



**NAVAL
POSTGRADUATE
SCHOOL**

MONTEREY, CALIFORNIA

DISSERTATION

**TERAHERTZ QUANTUM CASCADE STRUCTURES
USING STEP WELLS AND LONGITUDINAL
OPTICAL-PHONON SCATTERING**

by

Will Freeman

June 2009

Dissertation Supervisor:

Gamani Karunasiri

Approved for public release; distribution is unlimited

THIS PAGE INTENTIONALLY LEFT BLANK

REPORT DOCUMENTATION PAGE			<i>Form Approved OMB No. 0704-0188</i>
Public reporting burden for this collection of information is estimated to average 1 hour per response, including the time for reviewing instruction, searching existing data sources, gathering and maintaining the data needed, and completing and reviewing the collection of information. Send comments regarding this burden estimate or any other aspect of this collection of information, including suggestions for reducing this burden, to Washington headquarters Services, Directorate for Information Operations and Reports, 1215 Jefferson Davis Highway, Suite 1204, Arlington, VA 22202-4302, and to the Office of Management and Budget, Paperwork Reduction Project (0704-0188) Washington DC 20503.			
1. AGENCY USE ONLY (Leave blank)	2. REPORT DATE June 2009	3. REPORT TYPE AND DATES COVERED Dissertation	
4. TITLE AND SUBTITLE: Terahertz Quantum Cascade Structures Using Step Wells And Longitudinal Optical-Phonon Scattering		5. FUNDING NUMBERS	
6. AUTHOR: Will Freeman			
7. PERFORMING ORGANIZATION NAME(S) AND ADDRESS(ES) Naval Postgraduate School Monterey, CA 93943-5000		8. PERFORMING ORGANIZATION REPORT NUMBER	
9. SPONSORING /MONITORING AGENCY NAME(S) AND ADDRESS(ES)		10. SPONSORING/MONITORING AGENCY REPORT NUMBER	
11. SUPPLEMENTARY NOTES The views expressed in this thesis are those of the author and do not reflect the official policy or position of the Department of Defense or the U.S. Government.			
12a. DISTRIBUTION / AVAILABILITY STATEMENT Approved for public release; distribution is unlimited.		12b. DISTRIBUTION CODE	
13. ABSTRACT (maximum 200 words) Electron transport properties of terahertz (THz) longitudinal optical (LO)-phonon quantum cascade (QC) structures were modeled, in order to investigate high gain quantum cascade laser (QCL) structures. A new structure, a step well QC structure, was proposed. Under such an arrangement, there are three main energy levels within the step well, where the transition from the upper state to the middle state is at the THz radiative spacing and the transition from the middle state to the lower state is at or near the LO-phonon energy (~ 36 meV in GaAs). Because of the inherent difficulties in using rate equations for this type of transport analysis, a Monte Carlo simulation was developed. Step well injectors were modeled and shown to be capable of high injection efficiencies (~ 90%), higher than previously obtained. Comparisons to conventional square well LO-phonon structures are made, including a Monte Carlo analysis of a high power THz QCL. Interface roughness scattering was shown to be significant only for roughness greater than approximately one monolayer. It was found that step well structures are capable of high gains and injection efficiencies, with comparable characteristics to other square well designs, but do have increased scattering from the upper state to the lower states.			
14. SUBJECT TERMS Terahertz, THz, Quantum cascade structure, QC structure, Quantum cascade laser, QCL, Step well, Longitudinal optical-phonon, LO-phonon, Electron-phonon scattering, Electron-electron scattering, Impurity scattering, Interface roughness scattering, Optical transition, Electron transport, Monte Carlo method, Metal-metal waveguide, Surface plasmon waveguide			15. NUMBER OF PAGES 129
			16. PRICE CODE
17. SECURITY CLASSIFICATION OF REPORT Unclassified	18. SECURITY CLASSIFICATION OF THIS PAGE Unclassified	19. SECURITY CLASSIFICATION OF ABSTRACT Unclassified	20. LIMITATION OF ABSTRACT UU

THIS PAGE INTENTIONALLY LEFT BLANK

Approved for public release; distribution is unlimited

**TERAHERTZ QUANTUM CASCADE STRUCTURES USING STEP WELLS
AND LONGITUDINAL OPTICAL-PHONON SCATTERING**

Will Freeman

Civilian, Naval Air Warfare Center, China Lake, California

B.S., California State University, Northridge, 1996

M.S., Naval Postgraduate School, 2004

Submitted in partial fulfillment of the
requirements for the degree of

DOCTOR OF PHILOSOPHY IN PHYSICS

from the

NAVAL POSTGRADUATE SCHOOL

JUNE 2009

Author:

Will Freeman

Approved by:

Gamani Karunasiri
Professor of Physics
Dissertation Supervisor

Nancy M. Haegel
Professor of Physics

James Luscombe
Chair, Department of Physics

Donald L. Walters
Professor of Physics

Todd Weatherford
Associate Professor of Electrical
and Computer Engineering

Approved by:

James Luscombe, Chair, Department of Physics

Approved by:

Douglas Moses, Associate Provost for Academic Affairs

THIS PAGE INTENTIONALLY LEFT BLANK

ABSTRACT

Electron transport properties of terahertz (THz) longitudinal optical (LO)-phonon quantum cascade (QC) structures were modeled, in order to investigate high gain quantum cascade laser (QCL) structures. A new structure, a step well QC structure, was proposed. Under such an arrangement, there are three main energy levels within the step well, where the transition from the upper state to the middle state is at the THz radiative spacing and the transition from the middle state to the lower state is at or near the LO-phonon energy (~ 36 meV in GaAs). Because of the inherent difficulties in using rate equations for this type of transport analysis, a Monte Carlo simulation was developed. Step well injectors were modeled and shown to be capable of high injection efficiencies ($\sim 90\%$), higher than previously obtained. Comparisons to conventional square well LO-phonon structures are made, including a Monte Carlo analysis of a high power THz QCL. Interface roughness scattering was shown to be significant only for roughness greater than approximately one monolayer. It was found that step well structures are capable of high gains and injection efficiencies, with comparable characteristics to other square well designs, but do have increased scattering from the upper state to the lower states.

THIS PAGE INTENTIONALLY LEFT BLANK

TABLE OF CONTENTS

I.	INTRODUCTION.....	1
A.	PREVIOUS THz QC STRUCTURES	2
B.	STEP WELL QC STRUCTURES.....	4
C.	OVERVIEW	5
II.	QUANTUM WELLS	7
A.	TRANSFER MATRIX METHOD	7
1.	Self Consistent Solution of Schrödinger's and Poisson's Equations	9
B.	STEP QUANTUM WELLS	11
III.	SCATTERING AND OPTICAL TRANSITION	15
A.	ELECTRON-PHONON SCATTERING.....	15
1.	LO-Phonon Emission.....	24
2.	LO-Phonon Absorption	32
3.	Mean Scattering Rate	37
B.	ELECTRON-ELECTRON SCATTERING.....	38
1.	Antiparallel Spins	41
2.	Screening.....	47
3.	Mean Scattering Rate	49
4.	Antiparallel and Parallel Spins.....	50
C.	IMPURITY SCATTERING AND INTERFACE ROUGHNESS SCATTERING	51
1.	Mean Scattering Rate	54
D.	RADIATIVE TRANSITION	54
1.	Emission Rate	56
2.	Gain	58
3.	Rate Equations	59
IV.	MONTE CARLO SIMULATION.....	63
A.	ELECTRON TRANSPORT IN QC STRUCTURES	63
B.	MONTE CARLO METHOD.....	64
1.	Flight Times	64
2.	Selection Process	67
C.	IMPLEMENTATION	69
V.	WAVEGUIDE AND RESONATOR.....	73
A.	QCL RESONATORS	73
B.	SURFACE PLASMON AND METAL-METAL WAVEGUIDES.....	74
VI.	THz LO-PHONON QC STRUCTURES	77

A.	STEP WELL QC STRUCTURES.....	77
1.	Structure D619F10D.....	84
a.	MBE Growth and Fabrication.....	88
b.	Monte Carlo Simulation.....	90
2.	Structure D619F10E.....	91
B.	SQUARE WELL LO-PHONON QC STRUCTURE.....	95
1.	4.4 THz Structure.....	95
VII.	CONCLUSIONS AND DISCUSSION.....	99
	LIST OF REFERENCES.....	103
	INITIAL DISTRIBUTION LIST.....	109

LIST OF FIGURES AND TABLES

Figure I.A.1.	Conduction band diagrams illustrating the two main broadly categorized QC structure architectures, with one section outlined, (a) miniband structure (showing a bound to continuum structure), and (b) LO-phonon structure (showing a three well structure)	3
Figure II.A.1.	Illustration representing the conduction band as a number of constant steps, showing the coefficients for use in the transfer matrix method	8
Figure II.A.2.	Infinite plane surface of thickness Δx_3 and charge density $n_{3D}(x)$, showing the electric field	10
Figure II.B.1.	Conduction band profiles of step quantum wells. (a) Conduction band profile of a step quantum well comprised of $\text{Al}_x\text{Ga}_{1-x}\text{As}$ layers with compositions of 0.143/0.035/0/0.143 and well thicknesses in nm of 29.9/12.3, with $E_{21} = 13.7$ meV (3.3 THz) and $E_{10} = 37.9$ meV. (b) Conduction band profile of a step quantum well comprised of $\text{Al}_x\text{Ga}_{1-x}\text{As}$ layers with compositions of 0.143/0.035/0/0.143 and well thicknesses in nm of 20.9/13.5, with $E_{21} = 17.9$ meV (4.3 THz) and $E_{10} = 36.5$ meV. For both (a) and (b), the 1 to 0 transitions are near the LO-phonon energy and the applied bias is 10.1 kV/cm.....	12
Figure III.A.1.	Linear chain of diatomic atoms of masses m_1 and m_2	16
Figure III.A.2.	Phonon dispersion graph, showing the acoustic and optical branches	17
Figure III.A.3.	Feynman diagram for electron-phonon scattering	24
Figure III.A.4.	Contour illustrated for closing around the lower pole, for evaluating the contour integral in equation (III.A.49)	26
Figure III.A.5.	LO-phonon emission case 1a, $E_n - E_{n'} < \hbar\omega_{LO}$ and the electron does not have sufficient in-plane kinetic energy, forbidden transition	29
Figure III.A.6.	LO-phonon emission case 1b, $E_n - E_{n'} < \hbar\omega_{LO}$ and the electron has sufficient in-plane kinetic energy, allowed transition	30
Figure III.A.7.	LO-phonon emission case 2, $E_n - E_{n'} > \hbar\omega_{LO}$, “sideways” transition always allowed.....	31
Figure III.A.8.	LO-phonon emission case 2, \mathbf{q}_{\parallel} and \mathbf{k}_{\parallel} vectors when $\theta = 0$	32
Figure III.A.9.	LO-phonon absorption case 1a, $E_{n'} - E_n > \hbar\omega_{LO}$ and the electron does not have sufficient in-plane kinetic energy, forbidden transition	34
Figure III.A.10.	LO-phonon absorption case 1b, $E_{n'} - E_n > \hbar\omega_{LO}$ and the electron has sufficient in-plane kinetic energy, allowed transition	35
Figure III.A.11.	LO-phonon absorption case 2, $E_{n'} - E_n < \hbar\omega_{LO}$, “sideways” transition always allowed.....	36

Figure III.A.12.	LO-phonon absorption case 3, “upwards” transition always allowed.....	37
Figure III.B.1.	Feynman diagram for electron-electron scattering	38
Figure III.B.2.	Momentum vectors used in the calculation of the electron-electron scattering rate	46
Figure III.B.3.	Electron-electron scattering rate as a function of total energy at $T = 300$ K, with and without including screening, for subband populations of (a) 1×10^{10} and (b) $1 \times 10^{12} \text{ cm}^{-2}$	49
Figure III.B.4.	Momentum vectors used in the calculation of the electron-electron scattering rate, for the case when state blocking is included.....	50
Figure IV.B.1.	Graphical illustration for finding Γ_o , for the Monte Carlo method.....	67
Figure IV.B.2.	Graphical illustration of the Monte Carlo selection process.....	68
Figure IV.C.1.	A flow chart for the Monte Carlo simulation of QC structures	70
Figure IV.C.2.	Monte Carlo simulation of structure D619F10E at a bias of 51.9 mV/section, with all electrons initially distributed in state 2. Inset: Two sections of the structure are shown, with one section outlined	71
Figure V.B.1.	QCL waveguides, the (a) surface plasmon, (b) metal-metal, and (c) metal-patterned substrate waveguides.....	74
Figure VI.A.1.	Mean LO-phonon scattering rates for the 4.3 THz step quantum well (shown inset) as a function of initial state populations for $T_{lattice} = 25$ K and $T_{electron} = 100$ K (solid lines). For the 2 to 1 transition the maximum scattering rate (which is not an averaged rate) is also shown (dashed line). The lifetimes are listed (reciprocals of the essentially constant scattering rates)	79
Figure VI.A.2.	Mean electron-electron scattering rates for the 4.3 THz step quantum well as a function of initial state populations for $T_{electron} = 100$ K. The various scattering processes for the 2 to 1 and the 1 to 0 transitions for the simplified rate equation analysis are shown	80
Figure VI.A.3.	Scattering rates for the 4.3 THz step quantum well for $T_{electron} = 100$ K. (a) The total electron-electron scattering rates for the 2 to 1 and the 1 to 0 transitions, based on the processes for the simplified rate equation analysis, as a function of initial state populations. (b) The mean electron-electron scattering rates as a function of initial state populations for $T_{electron} = 100$ K, for some additional scattering processes for the 2 to 1 transition that are not within the framework of the simplified rate equation analysis.....	81
Figure VI.A.4.	Conduction band profile of a proposed step well QC structure found using a self consistent solution to Schrödinger’s and Poisson’s equations. The step well and resonant tunneling double barriers of one section are outlined. Beginning with the	

	left injector, the $\text{Al}_x\text{Ga}_{1-x}\text{As}$ layers compositions are 0.143/0.035/0/0.143/0/0.143/0 and thicknesses in nm are 4.3/20.9/13.5/1.7/9.6/2.5/7.6, with $E_{43} = 16.6$ meV (4 THz) and $E_{31} = 36.6$ meV. The applied field is 9.5 kV/cm. The 9.6 nm well is doped $2.9 \times 10^{16} \text{ cm}^{-3}$, which corresponds to a sheet density of $2.8 \times 10^{10} \text{ cm}^{-2}$	82
Figure VI.A.5.	Some of the step well QC structures considered, (a) one step, one well injector, (b) two step, one well injector, and (c) one step, two well injector.....	83
Figure VI.A.6.	Conduction band profile of structure D619F10D found using a self consistent solution to Schrödinger's and Poisson's equations. The step well and resonant tunneling well of one section are outlined. Beginning with the left injector, the $\text{Al}_x\text{Ga}_{1-x}\text{As}$ layers compositions are 0.16/0.05/0/0.05/0/0.16/0 and thicknesses in nm are 4.8/27.9/1.8/2/6.3/4.1/6.8, with $E_{32} = 15.1$ meV (3.6 THz) and $E_{21} = 37.2$ meV. The applied field is 10.5 kV/cm. The center 2 nm of the 6.8 nm well is doped to a sheet density of $3.4 \times 10^{10} \text{ cm}^{-2}$	85
Figure VI.A.7.	Threshold gain for a 200 μm ridge, 10 μm thick surface plasmon waveguide, as a function of lower plasma layer thickness for different doping concentrations (cm^{-3}) and mirror losses (cm^{-1}).....	86
Figure VI.A.8.	200 μm ridge, 10 μm thick surface plasmon waveguide with $t_{\text{plasma}} = 500$ nm doped at $3 \times 10^{18} \text{ cm}^{-3}$, (a) cross-section 2D mode intensity, (b) 1D profile mode intensity.....	87
Figure VI.A.9.	200 μm ridge, 10 μm thick metal-metal waveguide, cross-section 2D mode intensity.....	88
Figure VI.A.10.	Sample D619F10D. (a) Top view of the metal-metal waveguides, showing bond wires to the 100 and 200 μm wide by 1 mm long waveguides. (b) Cross-section of one of the 100 μm wide waveguides.....	89
Figure VI.A.11.	The measured I-V curve of sample D619F10D, for a 200 μm wide by 1 mm long metal-metal waveguide device.....	90
Figure VI.A.12.	Results of the Monte Carlo simulation of structure D619F10D, with and without including interface roughness scattering. (a) Current density as a function of applied electric field bias. (b) Gain as a function of bias.....	91
Figure VI.A.13.	Conduction band profile of structure D619F10E found using a self consistent solution to Schrödinger's and Poisson's equations, shown at an applied electric field of 10.4 kV/cm (56.3 mV/section). The step well and resonant tunneling well of one section are outlined. Beginning with the left injector, the $\text{Al}_x\text{Ga}_{1-x}\text{As}$ layers compositions are 0.16/0.05/0/0.05/0/0.16/0 and thicknesses in nm are 4.6/27.9/1.8/2/6.3/4.7/6.8, with $E_{32} =$	

	15.2 meV (~ 3.7 THz) and $E_{21} = 37.9$ meV. The center 2 nm of the 6.8 nm well is doped to a sheet density of $3.4 \times 10^{10} \text{ cm}^{-2}$92
Table VI.A.I.	Populations of the subbands (E_n) and electron temperatures found from the Monte Carlo simulation of structure D619F10E, at an applied electric field of 51.9 mV/section, with $T_{lattice} = 25$ K93
Figure VI.A.14.	Results of the Monte Carlo simulation of structure D619F10E, with and without including interface roughness scattering. (a) Current density as a function of applied electric field bias. (b) Gain as a function of bias. (c) The population densities and (d) electron temperatures for the upper (E_3) and middle (E_2) subbands as a function of bias94
Figure VI.B.1.	Conduction band profile of the 4.4 THz structure, shown at an applied electric field of 11.5 kV/cm (62.4 mV/section), with one section outlined. Beginning with the left injector, the $\text{Al}_x\text{Ga}_{1-x}\text{As}$ layers compositions are 0.15/0/0.15/0/0.15/0/0.15/0 and thicknesses in nm are 4.8/8.2/1.7/6.8/4.0/16.4/3.4/9.0. The 16.4 nm well is doped to a sheet density of $3.1 \times 10^{10} \text{ cm}^{-2}$96
Figure VI.B.2.	Results of the Monte Carlo simulation of the 4.4 THz structure, with and without including interface roughness scattering. (a) Current density as a function of applied electric field bias. (b) Gain as a function of bias.....97

LIST OF SYMBOLS

A = area
 a = lattice parameter
 $c = 2.997\,924\,58 \times 10^{10}$ cm sec⁻¹
 $e = 1.602\,176\,53(14) \times 10^{-19}$ Coul
 E = energy
 $E_{LO} = \omega_{LO} = \hbar\omega_{LO} \approx 36$ meV in GaAs, LO-phonon energy
 $|\mathbf{E}|$ = electric field magnitude
 $FWHM$ = full width half maximum
 H = Hamiltonian
 $\hbar = 6.582\,119\,15(56) \times 10^{-22}$ MeV sec
 j = probability density flux
 $k_B = 8.617\,343(15) \times 10^{-5}$ eV K⁻¹
 k and q = momentum vector magnitudes
 L = length
 $m \approx 0.067 \times 0.510\,998\,918(44)$ MeV in GaAs, electron effective mass (times c^2)
 n = subband population (cm⁻² or cm⁻³)
 R and r = intensity and electric field reflectivities respectively
 T = temperature
 V = interaction potential
 V = volume
 v = velocity magnitude (speed of light in medium)
 W = scattering rate
 $a_{\mathbf{q}}^\dagger$ = creation operator
 $a_{\mathbf{q}}$ = annihilation operator
 $\alpha = e^2/4\pi = e^2/4\pi\hbar c \approx 1/137$, fine-structure constant
 β = complex propagation constant
 Γ = confinement factor
 λ = wavelength
 ξ = “bed spring” spinor
 τ = lifetime
 ψ = “pitch fork” envelope wavefunction
 ω = angular frequency

Constants taken from the Particle Physics Booklet, PDG (July 2004).

THIS PAGE INTENTIONALLY LEFT BLANK

EXECUTIVE SUMMARY

Electron transport properties of terahertz (THz) longitudinal optical (LO)-phonon quantum cascade (QC) structures were modeled, in order to investigate and better understand the underlying physics of high gain quantum cascade laser (QCL) structures. A new structure, a step well QC structure, was proposed after rate equation analysis showed favorable scattering rate lifetimes for maintaining a population inversion. Under such an arrangement, there are three main energy levels within the step well, where the transition from the upper state to the middle state is at the THz radiative spacing and the transition from the middle state to the lower state is at or near the LO-phonon energy (~ 36 meV in GaAs) for fast depopulation. The middle state (upper phonon or lower lasing state) is a single energy state, contrasting to previous LO-phonon based QCL designs that have doublet states. For long wavelength lasers, this may be important because it eliminates the possibility for unwanted THz absorption that could otherwise occur between those doublet states. Since the radiative and LO-phonon transitions are intrawell in nature, high oscillator strengths and sub-picosecond middle state lifetimes are possible, which can lead to increased gain in the active region provided the upper state lifetime and injection efficiency are maintained. Because of the inherent difficulties in using rate equations for this type of transport analysis, a Monte Carlo simulation was developed. Step well injectors were modeled and shown to be capable of high injection efficiencies ($\sim 90\%$), which is higher than previously obtained in other LO-phonon structures with similar wavelengths of operation and oscillator strengths. It is likely that step injectors could be useful in approaches that do not arrange all three energy levels within the same well. Comparisons to conventional square well LO-phonon structures are made, including a Monte Carlo analysis of a high power THz QCL. Interface roughness scattering was shown to be significant only for roughness greater than approximately one monolayer. It was found that step well structures are capable of high gains and oscillator strengths, high injection efficiencies, with comparable characteristics to other square well designs, but do have increased scattering from the upper state to the lower states.

Throughout the course of this research, scientific results and findings were presented and published. This research was profiled in an article appearing in the Winter 2005/2006 issue of STARLINK. The author presented portions of this work in 2007 at The Ninth International Conference on Intersubband Transitions in Quantum Wells, and at the 2009 SPIE Defense, Security, and Sensing Conference. Scientific papers were published in the proceedings of these symposia (Proc. Ninth Int. Conf. on Intersubband Transitions in Quantum Wells, and Proc. SPIE 7311), as well as in a 2008 Naval Air Warfare Center report, NAWCWD TM 8577. This research also led to the filing of a U.S. patent in 2008.

ACKNOWLEDGMENTS

I would like to thank Gamani Karunasiri for the opportunity to be a part of his semiconductor group at NPS, for being an outstanding advisor and teacher, and for the many fun and interesting times I had working with him. Though there were numerous long hour days, those were overshadowed by the excitement of the research. I look forward to our continuing working relationship. Additional thanks are extended to the following:

To the NPS professors, Robert Armstead, Scott Davis, Nancy Haegel, Andres Larraza, Jim Luscombe, and Kai Woehler, I thank for their commitment to teaching and for giving me the necessary skills for investigating physical phenomena. I would also like to thank all of the professors on my committee, for their time.

To fellow students Kevin Buchanan for collaboration in the laboratory, and Kevin Lantz for earlier work on quantum wells that provided a starting point for this effort.

To H.C. Liu and his semiconductor group at NRC, for processing our QC samples.

This work was supported by China Lake's Fellowship Program, NAVAIR's ILIR Program sponsored by ONR, AFOSR, and NAVSEA. I would like to thank Pam Overfelt, Denton Marrs, and Robin Nissan, at NAWC, China Lake, CA, for their support.

THIS PAGE INTENTIONALLY LEFT BLANK

I. INTRODUCTION

Terahertz (THz) sources capable of operating in roughly the 1 to 5 THz region (300 to 60 μm) or far-infrared region are of considerable interest and are currently an active field of study. The THz frequency range has remained one of the least developed spectral regions, in part due to the lack of compact coherent sources. Though, in the last seven years or so, there has been a significant increase in efforts to produce compact THz sources. One approach to providing a compact source within the THz region, is to use a quantum cascade laser (QCL).¹ QCLs are solid state unipolar devices that differ from conventional semiconductor lasers in that transitions occur all within the conduction band, rather than between the bandgap of the conduction and valence bands. This class of semiconductor lasers allows for customization of the wavelength, by utilizing a multiple quantum well active region. A key feature of a QCL is that it consists of N repeated sections that form a cascade. Thus, one injected electron can emit many photons, which allows for differential quantum efficiencies greater than unity and hence higher power output.

QCLs have been successfully designed for operating in the infrared (IR) region (for wavelengths from ~ 3 to 24 μm , with room temperature operation, and CW operation of hundreds of mW of power).²⁻⁷ More recently, QCLs have been designed in the THz region (~ 0.84 to 5 THz, up to ~ 185 K, 250 mW pulsed, and 130 mW CW operation).⁸⁻¹² Though, for THz QCLs these figures are not from the same device. Temperature as a function of frequency for the best devices has approximately followed the trend $T \sim E_{\text{radiative}}/k_B = \hbar\omega/k_B$, and several of the low frequency designs operate with the assistance of a magnetic field.¹³ Alternative compact solid state sources, such as lead-salt semiconductor diode lasers, are limited by the bandgap to ~ 30 μm for the longest wavelengths.¹⁴ Other solid state devices such as transistors, Gunn oscillators, and Schottky diodes multipliers, have at best achieved low μW power levels in the THz region.¹⁵⁻¹⁸ Gas lasers generally have limited lasing frequencies and are usually fairly bulky. For these reasons, and because of the lack of intersubband materials, QCLs provide a good means for solid state THz sources.

Some applications for the terahertz spectrum include astrophysical science, medical science, THz spectroscopy, various security applications such as THz imaging systems, chemical gas sensing, and agent detection.^{15,19-31} Because THz radiation is nonionizing, it is attractive for security imaging applications. Many materials have absorption bands in the THz region of the electromagnetic spectrum, therefore this may be used for the characterization of explosive materials. Imaging in this region can allow for characterization of materials as they are brought through a security screen, as well as detect and identify materials. THz waves penetrate dielectrics, such as clothes and plastic, but are blocked by metallic objects, which affect their screening and detection capabilities.

A. PREVIOUS THz QC STRUCTURES

THz QCL designs have used two main quantum cascade (QC) structure architectures, broadly categorized as miniband^{1,32-36,8} and longitudinal optical (LO)-phonon,^{37-39,10,12} using coupled square quantum wells (square when unbiased). Although sometimes hybrid structures have been used with some overlap of these two approaches, usually designs can be classified as belonging to one of these two classes.

In miniband designs, very closely spaced energy levels are formed which create minibands. Radiative transitions take place between these minibands or between a relatively isolated state and a miniband. The first THz QCL which used a chirped superlattice,¹ is an example of a miniband structure. Other miniband designs have included a bound to continuum³³ (Figure I.A.1(a)) and a hybrid bound to continuum with optical-phonon scattering approaches.³⁵ Both featured minibands and somewhat isolated radiative states with more sideways radiative transitions.

In THz LO-phonon designs, the approach is similar to the first QCL developed² (which was a mid-IR laser) in that the lower lasing state is depopulated by electron-phonon scattering. Though, no terahertz LO-phonon QCL was fabricated that used all diagonal transitions like the first mid-IR QCL. Also, the use of digitally graded alloy injectors has been replaced with easier to grow so called funnel or resonant tunneling injectors.^{33,37} THz designs differ in that the radiative energy spacing is smaller than the

LO-phonon energy levels spacing. The first THz QCL that used the LO-phonon approach for depopulation, achieved the small radiative energy spacing by coupling the first two quantum wells with a thin barrier.³⁷ This design approach still principally used three quantum wells, but the third well differed in that it was used to resonantly tunnel the lower lasing state (or equivalently the upper phonon state) and also arrange a lower ground state spaced near the LO-phonon energy (a fourth well was also included at the injector). Although some variations to these structures have been made, all of the THz LO-phonon based structures have essentially been within the same framework and have included this type of three well arrangement, differing only in the design of the injector.

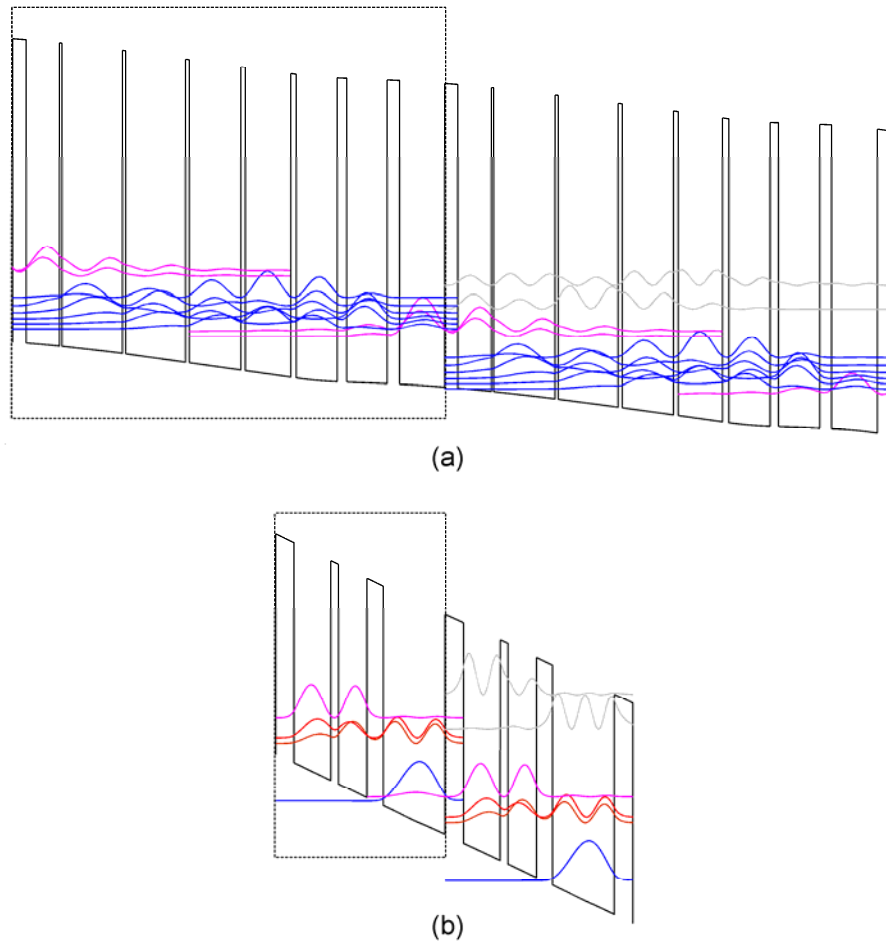


Figure I.A.1. Conduction band diagrams illustrating the two main broadly categorized QC structure architectures, with one section outlined, (a) miniband structure (showing a bound to continuum structure), and (b) LO-phonon structure (showing a three well structure).

This three well arrangement (Figure I.A.1(b)) is exemplified in the given reference.³⁹ Although at some THz frequencies, reported miniband designs have achieved the highest output power levels, this is attributable likely only to differences in the waveguide structure or the number of sections, and not the design approach of the active region. In fact, the highest output power QCL used a LO-phonon structure.¹⁰

LO-phonon based structures are of interest because of the large separation of the LO-phonon energy spacing, and also because the highest output power THz QCL used a LO-phonon approach. This approach seemingly is more likely tolerant to thermal backfilling, which could be important for increased operating temperatures. The LO-phonon structures typically have oscillator strengths (~ 0.5 to 0.96), while miniband structures such as the bound to continuum designs have higher listed oscillator strengths (~ 1.9). However, this may be somewhat offset since the LO-phonon sections are typically about half the length of their miniband counterparts, and thus typically have about twice the number of (LO-phonon based) sections within the same overall active region thickness. Our multiple section analysis of some miniband structures, has indicated lower oscillator strengths than reported. All of these miniband and LO-phonon designs have used square quantum wells that are symmetric when not under bias of an applied electric field. Next, a new theoretical approach that was investigated as part of this work, to the design of the active region for THz QCLs, will be discussed.

B. STEP WELL QC STRUCTURES

In addition to the use of miniband and square well LO-phonon approaches, the use of step well (asymmetric when unbiased) QC structures was first proposed by Freeman (author) and Karunasiri.⁴⁰ These types of structures can allow for the radiative and LO-phonon transitions to be placed within the same well. Since the bound state energy in high barrier square quantum wells increases $\sim n^2$ (with n being the quantum number of the state), it is not possible to have an upper radiative THz energy spacing and LO-phonon energy spacing (below) within a single square quantum well. Under a step well arrangement, there are three main energy levels, where the transition from the upper state to the middle state is at the THz radiative spacing and the transition from the middle

state to the lower state is at or near the LO-phonon energy (~ 36 meV in GaAs). The middle state (upper phonon or lower lasing state) is a single energy state, contrasting to previous LO-phonon based QCL designs that have doublet states. Allowing for a single middle energy state could be important for longer wavelength (lower THz frequency) devices to reduce unwanted absorption. By having vertical radiative and LO-phonon transitions within the same well, it is possible for these types of structures to yield high oscillator strengths, which can lead to increased gain in the active region provided the upper state lifetime and injection efficiency are maintained. The step in the well allows for high injection efficiency due to the spatial separation of the wavefunctions.

A step quantum well, in which at least two different conduction band heights within a well are used, allows for additional freedom and breaks the restriction single square wells have. Thus, a THz and LO-phonon energy spacing can be arranged within a single step quantum well. Others have analyzed step wells for proposed CO₂ pumped THz laser applications.⁴¹⁻⁴² Those step wells differ from the step wells considered in this research, where the radiative state is positioned above the LO-phonon transition states, and are intended for electrically pumped QCL structures. It was these unique characteristics of a step well, that prompted investigation of using a step well approach for a QC structure.

C. OVERVIEW

The ongoing imaging research using THz QCLs at NPS and by other groups, has shown there is a need for high power QCL sources.⁴³⁻⁵⁰ The research documented in this dissertation focused on investigating high gain THz QC structures of a particular type, LO-phonon QC structures. This was because our step well structures, which are LO-phonon designs, showed characteristics favorable for a high gain active region, and because the previously referenced highest power THz QCL was a LO-phonon design as well.

In the sections that follow, techniques developed for analyzing QC structures will be discussed. Methods for modeling quantum well structures, which are an absolute necessity for analyzing or designing QC band structures, will be covered. Various

scattering mechanisms and the calculation of pertinent scattering rates for determining state lifetimes, will then be discussed. Fundamental rate equations will be also reviewed along the way. As will be shown, the scattering rates of the electronic states are not constant, but are density and temperature dependent. Because of this, rate equations are not well suited for analyzing complete structures, as they would be nonlinear. One approach that is suitable for modeling entire structures is one based on Monte Carlo simulations. The Monte Carlo method that was developed for modeling the electron transport in QC structures is then discussed. The last sections cover the design and analysis of step well QC structures, and the first sample that was grown and processed. Comparisons are made to conventional square well LO-phonon designs. The final section will show our Monte Carlo analysis of a square well high power THz LO-phonon QC structure, including the effects of interface roughness scattering, and comparisons are made to experimental data.

The List of Symbols page shows some of the constants and notations used. Many of the derivations work in units with $\hbar = c = 1$. However, all sections dealing with equations of final computable values will have \hbar and c inserted back into the equations.

II. QUANTUM WELLS

The energy states in the active region of a QCL are formed by quantum wells in the conduction band. In the sections that follow, methods for calculating the electronic states in quantum well structures are discussed. The transfer matrix method is developed for solving the energy levels and wavefunctions in such structures, both for arbitrary shaped potentials and for a linearly changing potential. The former is useful for analyzing doped structures, where bending of the band structure occurs due to the separation of the charges from the host ions. This requires a self consistent solution to Schrödinger's and Poisson's equations. These techniques are used to solve step quantum well structures, to illustrate their potential use for THz QC structures.

A. TRANSFER MATRIX METHOD

There are a number of ways to solve Schrödinger's equation for bound states in quantum well structures. One commonly used approach, the transfer matrix method, can be used to solve arbitrary shaped conduction band potentials, which is useful when the self consistent solution is needed. Also to be discussed, is the case where the potential can be modeled as perfectly linear (classically a charge moving under constant acceleration).

The most general solution can be formulated by considering the solution for the case where the potential is regionally constant. With this approach, any linear or nonlinear potential can be modeled by a succession of small steps. The solution to the Schrödinger equation $H|\psi\rangle = E|\psi\rangle$ for a region with constant potential can be written as a sum of forward and reverse waves (Figure II.A.1).

$$\psi(x) = Ae^{ikx} + BAe^{-ikx} \quad (\text{II.A.1})$$

Since the wavefunction must be continuous, at an interface (x_n) the first boundary condition can be written as

$$\psi_n(x_n) = \psi_{n+1}(x_n) \quad (\text{II.A.2})$$

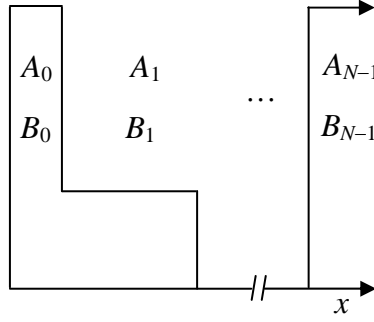


Figure II.A.1. Illustration representing the conduction band as a number of constant steps, showing the coefficients for use in the transfer matrix method.

A second boundary condition, is that the first derivative must be continuous. Choosing to take into account the change in effective masses across the boundaries, it is noted that the conserved probability density flux is $j = 1/m \text{Im}\{\psi^* \nabla \psi\}$. Setting $j_n = j_{n+1}$ the following is found

$$\frac{1}{m_n} \frac{d\psi_n(x_n)}{dx} = \frac{1}{m_{n+1}} \frac{d\psi_{n+1}(x_n)}{dx} \quad (\text{II.A.3})$$

The transfer matrix can be found from these boundary conditions by seeking relations for the coefficients A_n and B_n in terms of A_{n+1} and B_{n+1} . Substituting equation (II.A.1) into equations (II.A.2) and (II.A.3), the relationships for A_n and B_n can be found. The resulting equations can be cast into matrix form

$$\begin{bmatrix} A_n \\ B_n \end{bmatrix} = \begin{bmatrix} \frac{1}{2} \left(1 + \frac{k_{n+1} m_n}{k_n m_{n+1}} \right) e^{i(k_{n+1} - k_n)x_n} & \frac{1}{2} \left(1 - \frac{k_{n+1} m_n}{k_n m_{n+1}} \right) e^{-i(k_{n+1} + k_n)x_n} \\ \frac{1}{2} \left(1 - \frac{k_{n+1} m_n}{k_n m_{n+1}} \right) e^{i(k_{n+1} + k_n)x_n} & \frac{1}{2} \left(1 + \frac{k_{n+1} m_n}{k_n m_{n+1}} \right) e^{-i(k_{n+1} - k_n)x_n} \end{bmatrix} \begin{bmatrix} A_{n+1} \\ B_{n+1} \end{bmatrix} \quad (\text{II.A.4})$$

where inserting \hbar back into the equations $k_n = [2m_n(E - V_n)/\hbar^2]^{1/2}$. Because of the way the transfer matrix is developed, correct boundary conditions at the interfaces are always insured. In a structure with N regions, the matrix equation in terms of the first and last regions may be found as

$$\begin{bmatrix} A_0 \\ B_0 \end{bmatrix} = \mathbf{M}_0 \dots \mathbf{M}_{N-2} \begin{bmatrix} A_{N-1} \\ B_{N-1} \end{bmatrix} = \mathbf{M} \begin{bmatrix} A_{N-1} \\ B_{N-1} \end{bmatrix} = \begin{bmatrix} m_{00} & m_{01} \\ m_{10} & m_{11} \end{bmatrix} \begin{bmatrix} A_{N-1} \\ B_{N-1} \end{bmatrix} \quad (\text{II.A.5})$$

For bound state solutions, the wavefunctions must be square integrable and therefore vanish as $x \rightarrow \pm\infty$. From equation (II.A.5) we see the bound eigenstates can be found by

setting $m_{00}(E) = 0$. The transmission coefficient can also be found for the case where an electron is tunneling through one or more barriers. Assuming an electron incident from the left means that $B_{N-1} = 0$. The transmission coefficient is then found from $T(E) = j_{N-1}/j_0 = k_{N-1}m_0/(k_0m_{N-1})|1/m_{00}|^2$.

If the structure can be modeled as having a perfectly linear potential (as is the case for some QC structures where minimal bending of the band structure occurs from the doping), the transfer matrix can be formulated for the case of a linear potential. Writing the potential as $V(x) = V_n - e|\mathbf{E}|x$, Schrödinger's equation becomes Airy's equation

$$\frac{d^2\psi_n(x)}{d\rho_n(x)^2} = \rho_n(x)\psi_n(x) \quad (\text{II.A.6})$$

where $\rho_n(x) = (-|\mathbf{E}|x - \eta_n)/\beta$, $\eta_n = (E - V_n)/e$, $\beta = [\hbar^2|\mathbf{E}|^2/(2m_n e)]^{1/3}$, and the solutions are a linear combination of Airy functions.

$$\psi_n(x) = A_n Ai(\rho_n(x)) + B_n Bi(\rho_n(x)) \quad (\text{II.A.7})$$

The transfer matrix can be obtained in a similar manner as with the constant potential case, and can be simplified to^{51,52}

$$\begin{bmatrix} A_n \\ B_n \end{bmatrix} = \pi \begin{bmatrix} Ai(\alpha_{n+1})Bi'(\alpha_n) - \frac{m_n^{2/3}}{m_{n+1}^{2/3}} Ai'(\alpha_{n+1})Bi(\alpha_n) & Bi(\alpha_{n+1})Bi'(\alpha_n) - \frac{m_n^{2/3}}{m_{n+1}^{2/3}} Bi(\alpha_n)Bi'(\alpha_{n+1}) \\ \frac{m_n^{2/3}}{m_{n+1}^{2/3}} Ai(\alpha_n)Ai'(\alpha_{n+1}) - Ai'(\alpha_n)Ai(\alpha_{n+1}) & \frac{m_n^{2/3}}{m_{n+1}^{2/3}} Ai(\alpha_n)Bi'(\alpha_{n+1}) - Ai'(\alpha_n)Bi(\alpha_{n+1}) \end{bmatrix} \begin{bmatrix} A_{n+1} \\ B_{n+1} \end{bmatrix} \quad (\text{II.A.8})$$

where $\alpha_n = (2m_n e|\mathbf{E}|/\hbar^2)^{1/3}(-x_n - \eta_n/|\mathbf{E}|)$ and the prime denotes a derivative. In a structure with N regions, we can again write the matrix equation in terms of the first and last region the same as in equation (II.A.5). For bound state solutions, the wavefunctions must again vanish as $x \rightarrow \pm\infty$, or strictly speaking prior to the classical turning point as x tends toward ∞ . Since $Bi(\alpha_n) \rightarrow \infty$ as $x \rightarrow -\infty$, we set $B_0 = 0$, noting that $m_{10} \approx 0$ and $m_{10} \ll m_{11}$. The bound eigenstates are found by setting $m_{11}(E) = 0$.

1. Self Consistent Solution of Schrödinger's and Poisson's Equations

The self consistent solution of Schrödinger's and Poisson's equations is necessary to take into account doping in quantum well nanostructures. Formulating the transfer matrix method for a linear bias is computationally efficient, but is technically only valid

for undoped structures. In order to take into account bending of the band structure that occurs due to the separation of the dopant charges from the host ions, Schrödinger's equation is solved by approximating the conduction band as a number of small steps using the transfer matrix method. This approach allows for solution of any arbitrarily shaped potential. Another popular alternative technique used is the shooting method, which deals with the effective mass at intermediate points by taking the mean at the neighboring points.⁵³

The solution to Poisson's equation can be formulated for numerical computation as follows. Starting from Gauss's law $\nabla \cdot \mathbf{E} = \rho/\epsilon$ and the electrostatic form of Faraday's law $\nabla \times \mathbf{E} = 0$, noting that the curl of the gradient always vanishes, the electric field can be written in the usual way as $\mathbf{E} = -\nabla V_\sigma$. This leads to Poisson's equation $\nabla^2 V_\sigma = -\rho/\epsilon$. Now consider in general the following infinite sheet shown in Figure II.A.2, which is a plane surface of thickness Δx_3 with charge density $n_{3D}(x)$, illustrating the electric field.

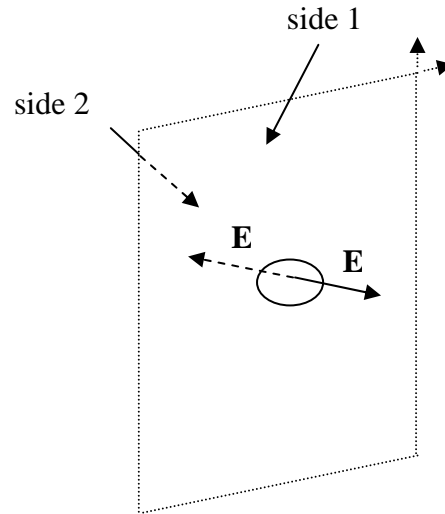


Figure II.A.2. Infinite plane surface of thickness Δx_3 and charge density $n_{3D}(x)$, showing the electric field.

Applying Gauss's law we find

$$\int d^2x \mathbf{E} \cdot \mathbf{n} = \frac{1}{\epsilon} \int d^3x \rho(x) = \frac{1}{\epsilon} \int d^2x \sigma(x) \quad (\text{II.A.9})$$

where σ is the 2D charge density. For this case, the electric field is then found from

$$2|\mathbf{E}| = \frac{\sigma}{\varepsilon} \quad (\text{II.A.10})$$

The charge density as a function of the growth direction may be written as

$$\sigma(x_3) = -e[n_{2D}\psi^*(x_3)\psi(x_3) - n_{3D}(x_3)]\Delta x_3 \quad (\text{II.A.11})$$

Using equations (II.A.10) and (II.A.11), the electric field is found, and the potential can then be determined by integration

$$V_\sigma = -\int dx \mathbf{E} \cdot \mathbf{n} \quad (\text{II.A.12})$$

If the dopants are concentrated in other states than just the ground state, the following modification is needed

$$\sigma(x_3) = -e \sum_{i=0}^{N-1} [n_{2D,i}\psi_i^*(x_3)\psi_i(x_3) - n_{3D,i}(x_3)]\Delta x_3 \quad (\text{II.A.13})$$

where the sum of all the sheet densities for all of the states equals the total sheet density. The self consistent solution iteratively computes the perturbing potential and adds it to the conduction band profile until after a given number of iterations, a self consistent solution is reached. Equation (II.A.13) assumes the charge distributions in the states are known. In practice, this is not known unless the electron transport of the full QC structure is analyzed and solved. One method for solving the state populations can be accomplished using Monte Carlo simulations, and this will be discussed later.

For QC structures, doping is needed to introduce charge carriers within the active region, and also to help reduce the possibility of the formation of high field domains.⁵⁴ A typical LO-phonon QC structure may have on the order of ~ 200 cascaded sections, and an undoped active region would essentially represent a large intrinsic region. Minimal doping levels can result in lower threshold currents, and moderate doping levels have been shown to result in the highest operating temperatures.^{55,56} In practice, only one well or a portion of a well or barrier is doped, in each section of the cascade.

B. STEP QUANTUM WELLS

As previously discussed, a step quantum well is not limited to have the bound state energy increase $\sim n^2$ as is the case for a conventional square quantum well. As such, the THz and LO-phonon energy spacing can be arranged within the same step well. This

approach is illustrated using the step quantum well structures shown in Figure II.B.1. These wells are comprised of $\text{Al}_x\text{Ga}_{1-x}\text{As}$ layers with compositions of 0.143/0.035/0/0.143. The step well thicknesses in nm are 29.9/12.3 for Figure II.B.1(a) and 20.9/13.5 for Figure II.B.1(b). The energy difference between states 2 and 1 for Figures II.B.1(a) and (b) are $E_{21} = 13.7$ meV (3.3 THz) and $E_{21} = 17.9$ meV (4.3 THz) respectively. Both step wells have E_{10} near the LO-phonon energy. The energy levels and wavefunctions were calculated assuming an applied field of 10.1 kV/cm (typical for LO-phonon QCLs) using the material parameters given in the references.⁵⁷⁻⁶⁵ This illustrates that it is possible to arrange different radiative transition energies and keep near resonant phonon transitions, within a single step well. This approach can be used to design radiative frequencies lower and higher than these as well.

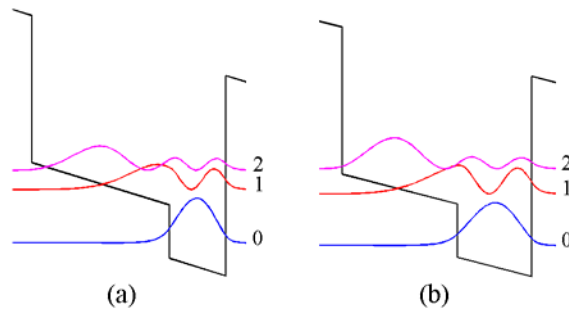


Figure II.B.1. Conduction band profiles of step quantum wells. (a) Conduction band profile of a step quantum well comprised of $\text{Al}_x\text{Ga}_{1-x}\text{As}$ layers with compositions of 0.143/0.035/0/0.143 and well thicknesses in nm of 29.9/12.3, with $E_{21} = 13.7$ meV (3.3 THz) and $E_{10} = 37.9$ meV. (b) Conduction band profile of a step quantum well comprised of $\text{Al}_x\text{Ga}_{1-x}\text{As}$ layers with compositions of 0.143/0.035/0/0.143 and well thicknesses in nm of 20.9/13.5, with $E_{21} = 17.9$ meV (4.3 THz) and $E_{10} = 36.5$ meV. For both (a) and (b), the 1 to 0 transitions are near the LO-phonon energy and the applied bias is 10.1 kV/cm.

This approach has a number of attractive features. Since the radiative and LO-phonon transitions are both vertical, this approach can yield large oscillator strengths and fast LO-phonon scattering rates for depopulation. Oscillator strengths for step well QC structures are typically around unity or greater. Conventional square well LO-phonon structures typically have oscillator strengths only about half of this and up to 0.96.³⁷ It is also noted that the step represents an additional barrier that can reduce parasitic injection

into the middle state. This could help the injection efficiency in QC structures, especially for longer wavelength devices where the radiative energy transition spacing is small. It is also seen that the middle state is a single state, contrasting to other conventional square well THz LO-phonon designs that always have doublet middle states. Having a single state could help reduce unwanted THz absorption, which could be important for longer wavelength devices. In the following sections, the calculation of various scattering rates of the electronic states in quantum well structures will be discussed.

THIS PAGE INTENTIONALLY LEFT BLANK

III. SCATTERING AND OPTICAL TRANSITION

In order to determine the state lifetimes within QC structures, various scattering rates of those states must be computed. In the sections that follow, the calculation of scattering rates for the pertinent scattering mechanisms will be covered. As will be shown, the scattering rates and hence the corresponding lifetimes of the electronic states are not constant, but rather are density and temperature dependent. We will also discuss the optical transition, and the important calculation of the gain. Some approximate rate equations will also be used to illustrate fundamental device parameters of interest.

A. ELECTRON-PHONON SCATTERING

Phonons are quantized vibrations within a lattice. Many electrical and thermal properties of materials are governed by phonon interactions. In semiconductor heterostructures, electron-phonon scattering can often be the dominant scattering mechanism. If the spacing between two states is at or near the resonant LO-phonon energy, the scattering rate to the lower state can be very fast. This is why resonant phonon scattering has been used in LO-phonon QCL devices as the primary mechanism for keeping a population inversion. Intraband LO-phonon scattering along with electron-electron scattering, are the mechanisms that cool the electron gas within subbands and thermally distribute the electrons into Fermi-Dirac distributions. Since our focus is on LO-phonon QC structures, this is the most important scattering mechanism, and it will be discussed first.

Beginning by considering a simple classical diatomic system, which is a good model for GaAs, the model consists of masses attached via springs in a chain (Figure III.A.1).⁶⁶ The Hamiltonian for the system is

$$\begin{aligned} H &= \sum KE + V \\ &= \sum_j \left[\frac{P_{x_j}^2}{2m_1} + \frac{P_{x'_j}^2}{2m_2} + \frac{1}{2}k(x'_j - x_j)^2 + \frac{1}{2}k(x_{j+1} - x'_j)^2 \right] \end{aligned} \quad (\text{III.A.1})$$

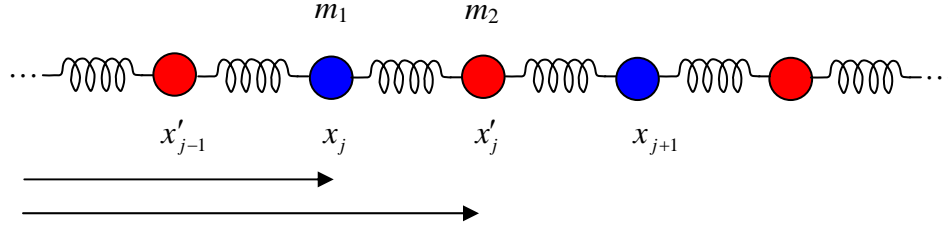


Figure III.A.1. Linear chain of diatomic atoms of masses m_1 and m_2 .

From Hamilton's equations we can write

$$\begin{aligned} \dot{P} &= -\frac{\partial H}{\partial x} \\ m_1 \ddot{x}_j &= -[k(x'_j - x_j) + k(x_j - x'_{j-1})] \\ m_2 \ddot{x}'_j &= -[k(x'_j - x_j) - k(x_{j+1} - x'_j)] \end{aligned} \quad (\text{III.A.2})$$

or

$$\begin{aligned} m_1 \ddot{x}_j &= k(x'_j + x'_{j-1} - 2x_j) \\ m_2 \ddot{x}'_j &= k(x_{j+1} + x_j - 2x'_j) \end{aligned} \quad (\text{III.A.3})$$

We seek solutions of the form

$$\begin{aligned} x_j &= \text{Re}\{X e^{i(q_j a - \omega t)}\} \\ x'_j &= \text{Re}\{X' e^{i(q_j a - \omega t)}\} \end{aligned} \quad (\text{III.A.4})$$

where a is the lattice spacing between like atoms. Using equations (III.A.4), equations (III.A.3) can be written in matrix notation after some manipulation as follows ($\text{Re}\{\}$ is assumed)

$$\begin{bmatrix} (\omega_{m_1}^2 - \omega^2) & -\frac{\omega_{m_1}^2}{2}(1 + e^{-iqa}) \\ -\frac{\omega_{m_2}^2}{2}(1 + e^{iqa}) & (\omega_{m_2}^2 - \omega^2) \end{bmatrix} \begin{bmatrix} X \\ X' \end{bmatrix} = 0 \quad (\text{III.A.5})$$

where

$$\begin{aligned} \omega_{m_1}^2 &= \frac{2k}{m_1} \\ \omega_{m_2}^2 &= \frac{2k}{m_2} \end{aligned} \quad (\text{III.A.6})$$

and $q = q_j - q_{j-1}$. The solution is found by setting the determinant to zero. Solving the quadratic in terms of ω^2 leads to the following.

$$\omega^2 = \frac{(\omega_{m_1}^2 + \omega_{m_2}^2)}{2} \pm \sqrt{\left(\frac{\omega_{m_1}^2 + \omega_{m_2}^2}{2}\right)^2 - \omega_{m_1}^2 \omega_{m_2}^2 \sin^2\left(\frac{qa}{2}\right)} \quad (\text{III.A.7})$$

Equation (III.A.7) can be used to graph the dispersion curve of ω versus q . Shown in Figure III.A.2 is the dispersion curve with $m_2 = 0.93 m_1$ ($m_{\text{Ga}} = 69.72 \text{ g/mol}$, $m_{\text{As}} = 74.92 \text{ g/mol}$). As can be seen, there are two main branches of phonons, known as acoustic and optical phonons (the notation $\omega \rightarrow \omega_{AC}$ for the acoustic branch and $\omega \rightarrow \omega_{OP}$ for the optical branch, will be used).

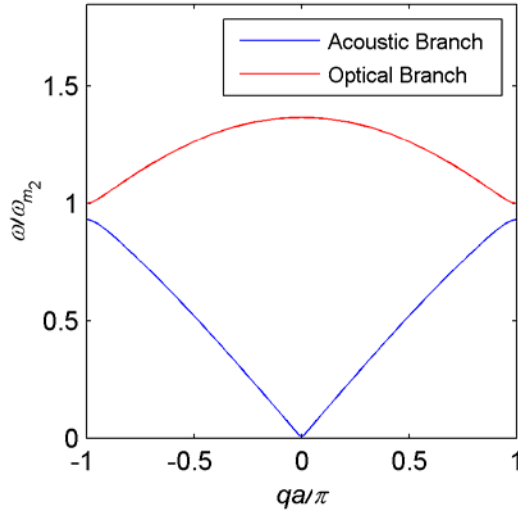


Figure III.A.2. Phonon dispersion graph, showing the acoustic and optical branches.

For the acoustic branch, which corresponds to the “negative sign” root in equation (III.A.7), as $q \rightarrow 0$, $\omega \rightarrow 0$ and we see using $\sin(qa/2) \sim qa/2$ and $(1 + stuff)^{1/2} \sim 1/2(stuff)$

$$\omega_{AC} = \frac{\omega_{m_1} \omega_{m_2}}{\sqrt{\omega_{m_1}^2 + \omega_{m_2}^2}} \frac{qa}{2} \quad (\text{III.A.8})$$

Substituting equation (III.A.8) into equation (III.A.5) gives the relative displacement between the two atoms.

$$\text{Re}\left\{\left(1 + \frac{iqa}{2}\right)X\right\} = X' \quad (\text{III.A.9})$$

For the optical branch, which corresponds to the “positive sign” root in equation (III.A.7), as $q \rightarrow 0$, $\omega \rightarrow \omega_{\max}$, and when $q = 0$ the following is found

$$\omega_{OP} = \sqrt{\omega_{m_1}^2 + \omega_{m_2}^2} = \sqrt{\frac{2k}{m_{reduced}}} \quad (III.A.10)$$

where $1/m_{reduced} = 1/m_1 + 1/m_2$. Substituting equation (III.A.10) into equation (III.A.5) gives the relative displacement between the two atoms.

$$\text{Re} \left\{ -\frac{m_1}{m_2} \left(1 + \frac{iqa}{2} \right) X \right\} = X' \quad (III.A.11)$$

As expected because of the high frequency nature at $q = 0$, the optical branch is characterized by opposing motion of the opposite atoms.

From equation (III.A.7) it is seen that there are a range of solutions specified by $q = \pm\pi/a$. For periodic boundary conditions ($x_{j+N} = x_j$ and $x'_{j+N} = x'_j$) of a finite chain of length $L = Na$, i.e., the ends of the chain are tied together in a ring, $qL = 2\pi n$, or $q_n = 2\pi n/L$. There are N number of m_1 atoms = N number of m_2 atoms = N number of two-body pairs or $2N$ number of atoms total (which is the number of degrees of freedom for the system). For the 3D case, in addition to longitudinal phonons, there can also be transverse phonons. In mixed composition crystals, the main branches can split into sub-branches. This has been experimentally measured and theoretically derived using the Lyddane-Sachs-Teller (LST) splitting.⁶⁷⁻⁶⁹

In polar semiconductors, the phonons create polarizations and thus electrostatic fields that follow the phonon. The interaction that describes this is referred to as the Fröhlich interaction.⁷⁰ An expression for this interaction can be found by first considering in general the dipole moment $\mathbf{p}_i = q_c \mathbf{x}$, where q_c is the charge and $|\mathbf{x}|$ is the displacement. The dipole moment per unit volume V , referred to as the electric polarization \mathbf{P} , is then written as

$$\mathbf{P} = \sum_i \frac{N_i}{V} \langle \mathbf{p}_i \rangle \quad (III.A.12)$$

The induced polarization due to the deformation by a phonon can be written as (noting e^* is the deformation charge, i.e., the charge that is transferred, not the electron charge)

$$\mathbf{P} = e^* (\mathbf{X} - \mathbf{X}') \frac{N}{V} \quad (\text{III.A.13})$$

The continuity equation $\partial_t J^\nu = 0$, where $J^\nu = (\rho, \mathbf{J})$, can be integrated with respect to time to give

$$\int dt \nabla \cdot \mathbf{J} = - \int dt \frac{\partial \rho}{\partial t} \quad (\text{III.A.14})$$

Since $\mathbf{P} = \int dt \mathbf{J}$, the charge density (charge per unit volume) is $\rho = -\nabla \cdot \mathbf{P}$. For an optical phonon with wavevector \mathbf{q} , this becomes

$$\rho(\mathbf{x}, t) = \text{Re} \left\{ -e^* \nabla \cdot (\mathbf{X} - \mathbf{X}') \frac{N}{V} e^{i\mathbf{q} \cdot \mathbf{x} - i\omega_q t} \right\} = \text{Re} \left\{ - \left(e^* i\mathbf{q} \cdot (\mathbf{X} - \mathbf{X}') \frac{N}{V} e^{i\mathbf{q} \cdot \mathbf{x} - i\omega_q t} \right) \right\} \quad (\text{III.A.15})$$

The dot product $\mathbf{q} \cdot (\mathbf{X} - \mathbf{X}')$ projects only in the longitudinal direction, i.e., the \mathbf{q} direction, thus only longitudinal optical (LO)-phonons can induce a charge. The induced electrostatic potential (Φ_q) can now be found from Poisson's equation $\nabla^2 \Phi_q = -\rho/\epsilon$, where $\epsilon = \epsilon_\infty$, and noting from the divergence theorem

$$\int d^2 x \nabla^2 \Phi_q = - \int d^2 x \frac{\rho}{\epsilon_\infty} \quad (\text{III.A.16})$$

thus

$$\Phi_q = \text{Re} \left\{ \frac{e^*}{\epsilon_\infty} (X - X') i q \frac{N}{V} \frac{1}{(iq)^2} \int e^u d^2 u \right\} = \text{Re} \left\{ \frac{e^*}{\epsilon_\infty} \frac{N}{V} (X - X') \frac{1}{iq} \int e^u d^2 u \right\} \quad (\text{III.A.17})$$

where $u = i\mathbf{q} \cdot \mathbf{x} - i\omega_q t$, $du = i\mathbf{q} \cdot d\mathbf{x}$, and $d^2 u = |\mathbf{q}|^2 d^2 x$. Performing the integral and taking the real part,⁷¹ the following is found

$$\Phi_q = - \frac{i e^*}{2 \epsilon_\infty} \frac{N}{V} \frac{1}{q} (X - X') (e^{iq \cdot x} - e^{-iq \cdot x}) = \frac{i e^*}{2 \epsilon_\infty} \frac{N}{V} \frac{1}{q} (X - X') (-e^{iq \cdot x} + e^{-iq \cdot x}) \quad (\text{III.A.18})$$

and the perturbing potential is now found from

$$\begin{aligned} V_{e^- \text{-phonon}} &= \sum_{\mathbf{q}} -e \Phi_q \\ &= \sum_{\mathbf{q}} -e \frac{i e^*}{2 \epsilon_\infty} \frac{N}{V} \frac{1}{q} (X - X') (-e^{iq \cdot x} + e^{-iq \cdot x}) \end{aligned} \quad (\text{III.A.19})$$

An expression for the deformation charge e^* due to a LO-phonon can be determined from classical arguments, and is found to be⁶⁶

$$e^* = \sqrt{\frac{mV\omega_{LO}^2 \epsilon_\infty^2}{N} \left(\frac{1}{\epsilon_\infty} - \frac{1}{\epsilon_{st}} \right)} \quad (\text{III.A.20})$$

To solve for the amplitude $X-X'$, the system must be quantized. Second quantization could be used to promote everything directly in our Hamiltonian to operators using the canonical commutation relations, but there is an easier way. This standard procedure is to write the Hamiltonian in terms of generalized coordinates.⁶⁶ Using canonical coordinates and momenta (Q'_i and P'_i), a set of normal coordinates (q_q) is found such that the potential is in diagonal form. The canonical commutation relations can then be used to quantize the system in a straight forward fashion. The Hamiltonian expressed in canonical coordinates is

$$H_{HO} = \sum_i \frac{P_i'^2}{2m_i} + \sum_{i,j} \frac{1}{2} A_{ij} Q'_i Q'_j \quad (\text{III.A.21})$$

where for the restricted harmonic oscillator case

$$A_{ij} = \frac{\partial^2 V}{\partial Q'_i \partial Q'_j} Q'_i Q'_j \quad (\text{III.A.22})$$

noting that A_{ij} is real and symmetric ($A_{ij} = A_{ji}$) and $[Q'_i, P'_j] = i\delta_{ij}$, $[Q'_i, Q'_j] = [P'_i, P'_j] = 0$. Following Feynman⁷² by scaling our canonical coordinates and momenta (to make the notation simpler), we look to find the normal coordinates. The scaling chosen is $Q_i = (m_i)^{1/2} Q'_i$, $P_i = P'_i / (m_i)^{1/2}$ and $U_{ij} = 2A_{ij} / (m_i m_j)^{1/2}$. The Hamiltonian then becomes

$$H_{HO} = \frac{1}{2} \sum_i P_i^2 + \frac{1}{2} \sum_{i,j} U_{ij} Q_i Q_j \quad (\text{III.A.23})$$

noting that U_{ij} is real and symmetric ($U_{ij} = U_{ji}$). A transform between the normal coordinates and the canonical coordinates can be written as

$$q_q = \sum_i C_{qi} Q_i \quad (\text{III.A.24})$$

where the transformation matrix C_{qi} is orthogonal, $\sum_i C_{qi} C_{\beta i} = \delta_{q\beta}$, $\sum_q C_{qi} C_{qj} = \delta_{ij}$, and the inverse transform is

$$Q_i = \sum_q C_{iq} q_q \quad (\text{III.A.25})$$

The canonical momenta is likewise written as (where $[q_q, p_\beta] = i\delta_{q\beta}$)

$$p_q = \sum_i C_{qi} P_i \quad (\text{III.A.26})$$

The eigenvalues ω_q^2 can now be found from

$$\sum_{i,j} C_{qi} C_{\beta j} U_{ij} = \omega_q^2 \delta_{q\beta} \quad (\text{III.A.27})$$

and thus

$$\sum_{i,j} U_{ij} Q_i Q_j = \sum_q \omega_q^2 q_q^2 \quad (\text{III.A.28})$$

Using equations (III.A.26) and (III.A.28), the Hamiltonian can now be written as a sum of independent harmonic oscillators.

$$\begin{aligned} H_{HO} &= \frac{1}{2} \sum_q p_q^2 + \frac{1}{2} \sum_q \omega_q^2 q_q^2 \\ &= \frac{1}{2} \sum_q (p_q^2 + \omega_q^2 q_q^2) \end{aligned} \quad (\text{III.A.29})$$

These decoupled oscillators represent noninteracting phonons. The solution is of course well known for the harmonic oscillator, and it is now straight forward to quantize. Treating each classical harmonic oscillator as a quantum harmonic oscillator, p_q and q_q are promoted to operators, and the canonical commutation relations are imposed.

$$\begin{aligned} [q_i, p_j] &= i \delta_{ij} \\ [q_i, q_j] &= [p_i, p_j] = 0 \end{aligned} \quad (\text{III.A.30})$$

The operators p and q can be written in terms of ladder operators, noting that the canonical commutation relation $[q_i, p_j] = i \delta_{ij}$ is the same as $[a_q, a_q^\dagger] = 1$.

$$\begin{aligned} q &= \frac{1}{\sqrt{2\omega_q}} (a_q + a_q^\dagger) \\ p &= -i \sqrt{\frac{\omega_q}{2}} (a_q - a_q^\dagger) \end{aligned} \quad (\text{III.A.31})$$

The Hamiltonian for the sum of the independent oscillators can now be written as

$$H_{HO} = \sum_q \omega_q \left(a_q^\dagger a_q + \frac{1}{2} \right) = \sum_q \omega_q \left(a_q a_q^\dagger - \frac{1}{2} \right) \quad (\text{III.A.32})$$

and the Hamiltonian can be explicitly written for the 3D case as follows, keeping in mind that for the 3D case both longitudinal and transverse modes can exist

$$H_{HO} = \sum_{\mathbf{q}} \sum_{s=1}^3 \omega_{\mathbf{q}} \left(a_{\mathbf{q},s}^\dagger a_{\mathbf{q},s} + \frac{1}{2} \right) \quad (\text{III.A.33})$$

where for each independent oscillator $|i = 0\rangle$ is an eigenstate of H_{HO} with a zero-point eigenvalue of $\frac{1}{2}\omega_{\mathbf{q}}$. When the zero-point energy is set to zero, $a_{\mathbf{q},s}|i = 0\rangle = 0$ and the vacuum state $|0\rangle$ has an energy eigenvalue of $E = 0$. Using the commutators below

$$[H_{HO}, a_{\mathbf{q},s}^\dagger] = \omega_{\mathbf{q}} a_{\mathbf{q},s}^\dagger, \quad [H_{HO}, a_{\mathbf{q},s}] = -\omega_{\mathbf{q}} a_{\mathbf{q},s} \quad (\text{III.A.34})$$

it is seen $|n\rangle = (a_{\mathbf{q},s}^\dagger)^n |0\rangle$ and the Hamiltonian for each oscillator is diagonalized, which has a complete set of eigenvalues of $(n+\frac{1}{2})\omega = (n+\frac{1}{2})E_{LO}$ (for $n = 0, 1, \dots$).

The background energy of the phonon modes is $\sum \frac{1}{2}\omega_{\mathbf{q}}$. For systems with many degrees of freedom, this c-number becomes large and infinite in extent for fields. Since only energy differences can physically be measured, this zero-point value is not important for our purposes here. However, it is noted though for fields that have infinite degrees of freedom, this shift in the zero-point could potentially be a problem.⁷³

The statistics of phonon particles can be determined by considering the following two particle state $a_{\mathbf{p}}^\dagger a_{\mathbf{q}}^\dagger |0\rangle$. Noting that $a_{\mathbf{p}}^\dagger$ and $a_{\mathbf{q}}^\dagger$ commute, the state is identical if the two particles are interchanged. Analogous to a classical oscillator that can be excited to an arbitrary number of high levels, mode \mathbf{q} can have an arbitrary number of particles. Thus, phonons are Bosons and the average number of phonons in a mode can be found from Bose-Einstein statistics $\langle N \rangle = 1/Z \text{Tr} N e^{-\beta H}$.

The mode displacement is now found by using the correspondence principle where the classical energy in the mode is the same as the quantum energy in the mode, which is $N_q E_{LO}$ (where N_q is the average number of phonons in the mode and E_{LO} is the quantized eigenstate energy).

$$\frac{1}{2} m \omega_{LO}^2 |X - X'|^2 N = N_q E_{LO} \quad (\text{III.A.35})$$

$$|X - X'| = \sqrt{\frac{2N_q E_{LO}}{Nm \omega_{LO}^2}} \quad (\text{III.A.36})$$

Substituting the expressions for e^* from equation (III.A.20) and the modal amplitude $X-X'$ from equation (III.A.36) into equation (III.A.19), the perturbing potential for the LO-phonon interaction can be written as

$$\begin{aligned}
V_{e^- - \text{phonon}} &= \sum_{\mathbf{q}} -e\Phi_{\mathbf{q}} = \sum_{\mathbf{q}} -e \frac{i}{2} \frac{1}{\epsilon_{\infty}} \frac{N}{V} \frac{1}{q} \sqrt{\frac{V}{N} m \omega_{LO}^2 \epsilon_{\infty}^2 \left(\frac{1}{\epsilon_{\infty}} - \frac{1}{\epsilon_{st}} \right) \frac{2N_{\mathbf{q}} E_{LO}}{Nm \omega_{LO}^2}} [-e^{i\mathbf{q}\cdot\mathbf{x}} + e^{-i\mathbf{q}\cdot\mathbf{x}}] \\
&= \sum_{\mathbf{q}} \frac{i}{q} \sqrt{\frac{1}{V} \frac{e^2}{2} E_{LO} \left(\frac{1}{\epsilon_{\infty}} - \frac{1}{\epsilon_{st}} \right)} \sqrt{N_{\mathbf{q}}} [e^{i\mathbf{q}\cdot\mathbf{x}} - e^{-i\mathbf{q}\cdot\mathbf{x}}]
\end{aligned} \tag{III.A.37}$$

where $q = |\mathbf{q}|$, which is the magnitude of the 3D momentum vector (includes the parallel in-plane and x_3 components). Separating this into emission and absorption terms, with $N_{\mathbf{q}} \rightarrow N_{\mathbf{q}}+1$ for the emission case, to include spontaneous and stimulated phonon emission

$$V_{e^- - \text{phonon}} = \begin{cases} \sum_{\mathbf{q}} \frac{i}{q} \sqrt{\frac{e^2 E_{LO}}{2V} \left(\frac{1}{\epsilon_{\infty}} - \frac{1}{\epsilon_{st}} \right)} \sqrt{N_{\mathbf{q}}} e^{i\mathbf{q}\cdot\mathbf{x}} & (\text{absorption}) \\ - \sum_{\mathbf{q}} \frac{i}{q} \sqrt{\frac{e^2 E_{LO}}{2V} \left(\frac{1}{\epsilon_{\infty}} - \frac{1}{\epsilon_{st}} \right)} \sqrt{N_{\mathbf{q}} + 1} e^{-i\mathbf{q}\cdot\mathbf{x}} & (\text{emission}) \end{cases} \tag{III.A.38}$$

This can also be written in terms of ladder operators ($\mathbf{a}_{\mathbf{q}}^{\dagger}|N_{\mathbf{q}}\rangle = (N_{\mathbf{q}}+1)^{1/2}|N_{\mathbf{q}}+1\rangle$, $\mathbf{a}_{\mathbf{q}}|N_{\mathbf{q}}\rangle = (N_{\mathbf{q}})^{1/2}|N_{\mathbf{q}}-1\rangle$)

$$\begin{aligned}
V_{e^- - \text{phonon}} &= \sum_{\mathbf{q}} \frac{i}{q} \sqrt{\frac{e^2 E_{LO}}{2V} \left(\frac{1}{\epsilon_{\infty}} - \frac{1}{\epsilon_{st}} \right)} (\mathbf{a}_{\mathbf{q}} e^{i\mathbf{q}\cdot\mathbf{x}} - \mathbf{a}_{\mathbf{q}}^{\dagger} e^{-i\mathbf{q}\cdot\mathbf{x}}) \\
&= \sum_{\mathbf{q}} \frac{i}{q} \sqrt{\frac{e^2 E_{LO}}{2V} \left(\frac{1}{\epsilon_{\infty}} - \frac{1}{\epsilon_{st}} \right)} (\mathbf{a}_{\mathbf{q}} - \mathbf{a}_{-\mathbf{q}}^{\dagger}) e^{i\mathbf{q}\cdot\mathbf{x}}
\end{aligned} \tag{III.A.39}$$

Sometimes this is expressed in terms of the nondimensional constant $\alpha_F = e^2/(8\pi\hbar\omega)(2m\omega/\hbar)^{1/2}(1/\epsilon_{\infty}+1/\epsilon_{st})$.

The following diagram (Figure III.A.3) shows the indexing and notation used for electron-phonon scattering, where i is the initial electron state, f is the final electron state, and n is the subband index.

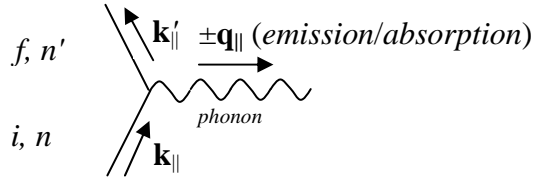


Figure III.A.3. Feynman diagram for electron-phonon scattering.

In this section some vectors have three components (\mathbf{q}) whereas others have two parallel in-plane components. Parallel subscripts will be used for parallel in-plane vectors (\mathbf{k}_{\parallel} and \mathbf{q}_{\parallel}) and the prime notation will indicate the final state. Now with the Fröhlich interaction potential, the scattering rate can be computed. The 2D wavefunctions are Bloch functions.

$$|i\rangle = |u_i \alpha_i\rangle \quad (\text{III.A.40})$$

Since the interest is in the matrix element for intersubband transitions, the following approximation can be used⁷⁴

$$\begin{aligned} \langle \psi_f | V | \psi_i \rangle &= \langle u_f \alpha_f | V | u_i \alpha_i \rangle \approx \langle u_f | V | u_i \rangle_{\text{cell}} \langle \alpha_f | \alpha_i \rangle + \langle u_f | u_i \rangle_{\text{cell}} \langle \alpha_f | V | \alpha_i \rangle \\ &\approx \langle \alpha_f | V | \alpha_i \rangle \end{aligned} \quad (\text{III.A.41})$$

where for intersubband transitions $\langle \alpha_f | \alpha_i \rangle = 0$ and $\langle u_f | u_i \rangle_{\text{cell}} = 1$. Working in the $\langle \mathbf{x} |$ representation, where $(x_1, x_2, x_3) = (x, y, z)$ with x_1, x_2 parallel to the growth direction x_3 , the wavefunctions can be written as

$$\langle \mathbf{x} | i \rangle = \frac{1}{\sqrt{A}} u_i e^{i\mathbf{k}_{\parallel} \cdot \mathbf{x}_{\parallel}} \psi_n(x_3) \approx \frac{1}{\sqrt{A}} e^{i\mathbf{k}_{\parallel} \cdot \mathbf{x}_{\parallel}} \psi_n(x_3) \quad (\text{III.A.42})$$

This will be used in subsequent sections and the periodic u_i part of the Bloch function will be dropped.

1. LO-Phonon Emission

Considering the emission case first, where $V = V_{e^- - \text{phonon}}$. The matrix element can be written as

$$\begin{aligned}
\langle f | V | i \rangle &= \langle f | - \sum_{\mathbf{q}} \frac{i}{q} \sqrt{\frac{e^2 E_{LO}}{2V} \left(\frac{1}{\epsilon_{\infty}} - \frac{1}{\epsilon_{st}} \right)} \sqrt{N_q + 1} e^{-i\mathbf{q} \cdot \mathbf{x}} | i \rangle \\
&= -\frac{i}{A} \sqrt{\frac{e^2 E_{LO}}{2V} \left(\frac{1}{\epsilon_{\infty}} - \frac{1}{\epsilon_{st}} \right)} \sqrt{N_q + 1} \int d^3 x \sum_{\mathbf{q}} \frac{1}{q} e^{-i\mathbf{k}'_{\parallel} \cdot \mathbf{x}_{\parallel}} e^{-i\mathbf{q} \cdot \mathbf{x}} e^{i\mathbf{k}_{\parallel} \cdot \mathbf{x}_{\parallel}} \psi_{n'}^*(x_3) \psi_n(x_3) \\
&= -\frac{i}{A} \sqrt{\frac{e^2 E_{LO}}{2V} \left(\frac{1}{\epsilon_{\infty}} - \frac{1}{\epsilon_{st}} \right)} \sqrt{N_q + 1} \int d^3 x \sum_{\mathbf{q}} \frac{1}{q} e^{-i\mathbf{k}'_{\parallel} \cdot \mathbf{x}_{\parallel}} e^{-i(\mathbf{q}_{\parallel} + \mathbf{q}_3) \cdot \mathbf{x}} e^{i\mathbf{k}_{\parallel} \cdot \mathbf{x}_{\parallel}} \psi_{n'}^*(x_3) \psi_n(x_3) \\
&= -\frac{i}{A} \sqrt{\frac{e^2 E_{LO}}{2V} \left(\frac{1}{\epsilon_{\infty}} - \frac{1}{\epsilon_{st}} \right)} \sqrt{N_q + 1} \int dx_3 \int d^2 x_{\parallel} \sum_{\mathbf{q}} \frac{1}{q} e^{i(\mathbf{k}_{\parallel} - \mathbf{k}'_{\parallel} - \mathbf{q}_{\parallel}) \cdot \mathbf{x}_{\parallel}} e^{-iq_3 x_3} \psi_{n'}^*(x_3) \psi_n(x_3)
\end{aligned} \tag{III.A.43}$$

For mode \mathbf{q} , there is only one value of \mathbf{q}_{\parallel} that makes the $d^2 x_{\parallel}$ integral nonvanishing, and is such when the exponent is zero (otherwise the other values lead to the addition of random phase terms which add to zero). This gives a Kronecker delta function, which is the conservation of momentum as expected for the emission case.

$$\begin{aligned}
\langle f | V | i \rangle &= -\frac{i}{A} \sqrt{\frac{e^2 E_{LO}}{2V} \left(\frac{1}{\epsilon_{\infty}} - \frac{1}{\epsilon_{st}} \right)} \sqrt{N_q + 1} \int dx_3 \frac{1}{q} e^{-iq_3 x_3} \psi_{n'}^*(x_3) \psi_n(x_3) A \delta(\mathbf{k}_{\parallel} - \mathbf{k}'_{\parallel} - \mathbf{q}_{\parallel}) \\
&= -i \sqrt{\frac{e^2 E_{LO}}{2V} \left(\frac{1}{\epsilon_{\infty}} - \frac{1}{\epsilon_{st}} \right)} \sqrt{N_q + 1} \frac{\int dx_3 e^{-iq_3 x_3} \psi_{n'}^*(x_3) \psi_n(x_3)}{q} \delta(\mathbf{k}_{\parallel} - \mathbf{k}'_{\parallel} - \mathbf{q}_{\parallel})
\end{aligned} \tag{III.A.44}$$

To find the electron-phonon scattering rate, the matrix element is substituted into Fermi's golden rule, summing over the final states.⁷⁵ Inserting \hbar and c back into the equations (noting $E_{LO} = \hbar \omega_{LO}$)

$$\begin{aligned}
W_{e^{-\text{phonon}}} &= \frac{2\pi}{\hbar} \sum_f |\langle f | V | i \rangle|^2 \delta \left[\left(E_{n'} + \frac{\hbar^2 k_{\parallel}^2}{2m} \right) + \hbar \omega_{LO} - \left(E_n + \frac{\hbar^2 k_{\parallel}^2}{2m} \right) \right] \\
&= \frac{2\pi}{\hbar} \frac{e^2 \hbar \omega_{LO}}{2V} \left(\frac{1}{\epsilon_{\infty}} - \frac{1}{\epsilon_{st}} \right) (N_q + 1) \sum_f \left| \frac{\int dx_3 e^{-iq_3 x_3} \psi_{n'}^*(x_3) \psi_n(x_3)}{q} \right|^2 \delta(\mathbf{k}_{\parallel} - \mathbf{k}'_{\parallel} - \mathbf{q}_{\parallel}) \\
&\times \delta(E_{n'} + E_{k'} + \hbar \omega_{LO} - E_n - E_k)
\end{aligned} \tag{III.A.45}$$

Converting the final states summation to an integral in k-space⁷⁵ and dropping the momentum delta function

$$\begin{aligned}
W_{e^- - \text{phonon}} &= \frac{\pi e^2 \omega_{LO}}{V} \left(\frac{1}{\epsilon_\infty} - \frac{1}{\epsilon_{st}} \right) (N_q + 1) \frac{V}{(2\pi)^3} \int d^3 q \frac{\left| \int dx_3 e^{-iq_3 x_3} \psi_{n'}^*(x_3) \psi_n(x_3) \right|^2}{q_\parallel^2 + q_3^2} \\
&\times \delta(E_{n'} + E_{k'} + \hbar \omega_{LO} - E_n - E_k) \\
&= \frac{e^2 \omega_{LO}}{8\pi^2} \left(\frac{1}{\epsilon_\infty} - \frac{1}{\epsilon_{st}} \right) (N_q + 1) \int d\theta dq_\parallel dq_3 \frac{\left| \int dx_3 e^{-iq_3 x_3} \psi_{n'}^*(x_3) \psi_n(x_3) \right|^2}{q_\parallel^2 + q_3^2} \\
&\times \delta(E_{n'} + E_{k'} + \hbar \omega_{LO} - E_n - E_k)
\end{aligned} \tag{III.A.46}$$

This can be rewritten as

$$W_{e^- - \text{phonon}} = \frac{e^2 \omega_{LO}}{8\pi^2} \left(\frac{1}{\epsilon_\infty} - \frac{1}{\epsilon_{st}} \right) (N_q + 1) \int d\theta dq_\parallel q_\parallel I_{2D}(\mathbf{q}_\parallel) \delta(E_{n'} + E_{k'} + \hbar \omega_{LO} - E_n - E_k) \tag{III.A.47}$$

where

$$I_{2D}(\mathbf{q}_\parallel) = \int_{-\infty}^{\infty} dq_3 \frac{\left| \int dx_3 e^{-iq_3 x_3} \psi_{n'}^*(x_3) \psi_n(x_3) \right|^2}{q_\parallel^2 + q_3^2} \tag{III.A.48}$$

The limits of integration for the q_3 integral are from $\pm\infty$, which is unfavorable for numerical computation. It can be written in an alternative form by pulling the q_3 integral inside and rewriting as

$$I_{2D}(\mathbf{q}_\parallel) = \int dx_3 dx'_3 \psi_{n'}^*(x_3) \psi_n(x_3) \psi_{n'}^*(x'_3) \psi_n(x'_3) \int_{-\infty}^{\infty} dq_3 \frac{e^{-iq_3(x_3-x'_3)}}{q_\parallel^2 + q_3^2} \tag{III.A.49}$$

The q_3 integral can now be evaluated by contour integration. For positive $x_3-x'_3$, the lower pole is pick up by closing the contour in the lower half plane (Figure III.A.4)

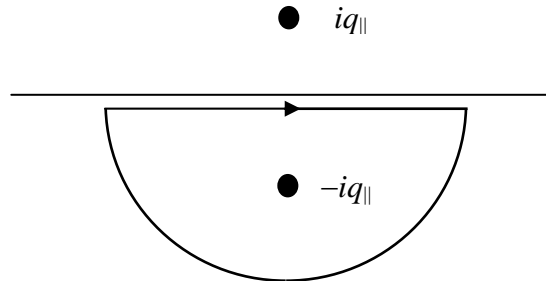


Figure III.A.4. Contour illustrated for closing around the lower pole, for evaluating the contour integral in equation (III.A.49).

$$\int_{-\infty}^{\infty} dq_3 \frac{e^{-iq_3(x_3-x'_3)}}{q_{\parallel}^2 + q_3^2} = 2\pi i \operatorname{res} = -2\pi i \frac{e^{-i(x_3-x'_3)(-iq_{\parallel})}}{-iq_{\parallel} + iq_{\parallel}} = \frac{\pi}{q_{\parallel}} e^{-q_{\parallel}(x_3-x'_3)} \text{ for } (x_3 - x'_3) \geq 0 \quad (\text{III.A.50})$$

and similarly for negative $x_3-x'_3$, the contour is closed in the upper half plane

$$\int_{-\infty}^{\infty} dq_3 \frac{e^{-iq_3(x_3-x'_3)}}{q_{\parallel}^2 + q_3^2} = \frac{\pi}{q_{\parallel}} e^{-q_{\parallel}|x_3-x'_3|} \text{ for } (x_3 - x'_3) < 0 \quad (\text{III.A.51})$$

and it's seen that

$$\int_{-\infty}^{\infty} dq_3 \frac{e^{-iq_3(x_3-x'_3)}}{q_{\parallel}^2 + q_3^2} = \frac{\pi}{q_{\parallel}} e^{-q_{\parallel}|x_3-x'_3|} \text{ for all } (x_3 - x'_3) \quad (\text{III.A.52})$$

The $I_{2D}(\mathbf{q}_{\parallel})$ integral can now be written as

$$I_{2D}(\mathbf{q}_{\parallel}) = \frac{\pi}{q_{\parallel}} \int dx_3 dx'_3 \psi_n^*(x_3) \psi_n(x_3) \psi_n^*(x'_3) \psi_n(x'_3) e^{-q_{\parallel}|x_3-x'_3|} \quad (\text{III.A.53})$$

If we wish to include a screening term, equation (III.A.49) with screening becomes⁷⁶

$$I_{2D}(\mathbf{q}_{\parallel}, q_{sc}) = \int dx_3 dx'_3 \psi_n^*(x_3) \psi_n(x_3) \psi_n^*(x'_3) \psi_n(x'_3) \int_{-\infty}^{\infty} dq_3 \frac{(q_{\parallel}^2 + q_3^2) e^{-iq_3(x_3-x'_3)}}{(q_{\parallel}^2 + q_3^2 + q_{sc}^2)^2} \quad (\text{III.A.54})$$

and the contour integral becomes

$$\begin{aligned} & \int_{-\infty}^{\infty} dq_3 \frac{(q_{\parallel}^2 + q_3^2) e^{-iq_3(x_3-x'_3)}}{(q_{\parallel}^2 + q_3^2 + q_{sc}^2)^2} \\ &= \pi \left[\frac{1}{(q_{\parallel}^2 + q_{sc}^2)^{1/2}} - \frac{|x_3 - x'_3| q_{sc}^2}{2(q_{\parallel}^2 + q_{sc}^2)} - \frac{q_{sc}^2}{2(q_{\parallel}^2 + q_{sc}^2)^{3/2}} \right] e^{-\sqrt{q_{\parallel}^2 + q_{sc}^2} |x_3 - x'_3|} \end{aligned} \quad (\text{III.A.55})$$

Finally, upon substitution the $I_{2D}(\mathbf{q}_{\parallel}, q_{sc})$ integral becomes

$$\begin{aligned} I_{2D}(\mathbf{q}_{\parallel}, q_{sc}) &= \pi \int dx_3 dx'_3 \psi_n^*(x_3) \psi_n(x_3) \psi_n^*(x'_3) \psi_n(x'_3) \\ &\times \left[\frac{1}{(q_{\parallel}^2 + q_{sc}^2)^{1/2}} - \frac{|x_3 - x'_3| q_{sc}^2}{2(q_{\parallel}^2 + q_{sc}^2)} - \frac{q_{sc}^2}{2(q_{\parallel}^2 + q_{sc}^2)^{3/2}} \right] e^{-\sqrt{q_{\parallel}^2 + q_{sc}^2} |x_3 - x'_3|} \end{aligned} \quad (\text{III.A.56})$$

Now consider the energy delta function in equation (III.A.47), which conserves energy. The inner function of the delta function can be simplified as follows

$$\begin{aligned}
E_{n'} + E_{k'} + \hbar\omega_{LO} - E_n - E_k &= 0 \\
\hbar\omega_{LO} - (E_n - E_{n'}) + E_{k'} - E_k &= 0 \\
\hbar\omega'_e + E_{\mathbf{k}_{\parallel}-\mathbf{q}_{\parallel}} - E_k &= 0 \quad \text{where } \hbar\omega'_e = \hbar\omega_{LO} - (E_n - E_{n'}) \\
\hbar\omega'_e + \frac{\hbar^2}{2m} (k_{\parallel}^2 - 2k_{\parallel}q_{\parallel} \cos\theta + q_{\parallel}^2) - E_k &= 0
\end{aligned} \tag{III.A.57}$$

where a similar notation to the given reference has been used.⁷⁷ Note that θ is the angle between \mathbf{k}_{\parallel} and \mathbf{q}_{\parallel} . The expression may be rearranged in terms of the quadratic.

$$\begin{aligned}
\hbar\omega'_e - \frac{\hbar^2}{m} k_{\parallel} q_{\parallel} \cos\theta + \frac{\hbar^2}{2m} q_{\parallel}^2 &= 0 \\
q_{\parallel}^2 - 2k_{\parallel} \cos\theta q_{\parallel} + \frac{2m\omega'_e}{\hbar} &= 0
\end{aligned} \tag{III.A.58}$$

The roots to the quadratic are

$$q_{\parallel\pm e} = k_{\parallel} \cos\theta \pm \sqrt{k_{\parallel}^2 \cos^2\theta - \frac{2m\omega'_e}{\hbar}} \tag{III.A.59}$$

and the following is noted⁷⁷

$$|q_{\parallel+e} - q_{\parallel-e}| = 2\sqrt{k_{\parallel}^2 \cos^2\theta - \frac{2m\omega'_e}{\hbar}} \tag{III.A.60}$$

Using $\delta(f(x)) = \sum_i \delta(x - x_i) / |f'(x_i)|$, where x_i are the roots of $f(x)$, the delta function becomes

$$\begin{aligned}
\delta\left(\frac{\hbar^2}{2m} q_{\parallel}^2 - \frac{\hbar^2}{2m} k_{\parallel} \cos\theta q_{\parallel} + \hbar\omega'_e\right) &= \frac{m}{\hbar^2} \frac{1}{\sqrt{k_{\parallel}^2 \cos^2\theta - \frac{2m\omega'_e}{\hbar}}} [\delta(q_{\parallel} - q_{\parallel+e}) + \delta(q_{\parallel} - q_{\parallel-e})] \\
&= \frac{2m}{\hbar^2} \frac{1}{|q_{\parallel+e} - q_{\parallel-e}|} [\delta(q_{\parallel} - q_{\parallel+e}) + \delta(q_{\parallel} - q_{\parallel-e})]
\end{aligned} \tag{III.A.61}$$

The final expression for the emission case is

$$\begin{aligned}
W_{e^- - \text{phonon}} &= \frac{e^2 \omega_{LO}}{8\pi^2} \left(\frac{1}{\epsilon_\infty} - \frac{1}{\epsilon_{st}} \right) (N_q + 1) \frac{2m}{\hbar^2} \int d\theta \frac{1}{|q_{\parallel+e} - q_{\parallel-e}|} dq_{\parallel} q_{\parallel} I_{2D}(\mathbf{q}_{\parallel}) \\
&\times \left[\delta(q_{\parallel} - q_{\parallel+e}) + \delta(q_{\parallel} - q_{\parallel-e}) \right] \\
&= \frac{e^2 \omega_{LO} m}{4\pi^2 \hbar^2} \left(\frac{1}{\epsilon_\infty} - \frac{1}{\epsilon_{st}} \right) (N_q + 1) \int d\theta \frac{1}{|q_{\parallel+e} - q_{\parallel-e}|} dq_{\parallel} q_{\parallel} I_{2D}(\mathbf{q}_{\parallel}) \left[\delta(q_{\parallel} - q_{\parallel+e}) + \delta(q_{\parallel} - q_{\parallel-e}) \right]
\end{aligned}
\tag{III.A.62}$$

Now consider the different emission cases that are possible. There are three different emission cases that can arise, and are referred to as cases 1a, 1b, and 2.

LO-phonon emission case 1a: $E_k < \hbar\omega'_e = \hbar\omega_{LO} - (E_n - E_{n'})$ and $\hbar\omega'_e > 0$, i.e., $E_n - E_{n'} < \hbar\omega_{LO}$ and the electron does not have sufficient in-plane kinetic energy, the transition is forbidden. The subbands are spaced such that the energy difference is smaller than the LO-phonon energy and the electron does not have enough in-plane kinetic energy, so the transition is forbidden (Figure III.A.5).

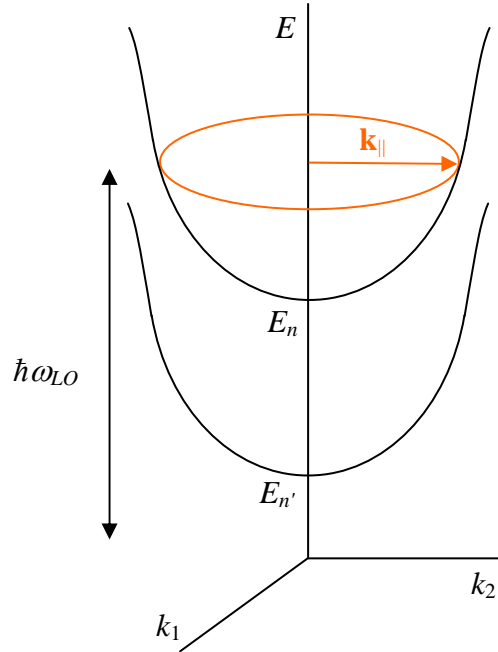


Figure III.A.5. LO-phonon emission case 1a, $E_n - E_{n'} < \hbar\omega_{LO}$ and the electron does not have sufficient in-plane kinetic energy, forbidden transition.

LO-phonon emission case 1b: $E_k \geq \hbar\omega'_e = \hbar\omega_{LO} - (E_n - E_{n'})$ and $\omega'_e > 0$, i.e., $E_n - E_{n'} < \hbar\omega_{LO}$ and the electron has sufficient in-plane kinetic energy, the transition is allowed. The subbands are spaced such that the energy difference is smaller than the LO-phonon energy and the electron has enough in-plane kinetic energy, the transition is allowed assuming no state blocking (Figure III.A.6). The red and blue circles on the $E-k$ diagram are equal energy planes and show the possible range for the in-plane momentum vectors. The final state represented by the blue circle must be vacant, otherwise state blocking will prevent such a transition. There are two possible solutions for this case, $q_{\parallel \pm e}$. Limits on θ are necessary to keep the momentum vectors real valued (to keep from getting a negative sign under the square root). Also note that at resonance the transition is allowed.

$$\theta_{\max e} = \cos^{-1} \left(\sqrt{\frac{2m\omega'_e}{\hbar k_{\parallel}^2}} \right) \quad (\text{III.A.63})$$

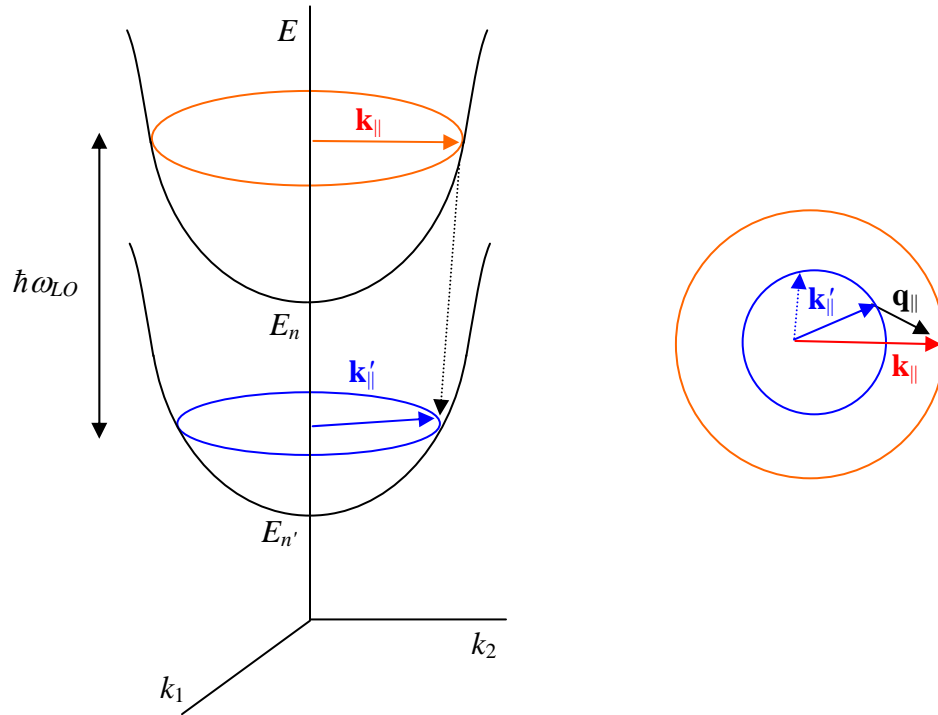


Figure III.A.6. LO-phonon emission case 1b, $E_n - E_{n'} < \hbar\omega_{LO}$ and the electron has sufficient in-plane kinetic energy, allowed transition.

Equation (III.A.62) becomes

$$\begin{aligned}
W_{e^- - \text{phonon}} &= \frac{e^2 \omega_{LO} m}{4\pi^2 \hbar^2} \left(\frac{1}{\epsilon_\infty} - \frac{1}{\epsilon_{st}} \right) (N_q + 1) \int_{-\theta_{\max e}}^{\theta_{\max e}} d\theta \frac{I_{2D}(q_{\parallel+e})q_{\parallel+e} + I_{2D}(q_{\parallel-e})q_{\parallel-e}}{|q_{\parallel+e} - q_{\parallel-e}|} \\
&= \frac{e^2 \omega_{LO} m}{2\pi^2 \hbar^2} \left(\frac{1}{\epsilon_\infty} - \frac{1}{\epsilon_{st}} \right) (N_q + 1) \int_0^{\theta_{\max e}} d\theta \frac{I_{2D}(q_{\parallel+e})q_{\parallel+e} + I_{2D}(q_{\parallel-e})q_{\parallel-e}}{|q_{\parallel+e} - q_{\parallel-e}|}
\end{aligned} \tag{III.A.64}$$

LO-phonon emission case 2: Any E_k is valid and $\omega'_e < 0$, i.e., $E_n - E_{n'} > \hbar\omega_{LO}$, the transition is allowed. The subbands are spaced such that the energy difference is larger than the LO-phonon energy, and the transition is always allowed assuming no state blocking (Figure III.A.7). This “sideways” transition has one solution $q_{\parallel+e}$. When θ is zero (Figure III.A.8) it is seen $q = q_{\parallel+e}$ is the correct root, as q_{\parallel} must be greater than k_{\parallel} .

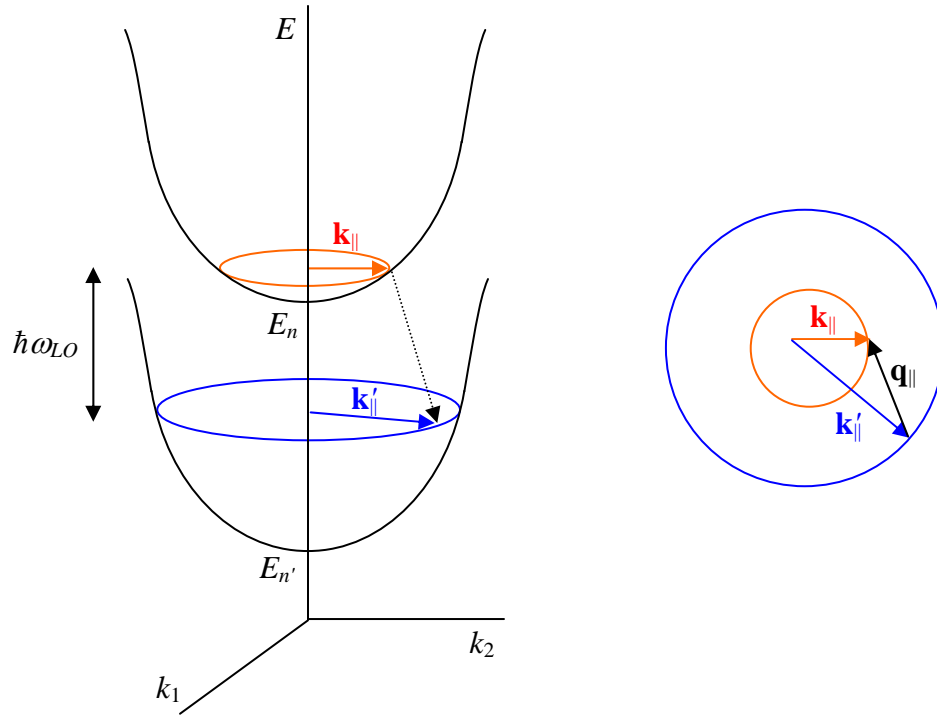


Figure III.A.7. LO-phonon emission case 2, $E_n - E_{n'} > \hbar\omega_{LO}$, “sideways” transition always allowed.

$$|\mathbf{q}_{\parallel+e}| = k_{\parallel} \cos(0) + \sqrt{k_{\parallel}^2 \cos^2(0) - \frac{2m\omega'_e}{\hbar}}$$

Figure III.A.8. LO-phonon emission case 2, \mathbf{q}_{\parallel} and \mathbf{k}_{\parallel} vectors when $\theta = 0$.

Equation (III.A.62) becomes

$$W_{e^{-}\text{-phonon}} = \frac{e^2 \omega_{LO} m}{4\pi^2 \hbar^2} \left(\frac{1}{\varepsilon_{\infty}} - \frac{1}{\varepsilon_{st}} \right) (N_q + 1) \int_0^{2\pi} d\theta \frac{I_{2D}(q_{\parallel+e}) q_{\parallel+e}}{|q_{\parallel+e} - q_{\parallel-e}|} \quad (\text{III.A.65})$$

$$= \frac{e^2 \omega_{LO} m}{2\pi^2 \hbar^2} \left(\frac{1}{\varepsilon_{\infty}} - \frac{1}{\varepsilon_{st}} \right) (N_q + 1) \int_0^{\pi} d\theta \frac{I_{2D}(q_{\parallel+e}) q_{\parallel+e}}{|q_{\parallel+e} - q_{\parallel-e}|}$$

2. LO-Phonon Absorption

The absorption case where $V = V_{e^{-}\text{-phonon}}$, proceeds in a similar manner as for the emission case. The main differences are $N_q + 1 \rightarrow N_q$ and the delta function changes for the conservation of energy for the absorption process. With these changes, similar to equation (III.A.47), the equation for the electron-phonon scattering rate becomes

$$W_{e^{-}\text{-phonon}} = \frac{e^2 \omega_{LO}}{8\pi^2} \left(\frac{1}{\varepsilon_{\infty}} - \frac{1}{\varepsilon_{st}} \right) N_q \int d\theta dq_{\parallel} q_{\parallel} I_{2D}(\mathbf{q}_{\parallel}) \delta(E_{n'} + E_{k'} - \hbar\omega_{LO} - E_n - E_k) \quad (\text{III.A.66})$$

Now the inner function of the delta function can be simplified as follows.

$$\begin{aligned} E_{n'} + E_{k'} - \hbar\omega_{LO} - E_n - E_k &= 0 \\ -\hbar\omega_{LO} - (E_n - E_{n'}) + E_{k'} - E_k &= 0 \\ -\hbar\omega'_a + E_{\mathbf{k}_{\parallel} + \mathbf{q}_{\parallel}} - E_k &= 0 \quad \text{where } \hbar\omega'_a = \hbar\omega_{LO} - (E_{n'} - E_n) \\ -\hbar\omega'_a + \frac{\hbar^2}{2m} (k_{\parallel}^2 - 2k_{\parallel}q_{\parallel} \cos\theta + q_{\parallel}^2) - E_k &= 0 \end{aligned} \quad (\text{III.A.67})$$

Again, θ is the angle between \mathbf{k}_{\parallel} and \mathbf{q}_{\parallel} . The expression may be rearranged in terms of the quadratic.

$$q_{\parallel}^2 - 2k_{\parallel} \cos\theta q_{\parallel} - \frac{2m\omega'_a}{\hbar} = 0 \quad (\text{III.A.68})$$

The roots to the quadratic are

$$q_{\parallel\pm a} = -k_{\parallel} \cos \theta \pm \sqrt{k_{\parallel}^2 \cos^2 \theta + \frac{2m\omega'_a}{\hbar}} \quad (\text{III.A.69})$$

noting that

$$|q_{\parallel+a} - q_{\parallel-a}| = 2\sqrt{k_{\parallel}^2 \cos^2 \theta - \frac{2m\omega'_a}{\hbar}} \quad (\text{III.A.70})$$

The delta function can be simplified using the same identity as used for the emission case, and the delta function becomes

$$\delta\left(\frac{\hbar^2}{2m}q_{\parallel}^2 - \frac{\hbar^2}{2m}k_{\parallel} \cos \theta q_{\parallel} - \hbar\omega'_a\right) = \frac{2m}{\hbar^2} \frac{1}{|q_{\parallel+a} - q_{\parallel-a}|} \left[\delta(q_{\parallel} - q_{\parallel+a}) + \delta(q_{\parallel} - q_{\parallel-a}) \right] \quad (\text{III.A.71})$$

The final expression for the absorption case can be written as

$$\begin{aligned} W_{e^- - \text{phonon}} &= \frac{e^2 \omega_{LO}}{8\pi^2} \left(\frac{1}{\epsilon_{\infty}} - \frac{1}{\epsilon_{st}} \right) N_q \frac{2m}{\hbar^2} \int d\theta \frac{1}{|q_{\parallel+a} - q_{\parallel-a}|} dq_{\parallel} q_{\parallel} I_{2D}(\mathbf{q}_{\parallel}) \\ &\times \left[\delta(q_{\parallel} - q_{\parallel+a}) + \delta(q_{\parallel} - q_{\parallel-a}) \right] \quad (\text{III.A.72}) \\ &= \frac{e^2 \omega_{LO} m}{4\pi^2 \hbar^2} \left(\frac{1}{\epsilon_{\infty}} - \frac{1}{\epsilon_{st}} \right) N_q \int d\theta \frac{1}{|q_{\parallel+a} - q_{\parallel-a}|} dq_{\parallel} q_{\parallel} I_{2D}(\mathbf{q}_{\parallel}) \left[\delta(q_{\parallel} - q_{\parallel+a}) + \delta(q_{\parallel} - q_{\parallel-a}) \right] \end{aligned}$$

Now consider the different absorption cases that are possible. There are four different cases that can arise, and are referred to as cases 1a, 1b, 2, and 3.

LO-phonon absorption case 1a: $E_k < -\hbar\omega'_a = -[\hbar\omega_{LO} - (E_{n'} - E_n)]$ and $\hbar\omega'_a < 0$, i.e., $E_{n'} - E_n > \hbar\omega_{LO}$ and the electron does not have sufficient in-plane kinetic energy, the transition is forbidden (for single phonon absorption). The subbands are spaced such that the energy difference is larger than the LO-phonon energy, and the electron does not have enough in-plane kinetic energy, so the transition is forbidden (Figure III.A.9).

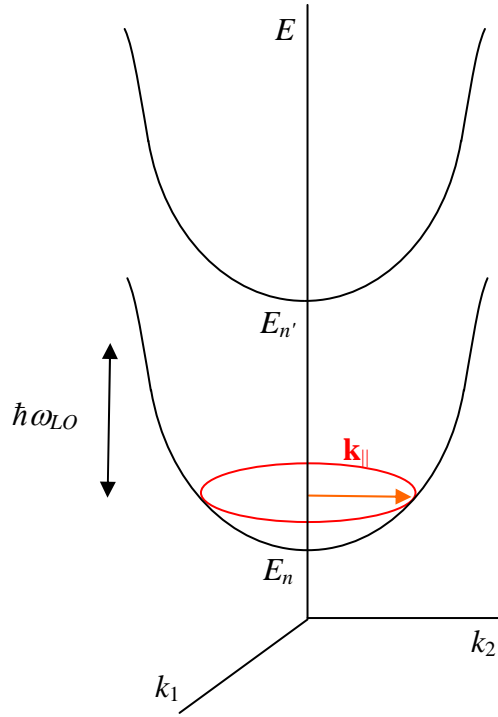


Figure III.A.9. LO-phonon absorption case 1a, $E_{n'} - E_n > \hbar\omega_{LO}$ and the electron does not have sufficient in-plane kinetic energy, forbidden transition.

LO-phonon absorption case 1b: $E_k \geq -\hbar\omega'_a = -[\hbar\omega_{LO} - (E_{n'} - E_n)]$ and $\omega'_a < 0$, i.e., $E_{n'} - E_n > \hbar\omega_{LO}$ and the electron has sufficient in-plane kinetic energy, the transition is allowed. The subbands are spaced such that the energy difference is larger than the LO-phonon energy and the electron has enough in-plane kinetic energy, so the transition is allowed assuming no state blocking (Figure III.A.10). There are two possible solutions for this case, $q_{\parallel \pm a}$. Limits on θ are necessary to keep the momentum vectors real valued (from getting a negative sign under the square root). Also note that at resonance the transition is allowed.

$$\theta_{\max a} = \cos^{-1} \left(\sqrt{\frac{-2m\omega'_a}{\hbar k_{\parallel}^2}} \right) \quad (\text{III.A.73})$$

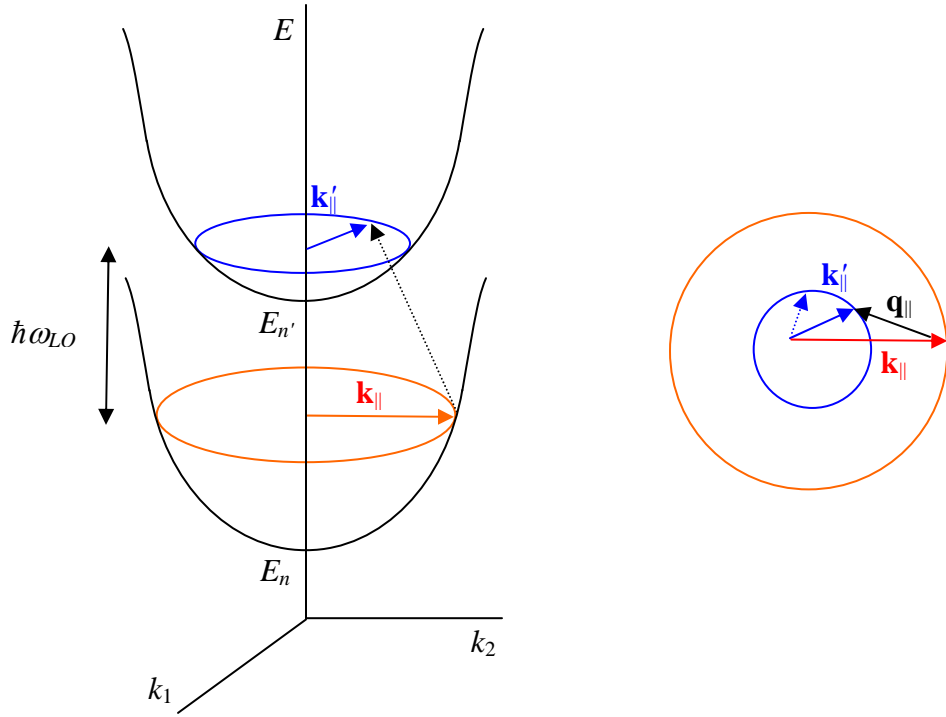


Figure III.A.10. LO-phonon absorption case 1b, $E_{n'} - E_n > \hbar\omega_{LO}$ and the electron has sufficient in-plane kinetic energy, allowed transition.

Equation (III.A.72) becomes

$$\begin{aligned}
 W_{e^- - \text{phonon}} &= \frac{e^2 \omega_{LO} m}{4\pi^2 \hbar^2} \left(\frac{1}{\epsilon_\infty} - \frac{1}{\epsilon_{st}} \right) N_q \int_{-\theta_{\max a}}^{\theta_{\max a}} d\theta \frac{I_{2D}(q_{||+a})q_{||+a} + I_{2D}(q_{||-a})q_{||-a}}{|q_{||+a} - q_{||-a}|} \\
 &= \frac{e^2 \omega_{LO} m}{2\pi^2 \hbar^2} \left(\frac{1}{\epsilon_\infty} - \frac{1}{\epsilon_{st}} \right) N_q \int_0^{\theta_{\max a}} d\theta \frac{I_{2D}(q_{||+a})q_{||+a} + I_{2D}(q_{||-a})q_{||-a}}{|q_{||+a} - q_{||-a}|}
 \end{aligned} \tag{III.A.74}$$

LO-phonon absorption case 2: Any E_k is valid and $\omega'_a > 0$, i.e., $E_{n'} - E_n < \hbar\omega_{LO}$, the transition is allowed. The subbands are spaced such that the energy difference is smaller than the phonon energy so the transition is always allowed assuming no state blocking (Figure III.A.11). This “sideways” transition has one solution $q_{||+a}$ which again can be seen when θ is zero.

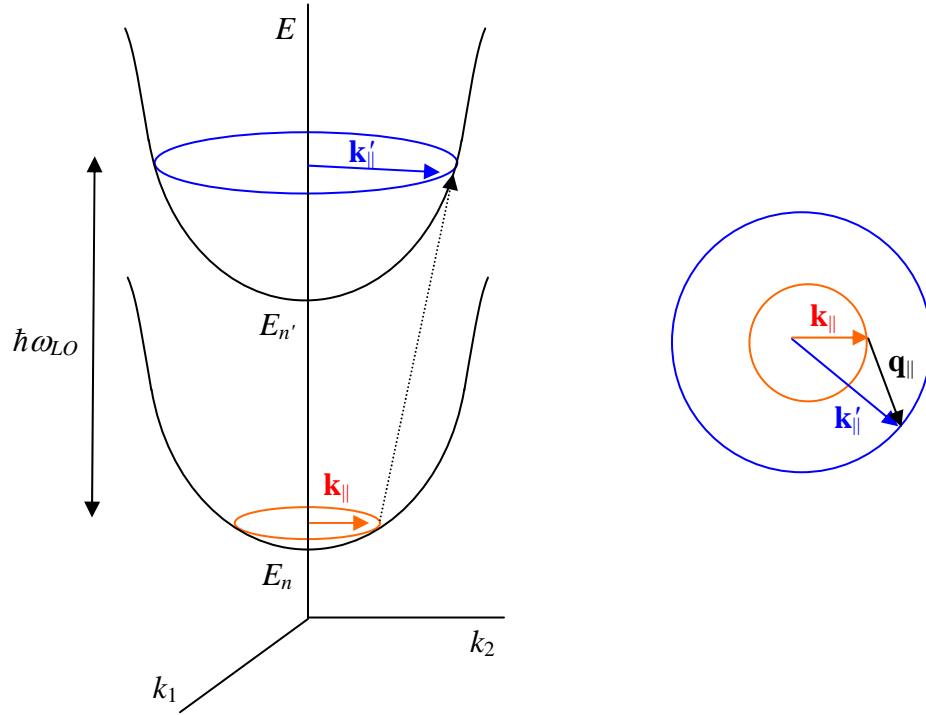


Figure III.A.11. LO-phonon absorption case 2, $E_{n'} - E_n < \hbar\omega_{LO}$, “sideways” transition always allowed.

Equation (III.A.72) becomes

$$\begin{aligned}
 W_{e^- - \text{phonon}} &= \frac{e^2 \omega_{LO} m}{4\pi^2 \hbar^2} \left(\frac{1}{\epsilon_\infty} - \frac{1}{\epsilon_{st}} \right) N_q \int_0^{2\pi} d\theta \frac{I_{2D}(q_{||+a}) q_{||+a}}{|q_{||+a} - q_{||-a}|} \\
 &= \frac{e^2 \omega_{LO} m}{2\pi^2 \hbar^2} \left(\frac{1}{\epsilon_\infty} - \frac{1}{\epsilon_{st}} \right) N_q \int_0^\pi d\theta \frac{I_{2D}(q_{||+a}) q_{||+a}}{|q_{||+a} - q_{||-a}|}
 \end{aligned} \tag{III.A.75}$$

LO-phonon absorption case 3: Any E_k is valid and $\omega'_a > 0$, and $E_{n'} - E_n < 0$, the transition is allowed. Absorption from an upper band edge to a lower band edge is always allowed assuming no state blocking (Figure III.A.12). This “upwards” transition has one solution $q_{||+a}$. Phonon absorption scattering rates (all cases) are much slower than phonon emission scattering rates at low temperatures. This is because a phonon must be present to be absorbed. Further for case 3, absorption via a large momentum transfer also reduces the scattering rate.

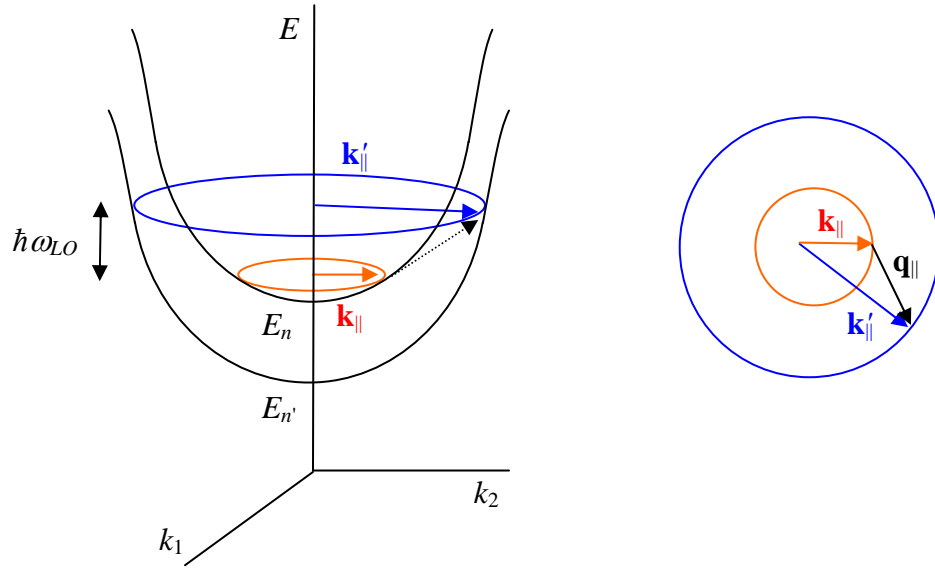


Figure III.A.12. LO-phonon absorption case 3, “upwards” transition always allowed.

Equation (III.A.72) again takes the same form as equation (III.A.75).

3. Mean Scattering Rate

Because there is a distribution of carrier energies in the initial state, the mean scattering rate is calculated by averaging over the Fermi-Dirac distribution of carriers in the initial state

$$W_{e^{-}\text{-phonon, mean}} = \frac{\int dE_{k_i} W_{e^{-}\text{-phonon}, i} f_{FD, i}(k_i) [1 - f_{FD, f}(k_f)]}{\int dE_{k_i} f_{FD, i}(k_i)} \quad (\text{III.A.76})$$

where state blocking has also been included, and the electron-phonon scattering rate for both emission and absorption can be written succinctly as

$$W_{e^{-}\text{-phonon}} = \frac{e^2 \omega_{LO} m}{4\pi^2 \hbar^2} \left(\frac{1}{\epsilon_{\infty}} - \frac{1}{\epsilon_{st}} \right) \left\{ \begin{array}{l} (N_q + 1)^{(emission)} \\ N_q^{(absorption)} \end{array} \right\} \int d\theta \frac{1}{|q_{||+} - q_{||-}|} dq_{||} q_{||} I_{2D}(\mathbf{q}_{||}) \times [\delta(q_{||} - q_{||+}) + \delta(q_{||} - q_{||-})] \quad (\text{III.A.77})$$

The populations and electron temperatures can vary greatly between the subbands, and these can only be determined by analyzing the entire QC structure. Modeling the entire structure using Monte Carlo simulations will be discussed later.

B. ELECTRON-ELECTRON SCATTERING

Carrier-carrier scattering is a mechanism that can be significant, particularly for closely spaced energy states. When the energy spacing between states is smaller than the LO-phonon energy, LO-phonon scattering is forbidden except for electrons that have sufficiently high in-plane kinetic energy. Because of this, the mean electron-phonon scattering rate will be reduced. Electron-electron scattering, as well as other single electron scattering mechanisms (such as impurity and interface roughness scattering), may then be the dominant scattering mechanisms. Intraband electron-electron scattering along with LO-phonon scattering, must be modeled in order to determine the thermal electron distributions within subbands. For these reasons, modeling electron-electron scattering is important.

The following diagram (Figure III.B.1) shows the indexing used for electron-electron scattering, where the electrons can be right or left handed, and i and j are the initial states and f and g are the final states.

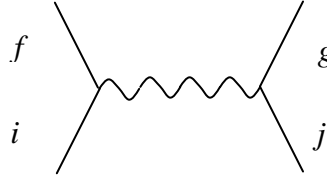


Figure III.B.1. Feynman diagram for electron-electron scattering.

Spin independent interactions combined with the Pauli exclusion principle lead to a term in the form of $\mathbf{S}_1 \cdot \mathbf{S}_2$, because $\mathbf{S}^2 = (\mathbf{S}_1 + \mathbf{S}_2)^2 = \mathbf{S}_1^2 + 2\mathbf{S}_1 \cdot \mathbf{S}_2 + \mathbf{S}_2^2$. The spatial part of the wavefunction can be either symmetric or antisymmetric.

$$\begin{aligned}
 |\psi_S\rangle &= \frac{1}{\sqrt{2}} (|k'\rangle|k''\rangle + |k''\rangle|k'\rangle) \\
 |\psi_A\rangle &= \frac{1}{\sqrt{2}} (|k'\rangle|k''\rangle - |k''\rangle|k'\rangle)
 \end{aligned}
 \tag{III.B.1}$$

The total wavefunction is the product of the spinor that describe the possible spin states of the two electrons and the spatial part. Since the electrons are fermions, the total

wavefunction must be antisymmetric under simultaneous exchange of both the spin and spatial parts. Using Pauli spin matrices

$$\sigma^1 = \begin{pmatrix} 0 & 1 \\ 1 & 0 \end{pmatrix}, \quad \sigma^2 = \begin{pmatrix} 0 & -i \\ i & 0 \end{pmatrix}, \quad \sigma^3 = \begin{pmatrix} 1 & 0 \\ 0 & -1 \end{pmatrix} \quad (\text{III.B.2})$$

the spin can be written in the usual way as

$$\mathbf{S} = \frac{1}{2} \boldsymbol{\sigma} \quad (\text{III.B.3})$$

The permutation operator $P_{12} = P_{12}^{(spin)} P_{12}^{(space)}$ has eigenvalue of 1 for the symmetric case and -1 for the antisymmetric case. For a two electron system, the eigenvalue for the $\mathbf{S}_1 \cdot \mathbf{S}_2$ triplet symmetric states is $1/4$ and for the singlet antisymmetric state $-3/4$. This allows the permutation operator for the spin to be written as^{72,78}

$$P_{12}^{(spin)} = \frac{1}{2} (1 + 4\mathbf{S}_1 \cdot \mathbf{S}_2) \quad (\text{III.B.4})$$

which can be rearranged to get

$$2P_{12}^{(spin)} - 1 = 4\mathbf{S}_1 \cdot \mathbf{S}_2 \quad (\text{III.B.5})$$

Since

$$\mathbf{S}_1 \cdot \mathbf{S}_2 = \frac{1}{4} \boldsymbol{\sigma}_1 \cdot \boldsymbol{\sigma}_2 \quad (\text{III.B.6})$$

the Pauli matrices are related to the exchange operator by (subscripts are the particle numbers)

$$\boldsymbol{\sigma}_1 \cdot \boldsymbol{\sigma}_2 = 2P_{12}^{(spin)} - 1 \quad (\text{III.B.7})$$

The total spin and square of the total spin is

$$\mathbf{S} = \frac{1}{2} \boldsymbol{\sigma}_1 + \frac{1}{2} \boldsymbol{\sigma}_2 \quad (\text{III.B.8})$$

$$\mathbf{S} \cdot \mathbf{S} = \frac{3}{2} + \frac{1}{2} \boldsymbol{\sigma}_1 \cdot \boldsymbol{\sigma}_2 \quad (\text{III.B.9})$$

From (III.B.9) and (III.B.7) the following is found

$$\mathbf{S} \cdot \mathbf{S} = 1 + \frac{1}{2} + \frac{1}{2} \boldsymbol{\sigma}_1 \cdot \boldsymbol{\sigma}_2 = P_{12}^{(spin)} + 1 \quad (\text{III.B.10})$$

The total spin for the symmetric case is 1 and for the antisymmetric case 0 (the eigenvalues of $\sigma_1 \cdot \sigma_2$ are 1 for the symmetric case and -3 for the antisymmetric case). The total wavefunction may be written as

$$|\psi_S\rangle = |\xi^0 \psi_S\rangle \quad \text{and} \quad |\psi_A\rangle = |\xi^1 \psi_A\rangle \quad (\text{III.B.11})$$

Electrons are indistinguishable particles. Denoting the matrix element as M , the following subscript notation is used.

$$\begin{aligned} M_{12} &= M_{ij \rightarrow fg} \\ M_{21} &= M_{ij \rightarrow gf} \end{aligned} \quad (\text{III.B.12})$$

Antiparallel spin electrons do not interfere while parallel spin electrons do interfere. This is because Pauli's exclusion principle states that no two electrons with the same quantum numbers (including spin), can occupy the same space. Since antiparallel spin electrons do not change sign upon exchange, the square of matrix element for the antiparallel spin case can be written as

$$M_a^2 = |M_{12}|^2 + |M_{21}|^2 \quad (\text{III.B.13})$$

Parallel spin electrons interfere and the wavefunction changes sign upon exchange. Thus, the square of the matrix element for the parallel spin case may be written as⁷⁹

$$M_p^2 = |M_{12} - M_{21}|^2 = M_a^2 - 2M_{12}M_{21} \quad (\text{III.B.14})$$

where the minus sign comes about from the exchange. The matrix element is the same as that for the antiparallel case, except for the additional exchange term (negative signed quantity). This exchange effect results in a lowering of the scattering rate for parallel spin electrons as compared to the antiparallel case.

If we assume equal distributions of antiparallel and parallel spins, the matrix element may first be written by including the $\frac{1}{2}$ probability factors as

$$M'^2 = \frac{1}{2}M_a^2 + \frac{1}{2}M_p^2 = M_a^2 - M_{12}M_{21} \quad (\text{III.B.15})$$

Now since $M_{ij \rightarrow fg} = M_{ij \rightarrow gf}$, an additional $\frac{1}{2}$ factor must be included to keep from double counting.

$$M^2 = \frac{1}{2}M'^2 = \frac{1}{2}(M_a^2 - M_{12}M_{21}) = \frac{1}{2}(M_{12}M_{12} + M_{21}M_{21} - M_{12}M_{21}) \quad (\text{III.B.16})$$

1. Antiparallel Spins

The first case considered is where the electrons are assumed to have antiparallel spins, so no interference occurs and the form of equation (III.B.13) applies. All of the vectors (\mathbf{k} vectors) in this section represent parallel component vectors (\mathbf{k}_{\parallel}) and the parallel subscript has been dropped to simplify the notation. The perturbing potential for the electron-electron scattering interaction is the Coulombic potential $V = V_{Coulomb}$. Working in the Born approximation and in the $\langle \mathbf{x} |$ representation, the following matrix element is computed where $(x_1, x_2, x_3) = (x, y, z)$ with x_1, x_2 parallel to the growth direction x_3 .

$$\begin{aligned} \langle f, g | V | i, j \rangle &= \langle f, g | \frac{\alpha}{\epsilon |\mathbf{x} - \mathbf{x}'|} | i, j \rangle \\ &= \frac{\alpha}{\epsilon A^2} \int d^2 x_{\parallel} d^2 x'_{\parallel} dx_3 dx'_3 \psi_f^*(x_3) \psi_i(x_3) \psi_g^*(x'_3) \psi_j(x'_3) \frac{e^{i[(\mathbf{k}_i \cdot \mathbf{x}_{\parallel} + \mathbf{k}_j \cdot \mathbf{x}'_{\parallel}) - (\mathbf{k}_f \cdot \mathbf{x}_{\parallel} + \mathbf{k}_g \cdot \mathbf{x}'_{\parallel})]}}{|\mathbf{x} - \mathbf{x}'|} \end{aligned} \quad (\text{III.B.17})$$

This can be rewritten as follows, showing explicitly the x_3 and in-plane parts of the integral separately.

$$= \frac{\alpha}{\epsilon A^2} \int dx_3 dx'_3 \psi_f^*(x_3) \psi_i(x_3) \psi_g^*(x'_3) \psi_j(x'_3) \int d^2 x_{\parallel} d^2 x'_{\parallel} \frac{e^{i[(\mathbf{k}_i \cdot \mathbf{x}_{\parallel} + \mathbf{k}_j \cdot \mathbf{x}'_{\parallel}) - (\mathbf{k}_f \cdot \mathbf{x}_{\parallel} + \mathbf{k}_g \cdot \mathbf{x}'_{\parallel})]}}{\sqrt{|\mathbf{x}_{\parallel} - \mathbf{x}'_{\parallel}|^2 + (x_3 - x'_3)^2}} \quad (\text{III.B.18})$$

In order to simplify this expression, the in-plane part which is essentially a 2D Fourier transform can be evaluated first. This can be done as follows. The in-plane part can be written as

$$\int d^2 x_{\parallel} d^2 x'_{\parallel} \frac{e^{i[(\mathbf{k}_i \cdot \mathbf{x}_{\parallel} + \mathbf{k}_j \cdot \mathbf{x}'_{\parallel}) - (\mathbf{k}_f \cdot \mathbf{x}_{\parallel} + \mathbf{k}_g \cdot \mathbf{x}'_{\parallel})]}}{\sqrt{|\mathbf{x}_{\parallel} - \mathbf{x}'_{\parallel}|^2 + (x_3 - x'_3)^2}} = \int d^2 x_{\parallel} d^2 x'_{\parallel} \frac{e^{i\Delta\mathbf{k} \cdot \mathbf{x}_{\parallel} + i\Delta\mathbf{k}' \cdot \mathbf{x}'_{\parallel}}}{\sqrt{|\mathbf{x}_{\parallel} - \mathbf{x}'_{\parallel}|^2 + (x_3 - x'_3)^2}} \quad (\text{III.B.19})$$

where $\Delta\mathbf{k} = \mathbf{k}_i - \mathbf{k}_f$ and $\Delta\mathbf{k}' = \mathbf{k}_j - \mathbf{k}_g$. Using the following Bessel function identity^{80,81}

$$\frac{1}{\sqrt{|\mathbf{x}_{\parallel} - \mathbf{x}'_{\parallel}|^2 + (x_3 - x'_3)^2}} = \int_0^{\infty} dq_{\parallel} e^{-q_{\parallel}|x_3 - x'_3|} J_0(q_{\parallel} |\mathbf{x}_{\parallel} - \mathbf{x}'_{\parallel}|) \quad (\text{III.B.20})$$

the expression becomes

$$\begin{aligned}
& \int d^2 x_{\parallel} d^2 x'_{\parallel} \frac{e^{i[(\mathbf{k}_i \cdot \mathbf{x}_{\parallel} + \mathbf{k}_j \cdot \mathbf{x}'_{\parallel}) - (\mathbf{k}_f \cdot \mathbf{x}_{\parallel} + \mathbf{k}_g \cdot \mathbf{x}'_{\parallel})]}}{\sqrt{|\mathbf{x}_{\parallel} - \mathbf{x}'_{\parallel}|^2 + (x_3 - x'_3)^2}} = \int d^2 x_{\parallel} d^2 x'_{\parallel} e^{i\Delta\mathbf{k} \cdot \mathbf{x}_{\parallel} + i\Delta\mathbf{k}' \cdot \mathbf{x}'_{\parallel}} \int_0^{\infty} dq_{\parallel} e^{-q_{\parallel} |x_3 - x'_3|} J_0(q_{\parallel} |\mathbf{x}_{\parallel} - \mathbf{x}'_{\parallel}|) \\
& = \int_0^{\infty} \int d^2 x_{\parallel} d^2 x'_{\parallel} dq_{\parallel} e^{i\Delta\mathbf{k} \cdot (\mathbf{x}_{\parallel} - \mathbf{x}'_{\parallel}) + i\Delta\mathbf{k} \cdot \mathbf{x}'_{\parallel} + i\Delta\mathbf{k}' \cdot \mathbf{x}'_{\parallel}} e^{-q_{\parallel} |x_3 - x'_3|} J_0(q_{\parallel} |\mathbf{x}_{\parallel} - \mathbf{x}'_{\parallel}|)
\end{aligned} \tag{III.B.21}$$

Now define $\boldsymbol{\rho} = \mathbf{x}_{\parallel} - \mathbf{x}'_{\parallel}$, and note that $d^2 x_{\parallel} = |d\mathbf{x}_{\parallel}| = |d(\mathbf{x}_{\parallel} - \mathbf{x}'_{\parallel})| = |d\boldsymbol{\rho}|$ since \mathbf{x}'_{\parallel} is constant with respect to the $|d\mathbf{x}_{\parallel}|$ integration, thus $d^2 x_{\parallel} = |d\boldsymbol{\rho}| = d\phi d\rho$

$$\begin{aligned}
& = \int_0^{\infty} \int d^2 x'_{\parallel} dq_{\parallel} e^{i(\Delta\mathbf{k} + \Delta\mathbf{k}') \cdot \mathbf{x}'_{\parallel}} e^{-q_{\parallel} |x_3 - x'_3|} \int d\phi d\rho e^{i\Delta\mathbf{k} \cdot \boldsymbol{\rho}} J_0(q_{\parallel} \rho) \\
& = \int_0^{\infty} \int d^2 x'_{\parallel} dq_{\parallel} e^{i(\Delta\mathbf{k} + \Delta\mathbf{k}') \cdot \mathbf{x}'_{\parallel}} e^{-q_{\parallel} |x_3 - x'_3|} \int d\phi d\rho e^{i\Delta\mathbf{k} \cdot \boldsymbol{\rho} \cos \phi} J_0(q_{\parallel} \rho)
\end{aligned} \tag{III.B.22}$$

Using the following equations⁸²

$$\int_0^{2\pi} d\phi e^{i\Delta k \rho \cos \phi - im\phi} = 2\pi i^m J_m(\Delta k \rho) \tag{III.B.23}$$

with $m = 0$ this becomes

$$\int_0^{2\pi} d\phi e^{i\Delta k \rho \cos \phi} = 2\pi J_0(\Delta k \rho) \tag{III.B.24}$$

and

$$\int_0^{\infty} \rho d\rho J_0(\Delta k \rho) J_0(q_{\parallel} \rho) = \frac{1}{q_{\parallel}} \delta(q_{\parallel} - \Delta k) \tag{III.B.25}$$

the equation now becomes

$$\begin{aligned}
& \int d^2 x_{\parallel} d^2 x'_{\parallel} \frac{e^{i[(\mathbf{k}_i \cdot \mathbf{x}_{\parallel} + \mathbf{k}_j \cdot \mathbf{x}'_{\parallel}) - (\mathbf{k}_f \cdot \mathbf{x}_{\parallel} + \mathbf{k}_g \cdot \mathbf{x}'_{\parallel})]}}{\sqrt{|\mathbf{x}_{\parallel} - \mathbf{x}'_{\parallel}|^2 + (x_3 - x'_3)^2}} \\
& = \int_0^{\infty} \int d^2 x'_{\parallel} dq_{\parallel} e^{i(\Delta\mathbf{k} + \Delta\mathbf{k}') \cdot \mathbf{x}'_{\parallel}} e^{-q_{\parallel} |x_3 - x'_3|} 2\pi \int_0^{\infty} \rho d\rho e^{i\Delta\mathbf{k} \cdot \boldsymbol{\rho}} J_0(\Delta k \rho) J_0(q_{\parallel} \rho) \\
& = \int_0^{\infty} \int d^2 x'_{\parallel} dq_{\parallel} e^{i(\Delta\mathbf{k} + \Delta\mathbf{k}') \cdot \mathbf{x}'_{\parallel}} e^{-q_{\parallel} |x_3 - x'_3|} 2\pi \frac{1}{q_{\parallel}} \delta(q_{\parallel} - \Delta k) \\
& = \frac{2\pi}{q_{\parallel}} e^{-q_{\parallel} |x_3 - x'_3|} \int d^2 x'_{\parallel} e^{i(\Delta\mathbf{k} + \Delta\mathbf{k}') \cdot \mathbf{x}'_{\parallel}}
\end{aligned} \tag{III.B.26}$$

with $q_{\parallel} = \Delta k = |\mathbf{k}_i - \mathbf{k}_j|$ from evaluating the integral with the delta function. Now from the d^2x_{\parallel} integral which has finite limits of integration, $\Delta \mathbf{k} = \Delta \mathbf{k}'$ is the only value such that the integral will be nonvanishing, which yields a delta function representing the conservation of momentum.

$$\begin{aligned} & \int d^2x_{\parallel} d^2x'_{\parallel} \frac{e^{i[(\mathbf{k}_i \cdot \mathbf{x}_{\parallel} + \mathbf{k}_j \cdot \mathbf{x}'_{\parallel}) - (\mathbf{k}_f \cdot \mathbf{x}_{\parallel} + \mathbf{k}_g \cdot \mathbf{x}'_{\parallel})]}}{\sqrt{|\mathbf{x}_{\parallel} - \mathbf{x}'_{\parallel}|^2 + (x_3 - x'_3)^2}} \\ &= \frac{2\pi}{q_{\parallel}} e^{-q_{\parallel}|x_3 - x'_3|} A \delta(\Delta \mathbf{k} + \Delta \mathbf{k}') = \frac{2\pi A}{q_{\parallel}} e^{-q_{\parallel}|x_3 - x'_3|} \delta(\mathbf{k}_f + \mathbf{k}_g - \mathbf{k}_i - \mathbf{k}_j) \end{aligned} \quad (\text{III.B.27})$$

This agrees with the given reference.⁷⁶ This expression can now be substituted back into the original matrix element to arrive at

$$\begin{aligned} \langle f, g | V | i, j \rangle &= \frac{2\pi\alpha A}{\varepsilon A^2 q_{\parallel}} \int dx_3 dx'_3 \psi_f^*(x_3) \psi_i(x_3) \psi_g^*(x'_3) \psi_j(x'_3) e^{-q_{\parallel}|x_3 - x'_3|} \\ &\times \delta(\mathbf{k}_f + \mathbf{k}_g - \mathbf{k}_i - \mathbf{k}_j) \end{aligned} \quad (\text{III.B.28})$$

which can be rewritten in the usual notation as (noting $\alpha = e^2/4\pi$)

$$\langle f, g | V | i, j \rangle = \frac{e^2}{2\varepsilon A q_{\parallel}} A_{ifg}(q_{\parallel}) \delta(\mathbf{k}_f + \mathbf{k}_g - \mathbf{k}_i - \mathbf{k}_j) \quad (\text{III.B.29})$$

where

$$A_{ifg}(q_{\parallel}) = \int dx_3 dx'_3 \psi_f^*(x_3) \psi_i(x_3) \psi_g^*(x'_3) \psi_j(x'_3) e^{-q_{\parallel}|x_3 - x'_3|} \quad (\text{III.B.30})$$

and again $q_{\parallel} = \Delta k = |\mathbf{k}_i - \mathbf{k}_j|$.

The scattering rate can be found by substituting the above matrix element into Fermi's golden rule summing over the final states f and g . Inserting \hbar and c back into the equations

$$\begin{aligned} W_{e^-e^-} &= \frac{2\pi}{\hbar} \sum_{f,g} |\langle f, g | V | i, j \rangle|^2 \delta \left[E_f + \frac{\hbar^2 k_f^2}{2m} + E_g + \frac{\hbar^2 k_g^2}{2m} - \left(E_i + \frac{\hbar^2 k_i^2}{2m} \right) - \left(E_j + \frac{\hbar^2 k_j^2}{2m} \right) \right] \\ &= \frac{2\pi}{\hbar} \left(\frac{e^2}{2\varepsilon A} \right)^2 \sum_{f,g} \left| \frac{A_{ifg}(q_{\parallel})}{q_{\parallel}} \right|^2 \delta(\mathbf{k}_f + \mathbf{k}_g - \mathbf{k}_i - \mathbf{k}_j) \delta(E_{Tf} + E_{Tg} - E_{Ti} - E_{Tj}) \end{aligned} \quad (\text{III.B.31})$$

where E_T is total energy, i.e., the subband edge plus the in-plane kinetic energy. Converting the final states summations to integrals in \mathbf{k} -space

$$\begin{aligned}
W_{e^-e^-} &= \frac{\pi e^4}{\hbar 2 \varepsilon^2 A^2} \frac{A}{(2\pi)^2} \frac{A}{(2\pi)^2} \int d^2 k_f d^2 k_g \left| \frac{A_{ifg}(q_{\parallel})}{q_{\parallel}} \right|^2 \delta(\mathbf{k}_f + \mathbf{k}_g - \mathbf{k}_i - \mathbf{k}_j) \\
&\times \delta(E_{Tf} + E_{Tg} - E_{Ti} - E_{Tj}) \tag{III.B.32} \\
&= \frac{e^4}{32\pi^3 \hbar \varepsilon^2} \int d^2 k_f d^2 k_g \left| \frac{A_{ifg}(q_{\parallel})}{q_{\parallel}} \right|^2 \delta(\mathbf{k}_f + \mathbf{k}_g - \mathbf{k}_i - \mathbf{k}_j) \delta(E_{Tf} + E_{Tg} - E_{Ti} - E_{Tj})
\end{aligned}$$

Integrating over all the states of the j index electron and including Fermi-Dirac functions to take into account the occupancy distributions

$$\begin{aligned}
W_{e^-e^-} &= \frac{e^4}{32\pi^3 \hbar \varepsilon^2} \int d^2 k_f d^2 k_g d^2 k_j \left| \frac{A_{ifg}(q_{\parallel})}{q_{\parallel}} \right|^2 [1 - f_{FD,f}(k_f)] [1 - f_{FD,g}(k_g)] f_{FD,j}(k_j) \\
&\times \delta(\mathbf{k}_f + \mathbf{k}_g - \mathbf{k}_i - \mathbf{k}_j) \delta(E_{Tf} + E_{Tg} - E_{Ti} - E_{Tj}) \tag{III.B.33}
\end{aligned}$$

Grouping the occupancy distribution functions into one term F_{ifg} , and evaluating the $d^2 k_g$ integral to get rid of the momentum delta function

$$\begin{aligned}
W_{e^-e^-} &= \frac{e^4}{32\pi^3 \hbar \varepsilon^2} \int d^2 k_f d^2 k_j \left| \frac{A_{ifg}(q_{\parallel})}{q_{\parallel}} \right|^2 F_{ifg} \\
&\times \delta \left(E_f + \frac{\hbar^2 k_f^2}{2m} + E_g + \frac{\hbar^2 k_g^2}{2m} - E_i - \frac{\hbar^2 k_i^2}{2m} - E_j - \frac{\hbar^2 k_j^2}{2m} \right) \\
&= \frac{2m}{\hbar^2} \frac{e^4}{32\pi^3 \hbar \varepsilon^2} \int d^2 k_f d^2 k_j \left| \frac{A_{ifg}(q_{\parallel})}{q_{\parallel}} \right|^2 F_{ifg} \delta \left[k_f^2 + k_g^2 - k_i^2 - k_j^2 + \frac{2m}{\hbar^2} (E_f + E_g - E_i - E_j) \right] \\
&= \frac{me^4}{16\pi^3 \hbar^3 \varepsilon^2} \int d^2 k_f d^2 k_j \left| \frac{A_{ifg}(q_{\parallel})}{q_{\parallel}} \right|^2 F_{ifg} \delta \left[k_f^2 + k_g^2 - k_i^2 - k_j^2 + \frac{2m}{\hbar^2} (E_f + E_g - E_i - E_j) \right] \tag{III.B.34}
\end{aligned}$$

This equation gives the scattering rate of an electron with momentum vector \mathbf{k}_i averaged over the other initial particle states \mathbf{k}_j . Since \mathbf{k}_g can be written in terms of the other three momentum vectors, the only unknown is \mathbf{k}_f and this can be determined as follows by using relative momentum vectors^{76,53}

$$\mathbf{k}_{ij} = \mathbf{k}_j - \mathbf{k}_i \tag{III.B.35}$$

$$\mathbf{k}_{fg} = \mathbf{k}_g - \mathbf{k}_f \tag{III.B.36}$$

In this scheme, we look to replace the integration over d^2k_f with an integral over d^2k_{fg} .

The following can now be written for \mathbf{k}_f

$$\mathbf{k}_f = \mathbf{k}_i + \mathbf{k}_j - \mathbf{k}_g = \mathbf{k}_i + \mathbf{k}_j - \mathbf{k}_{fg} - \mathbf{k}_f = \frac{1}{2}(\mathbf{k}_i + \mathbf{k}_j - \mathbf{k}_{fg}) \quad (\text{III.B.37})$$

Since \mathbf{k}_{fg} is the only one of the two relative vectors that is a function of \mathbf{k}_f

$$dk_{f,x_1} = -\frac{1}{2}dk_{fg,x_1} \quad (\text{III.B.38})$$

$$dk_{f,x_2} = -\frac{1}{2}dk_{fg,x_2} \quad (\text{III.B.39})$$

and thus^{83,84}

$$d^2k_f = dk_{f,x_1}dk_{f,x_2} = \left(-\frac{1}{2}dk_{fg,x_1}\right)\left(-\frac{1}{2}dk_{fg,x_2}\right) = \frac{1}{4}d^2k_{fg} \quad (\text{III.B.40})$$

as originally shown in the given reference.⁸³ Now $d^2k_{fg} = d\theta k_{fg}dk_{fg}$, where θ is defined in Figure III.B.2, using notation similar to the given reference.⁵³

It is often reasonable to approximate that the occupancy of the final states f and g are small, and ignore state blocking. This effectively means that $F_{jfg} \sim f_{FD,j}(k_j)$ since $f_{FD,f} = f_{FD,g} \sim 0$. Including state blocking decreases the scattering rate only if the densities in the final states are appreciable. In order to solve for $q_{||}$, the law of cosines is used as follows

$$\begin{aligned} k_{sum\ ij}^2 &= k_i^2 + k_j^2 - 2k_i k_j \cos(\pi - \alpha_1) \\ &= k_i^2 + k_j^2 + 2k_i k_j \cos(\alpha_1) \end{aligned} \quad (\text{III.B.41})$$

$$\begin{aligned} k_{sum\ ij}^2 &= k_f^2 + k_g^2 - 2k_f k_g \cos(\pi - \beta) \\ &= k_f^2 + k_g^2 + 2k_f k_g \cos(\beta) \end{aligned} \quad (\text{III.B.42})$$

and

$$k_{ij}^2 = k_i^2 + k_j^2 - 2k_i k_j \cos(\alpha_1) \quad (\text{III.B.43})$$

$$k_{fg}^2 = k_f^2 + k_g^2 - 2k_f k_g \cos(\beta) \quad (\text{III.B.44})$$

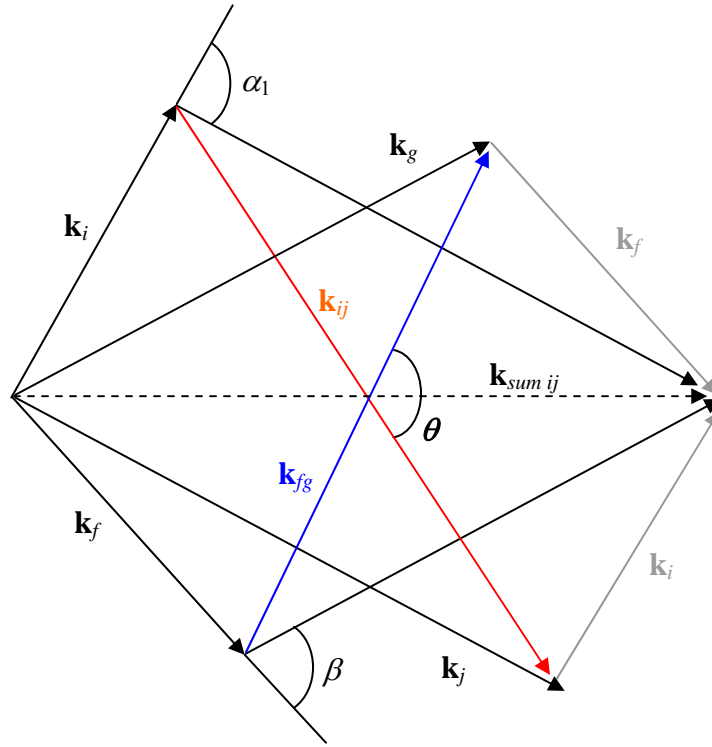


Figure III.B.2. Momentum vectors used in the calculation of the electron-electron scattering rate.

Summing equations (III.B.41) and (III.B.43) and summing equations (III.B.42) and (III.B.44)

$$k_{sum\ ij}^2 + k_{ij}^2 = 2k_i^2 + 2k_j^2 \quad (III.B.45)$$

$$k_{sum\ ij}^2 + k_{fg}^2 = 2k_f^2 + 2k_g^2 \quad (III.B.46)$$

Substituting equations (III.B.44) and (III.B.45) to get rid of $k_{sum\ ij}^2$

$$k_{fg}^2 = k_{ij}^2 + 2(k_f^2 + k_g^2 - k_i^2 - k_j^2) \quad (III.B.47)$$

The energy delta function yields conservation of energy.

$$E_f + \frac{\hbar^2 k_f^2}{2m} + E_g + \frac{\hbar^2 k_g^2}{2m} = E_i + \frac{\hbar^2 k_i^2}{2m} + E_j + \frac{\hbar^2 k_j^2}{2m} \quad (III.B.48)$$

$$k_f^2 + k_g^2 - k_i^2 - k_j^2 = \frac{2m}{\hbar^2} (E_i + E_j - E_f - E_g) \quad (III.B.49)$$

Substituting equation (III.B.49) into (III.B.47)

$$k_{fg}^2 = k_{ij}^2 + \frac{4m}{\hbar^2}(E_i + E_j - E_f - E_g) = k_{ij}^2 + k_o^2 \quad (\text{III.B.50})$$

using the usual definition $k_o^2 = 4m/\hbar^2(E_i+E_j-E_f-E_g)$. Recall from the definitions of q_{\parallel} , k_{ij} , and k_{fg} , we may write

$$q_{\parallel} = |\mathbf{k}_i - \mathbf{k}_f| = \frac{|\mathbf{k}_{ij} - \mathbf{k}_{fg}|}{2} \quad (\text{III.B.51})$$

Now from the law of cosines

$$(2q_{\parallel})^2 = k_{ij}^2 + k_{fg}^2 - 2k_{ij}k_{fg} \cos \theta \quad (\text{III.B.52})$$

Substituting k_{fg} from equation (III.B.50) into equation (III.B.52) gives

$$(2q_{\parallel})^2 = 2k_{ij}^2 + k_o^2 - 2k_{ij} \sqrt{k_{ij}^2 + k_o^2} \cos \theta \quad (\text{III.B.53})$$

Performing the dk_{fg} part of the $d^2k_{fg} = d\theta k_{fg} dk_{fg}$ integration and using equation (III.B.47) gets rid of the delta function and gives q_{\parallel} , which is a function of k_{fg} and θ . Thus, the $d\theta$ part of this integration remains.

$$\begin{aligned} W_{e^-e^-} &= \frac{1}{4} \frac{me^4}{16\pi^3 \hbar^3 \epsilon^2} \int d^2k_{fg} d^2k_j \left| \frac{A_{ifg}(q_{\parallel})}{q_{\parallel}} \right|^2 F_{ifg} \delta \left(k_f^2 + k_g^2 - k_i^2 - k_j^2 + \frac{2m}{\hbar^2}(E_f + E_g - E_i - E_j) \right) \\ &= \frac{me^4}{64\pi^3 \hbar^3 \epsilon^2} \int d\theta d^2k_j \left| \frac{A_{ifg}(q_{\parallel})}{q_{\parallel}} \right|^2 F_{ifg} \end{aligned} \quad (\text{III.B.54})$$

Now $d^2k_j = d\alpha_1 k_j dk_j$, where α_1 is the angle between \mathbf{k}_i and \mathbf{k}_j (the integral is performed along k_{ij} with angle α_1).

$$W_{e^-e^-} = \frac{me^4}{64\pi^3 \hbar^3 \epsilon^2} \int d\theta d\alpha_1 k_j dk_j \left| \frac{A_{ifg}(q_{\parallel})}{q_{\parallel}} \right|^2 F_{ifg} \quad (\text{III.B.55})$$

The upper limit of integration for k_j can be taken to be the top of the well barrier.

$$k_{j \max} = \sqrt{\frac{2m}{\hbar^2}(V_{\text{barrier}} - E_j)} \quad (\text{III.B.56})$$

Equation (III.B.55) is an expression for calculating the electron-electron scattering rate.

2. Screening

The formulation so far has assumed that there are only the two initial electrons and they scatter due to the Coulomb force between them. That is, it has been assumed

that there are no other electrons (free carriers) present. In reality, there will be carrier concentrations in the subbands. These free carriers respond under the influence of the electrostatic field. This will have the effect of reducing the force between the initial electrons and reduce the scattering rate due to this screening.

One screening model, is the static single subband screening model, where the dielectric function is modified to take the screening into account. This was first derived by the given reference⁸⁵ and later used by others.⁸⁶ This model can be included by taking ε inside the scattering integral, and replacing it with $\varepsilon = \varepsilon\varepsilon_{sc}$, where

$$\varepsilon_{sc} = 1 + \frac{e^2}{2\varepsilon} \frac{1}{q_{\parallel}} \Pi_{ii}(q_{\parallel}) A_{iii}(q_{\parallel}) \quad (\text{III.B.57})$$

and the polarization factor ignoring collision broadening at $T = 0$ K is

$$\Pi_{ii}(q_{\parallel}, T = 0 \text{ K}) = \frac{m}{\pi\hbar^2} \left[1 - U(q_{\parallel} - 2K_F) \sqrt{1 - \left(\frac{2K_F}{q_{\parallel}} \right)^2} \right] \quad (\text{III.B.58})$$

where $U(q_{\parallel} - 2K_F)$ is a unit step function that when $q_{\parallel} > 2K_F$ is equal to 1, and otherwise 0. At any temperature T , under the assumption of noninteracting polarizability, the polarization factor becomes⁸⁷

$$\begin{aligned} \Pi_{ii}(q_{\parallel}, T) &= \int_0^{\infty} dE \frac{\Pi_{ii}(q_{\parallel}, T = 0 \text{ K})}{4k_B T \cosh^2\left(\frac{E_F - E}{2k_B T}\right)} \\ &= \Pi_{ii}(q_{\parallel}, T = 0 \text{ K}) \frac{1}{2} \left[1 + \tanh\left(\frac{E_F}{2k_B T}\right) \right] \end{aligned} \quad (\text{III.B.59})$$

where k_B is Boltzman's constant and K_F is the Fermi wave vector defined as

$$K_F = \sqrt{\frac{2\pi n_i}{g}} \quad (\text{III.B.60})$$

with the valley degeneracy factor $g = 1$ for GaAs, which gives the number of equivalent energy bands.

As an example of how screening affects electron-electron scattering, consider the 1100 scattering process for an infinite GaAs well 40 nm in length (Figure III.B.3). The rates are calculated for subband populations of 1×10^{10} and $1 \times 10^{12} \text{ cm}^{-2}$ at $T = 300$ K,

unscreened and including screening. As expected, the scattering rate increases as the subband population increases. The screening effect becomes significant for large sheet densities. Sheet densities on the order of 10^{12} cm^{-2} are two orders of magnitude larger than typically used in QCLs.

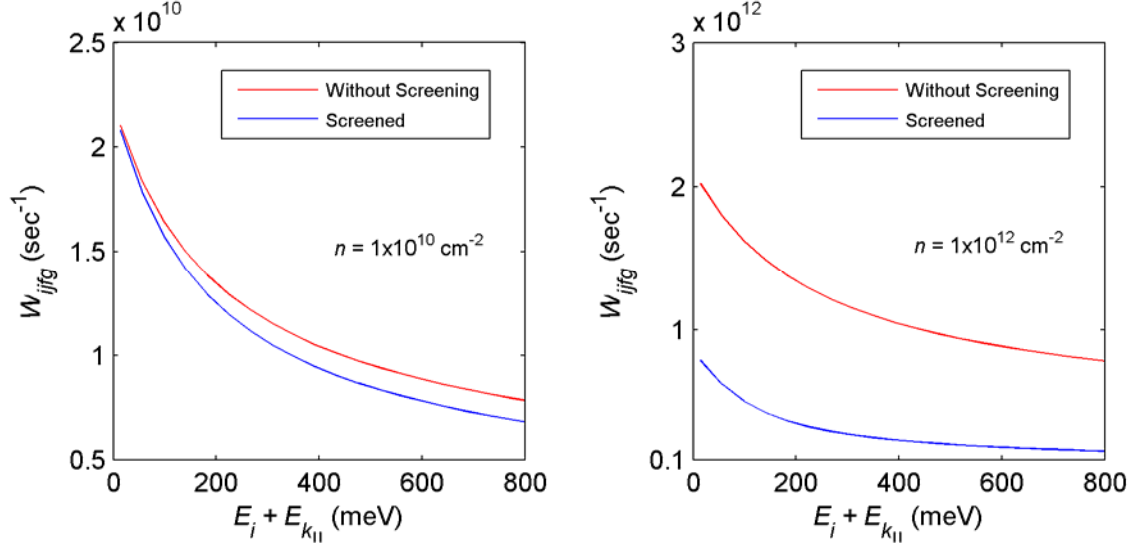


Figure III.B.3. Electron-electron scattering rate as a function of total energy at $T = 300 \text{ K}$, with and without including screening, for subband populations of (a) 1×10^{10} and (b) $1 \times 10^{12} \text{ cm}^{-2}$.

3. Mean Scattering Rate

The electron-electron scattering rate calculated so far, is for the i indexed electron at a given energy averaged over the j indexed electron initial state distribution. Since there is a distribution of carriers in the initial state, the mean scattering rate averaged over the Fermi-Dirac distribution of carriers in the initial state can be found as follows

$$W_{e^-e^-, \text{mean}} = \frac{\int dE_{k_i} W_{e^-e^-, i} f_{FD, i}(k_i)}{\int dE_{k_i} f_{FD, i}(k_i)} = \frac{m}{\pi \hbar^2 n_i} \int dE_{k_i} W_{e^-e^-, i} f_{FD, i}(k_i) \quad (\text{III.B.61})$$

since

$$n_i = \int dE_{k_i} f_{FD, i}(k_i) \frac{m}{\pi \hbar^2} \quad (\text{III.B.62})$$

4. Antiparallel and Parallel Spins

In this section, taking into account spin and state blocking will be discussed. Starting with equation (III.B.33), the solution can be found by defining angles between the momentum vectors different than what was used earlier.⁸⁸ Including screening, the equation can be written as

$$W_{e^-e^-} = \frac{e^4}{32\pi^3\hbar\epsilon^2} \int d^2k_f d^2k_g d^2k_j \left| \frac{A_{ifg}(q_{\parallel})}{q_{\parallel}\epsilon_{sc}} \right|^2 [1 - f_{FD,f}(k_f)] [1 - f_{FD,g}(k_g)] f_{FD,j}(k_j) \quad (\text{III.B.63})$$

$$\times \delta(\mathbf{k}_f + \mathbf{k}_g - \mathbf{k}_i - \mathbf{k}_j) \delta(E_{Tf} + E_{Tg} - E_{Ti} - E_{Tj})$$

Integrating over the d^2k_g to get rid of the momentum delta function and using $d^2k_j = d\alpha_1 k_j dk_j$, the equation becomes

$$W_{e^-e^-} = \frac{e^4}{32\pi^3\hbar\epsilon^2} \int d^2k_f d\alpha_1 k_j dk_j \left| \frac{A_{ifg}(q_{\parallel})}{q_{\parallel}\epsilon_{sc}} \right|^2 [1 - f_{FD,f}(k_f)] [1 - f_{FD,g}(k_g)] f_{FD,j}(k_j) \quad (\text{III.B.64})$$

$$\times \delta(E_{Tf} + E_{Tg} - E_{Ti} - E_{Tj})$$

From the usual conservation of energy and momentum we have the following

$$E_f + \frac{\hbar^2 k_f^2}{2m} + E_g + \frac{\hbar^2 k_g^2}{2m} = E_i + \frac{\hbar^2 k_i^2}{2m} + E_j + \frac{\hbar^2 k_j^2}{2m} \quad (\text{III.B.65})$$

$$\mathbf{k}_g = \mathbf{k}_i + \mathbf{k}_j - \mathbf{k}_f \quad (\text{III.B.66})$$

Now defining the angles for the momentum vectors as follows (Figure III.B.4)

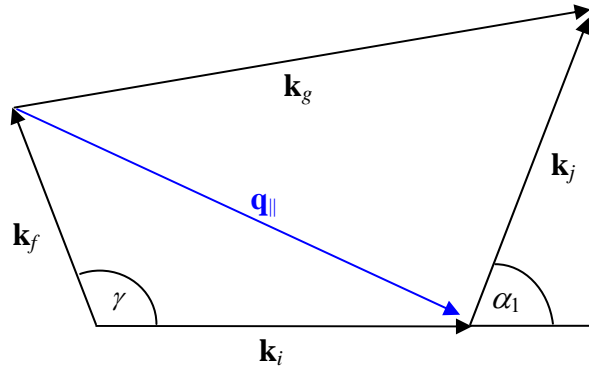


Figure III.B.4. Momentum vectors used in the calculation of the electron-electron scattering rate, for the case when state blocking is included.

k_g^2 can be solved for by squaring the conservation of momentum equation

$$\begin{aligned}
k_g^2 &= (\mathbf{k}_i + \mathbf{k}_j - \mathbf{k}_f) \cdot (\mathbf{k}_i + \mathbf{k}_j - \mathbf{k}_f) \\
&= k_i^2 + k_j^2 + k_f^2 - 2k_i k_f \cos(\gamma) + 2k_i k_j \cos(\alpha_1) - 2k_j k_f \cos(\gamma - \alpha_1)
\end{aligned} \tag{III.B.67}$$

Substituting equation (III.B.67) into equation (III.B.65)

$$\begin{aligned}
E_i + \frac{\hbar^2 k_i^2}{2m} + E_j + \frac{\hbar^2 k_j^2}{2m} &= E_f + \frac{\hbar^2 k_f^2}{2m} + E_g + \frac{\hbar^2}{2m} \\
&\times [k_i^2 + k_j^2 + k_f^2 - 2k_i k_f \cos(\gamma) + 2k_i k_j \cos(\alpha_1) - 2k_j k_f \cos(\gamma - \alpha_1)]
\end{aligned} \tag{III.B.68}$$

The resulting quadratic can be solved to find k_f

$$k_f = \frac{1}{2} k_i \cos(\gamma) + \frac{1}{2} k_j \cos(\alpha_1 - \gamma) \pm \frac{1}{2} \left\{ \left[[k_i \cos(\gamma) + k_j \cos(\alpha_1 - \gamma)]^2 - 4k_i k_j \cos(\alpha_1) \right]^{\frac{1}{2}} + \left[\frac{4m}{\hbar^2} (E_i + E_j - E_f - E_g) \right] \right\} \tag{III.B.69}$$

From Figure III.B.4 the following equations for k_g and q_{\parallel}^2 are found, where angle γ is the angle between \mathbf{k}_i and \mathbf{k}_f

$$k_g = \left[(k_i + k_j \cos(\alpha_1) - k_f \cos(\gamma))^2 + (k_j \sin(\alpha_1) - k_f \sin(\gamma))^2 \right]^{\frac{1}{2}} \tag{III.B.70}$$

$$q_{\parallel}^2 = k_i^2 + k_f^2 - 2k_i k_f \cos(\gamma) \tag{III.B.71}$$

These equations are in a form so that state blocking can be included. Now to take into account spin, consider the case where the electrons have equal probability of having parallel and antiparallel spins. Including the exchange effect discussed earlier, it is seen that the following substitutions must be made to equation (III.B.64)

$$\left| \frac{A_{ijfg}(q_{\parallel})}{q_{\parallel} \varepsilon_{sc}(q_{\parallel})} \right|^2 \rightarrow \frac{1}{2} \left[\left| \frac{A_{ijfg}(q_{\parallel})}{q_{\parallel} \varepsilon_{sc}(q_{\parallel})} \right|^2 + \left| \frac{A_{ijgf}(q'_{\parallel})}{q'_{\parallel} \varepsilon_{sc}(q'_{\parallel})} \right|^2 - \frac{A_{ijfg}(q_{\parallel}) A_{ijgf}^*(q'_{\parallel})}{q_{\parallel} q'_{\parallel} \varepsilon_{sc}(q_{\parallel}) \varepsilon_{sc}(q'_{\parallel})} \right] \tag{III.B.72}$$

where

$$q'_{\parallel}^2 = k_j^2 + k_f^2 - 2k_j k_f \cos(\alpha_1 - \gamma) \tag{III.B.73}$$

and angle $\gamma - \alpha_1$ is between \mathbf{k}_f and \mathbf{k}_j . This agrees with that in the given reference.⁸⁸

C. IMPURITY SCATTERING AND INTERFACE ROUGHNESS SCATTERING

In this section, two additional scattering mechanisms, impurity scattering and interface roughness scattering, will be discussed. Beginning with impurity scattering,

ionized impurities within a semiconductor lattice and its distributed charges, can cause scattering due to the Coulombic interaction. The corresponding matrix element may be written as

$$\begin{aligned}\langle f|V|i\rangle &= \langle f|\frac{\alpha}{\epsilon|\mathbf{x}-\mathbf{x}'|}|i\rangle \\ &= \frac{\alpha}{\epsilon A^2} \int d^2x_{\parallel} d^2x'_{\parallel} dx_3 \psi_f^*(x_3) \psi_i(x_3) \frac{e^{i(\mathbf{k}_i-\mathbf{k}_f)\cdot\mathbf{x}_{\parallel}}}{|\mathbf{x}-\mathbf{x}'|}\end{aligned}\quad (\text{III.C.1})$$

This matrix element can be simplified for scattering from an ionized impurity at $x_3 = x'_3$, in a similar manner as was done with the electron-electron scattering case, inserting \hbar and c back into the equation this becomes

$$\begin{aligned}\langle f|V|i\rangle &= \frac{e^2}{2\epsilon A q_{\parallel}} \int dx_3 \psi_f^*(x_3) \psi_i(x_3) e^{-q_{\parallel}|x_3-x'_3|} \\ &= \frac{e^2}{2\epsilon A q_{\parallel}} \frac{A_{if}(q_{\parallel})}{q_{\parallel}}\end{aligned}\quad (\text{III.C.2})$$

where

$$A_{if}(q_{\parallel}) = \int dx_3 \psi_f^*(x_3) \psi_i(x_3) e^{-q_{\parallel}|x_3-x'_3|} \quad (\text{III.C.3})$$

and $q_{\parallel} = \Delta k = |\mathbf{k}_i - \mathbf{k}_f| = k_i^2 + k_f^2 - 2k_i k_f \cos\theta$. The scattering rate can be found by substituting the above matrix element into Fermi's golden rule, summing over the final states

$$\begin{aligned}W_{\text{impurity}} &= \frac{2\pi}{\hbar} \sum_f |\langle f|V|i\rangle|^2 \delta\left[E_f + \frac{\hbar^2 k_f^2}{2m} - \left(E_i + \frac{\hbar^2 k_i^2}{2m}\right)\right] \\ &= \frac{2\pi}{\hbar} \left(\frac{e^2}{2\epsilon A}\right)^2 \sum_f \left|\frac{A_{if}(q_{\parallel})}{q_{\parallel}}\right|^2 \delta(E_{Tf} - E_{Ti})\end{aligned}\quad (\text{III.C.4})$$

where E_T is total energy, i.e., the subband edge plus the in-plane kinetic energy. Converting the final states summation to an integral in k-space, this becomes

$$\begin{aligned}
W_{\text{impurity}} &= \frac{2\pi e^4}{\hbar 4\epsilon^2 A^2} \frac{A}{(2\pi)^2} \int d^2 k_f \left| \frac{A_{if}(q_{\parallel})}{q_{\parallel}} \right|^2 \delta(E_{T,f} - E_{T,i}) \\
&= \frac{e^4}{8\pi\hbar\epsilon^2 A} \int d^2 k_f \left| \frac{A_{if}(q_{\parallel})}{q_{\parallel}} \right|^2 \delta(E_{T,f} - E_{T,i}) \\
&= \frac{me^4}{4\pi\hbar^3\epsilon^2 A} \int d^2 k_f \left| \frac{A_{if}(q_{\parallel})}{q_{\parallel}} \right|^2 \delta \left[k_f^2 - k_i^2 + \frac{2m}{\hbar^2} (E_f - E_i) \right]
\end{aligned} \tag{III.C.5}$$

Performing the dk_f part of the $d^2k_f = d\theta k_f dk_f$ integration gets rid of the delta function and the following is found

$$W_{\text{impurity}} = \frac{me^4}{8\pi\hbar^3\epsilon^2 A} \int d\theta \left| \frac{A_{if}(q_{\parallel})}{q_{\parallel}} \right|^2 \tag{III.C.6}$$

To apply this for the case of doping over a distribution, where a sheet charge is $dx_3 n_{3D}(x_3)$ at $x_3 = x_3'$, the final expression for computing scattering due to ionized impurities becomes

$$W_{\text{impurity}} = \frac{me^4}{8\pi\hbar^3\epsilon^2} \int dx_3' n_{3D}(x_3') \int d\theta \left| \frac{A_{if}(q_{\parallel})}{q_{\parallel}} \right|^2 \tag{III.C.7}$$

Monolayer fluctuations are often formed at heterostructure interfaces. Scattering can occur from these imperfect growth surfaces, where these variations in the barrier thicknesses gives way to variations in the energy levels and wavefunctions of the subbands. Assuming that the roughness height $\Delta(\mathbf{x})$ at the in-plane position has a correlation function of ⁸⁹⁻⁹²

$$\langle \Delta(\mathbf{x}_{\parallel}) \Delta(\mathbf{x}'_{\parallel}) \rangle = \frac{\pi \Delta^2 \Lambda^2}{A} \left(1 + \frac{q^2 \Lambda^2}{2} \right)^{-3/2} \tag{III.C.8}$$

where the Δ is the roughness and Λ is the correlation length, the matrix element is given by

$$\langle f | V | i \rangle = \int d^2 x_{\parallel} F_{mn} \Delta(\mathbf{x}_{\parallel}) e^{iq \cdot \mathbf{x}_{\parallel}} \tag{III.C.9}$$

with

$$F_{mn} = V_o \psi_f(x_o) \psi_i(x_o) \tag{III.C.10}$$

Substituting the matrix element into Fermi's golden rule and summing over the final states we find

$$\begin{aligned}
W_{\text{interface roughness}} &= \frac{2\pi}{\hbar} \sum_f \left| \langle f | V | i \rangle \right|^2 \delta(E_{T,f} - E_{T,i}) \\
&= \frac{2\pi}{\hbar} \left| V_o \psi_f^*(x_o) \psi_i(x_o) \right|^2 \frac{1}{A} \sum_f \pi \Delta^2 \Lambda^2 \left(1 + \frac{q^2 \Lambda^2}{2} \right)^{-3/2} \delta(E_{T,f} - E_{T,i}) \\
&= \frac{2\pi^2 \Delta^2 \Lambda^2}{\hbar} \left| V_o \psi_f^*(x_o) \psi_i(x_o) \right|^2 \frac{1}{A} \frac{A}{(2\pi)^2} \int d^2 k_f \left(1 + \frac{q^2 \Lambda^2}{2} \right)^{-3/2} \delta \left[E_f + \frac{\hbar^2 k_f^2}{2m} - \left(E_i + \frac{\hbar^2 k_i^2}{2m} \right) \right] \\
&= \frac{\Delta^2 \Lambda^2}{2\hbar} \left| V_o \psi_f^*(x_o) \psi_i(x_o) \right|^2 \frac{2m}{\hbar^2} \int d\theta k_f dk_f \left(1 + \frac{q^2 \Lambda^2}{2} \right)^{-3/2} \delta \left(k_f^2 - k_i^2 + \frac{2m}{\hbar^2} (E_f - E_i) \right)
\end{aligned} \tag{III.C.11}$$

Performing the dk_f part of the $d^2 k_f = d\theta k_f dk_f$ integration gets rid of the delta function and the following is arrived at (noting the parallel subscript has been dropped)

$$W_{\text{interface roughness}} = \frac{m \Delta^2 \Lambda^2}{2\hbar^3} \left| V_o \psi_f^*(x_o) \psi_i(x_o) \right|^2 \int d\theta \left(1 + \frac{q^2 \Lambda^2}{2} \right)^{-3/2} \tag{III.C.12}$$

This is the scattering rate due to interface roughness using an exponential autocovariance function. A roughness $a/2$, where a is the lattice parameter, with a correlation length of 5 nm was used in some of the simulations that will be discussed later.

1. Mean Scattering Rate

Because there is a distribution of carrier energies in the initial state, the mean scattering rate is again calculated by averaging over the Fermi-Dirac distribution of carriers in the initial state.

$$W_{\left\{ \begin{smallmatrix} \text{impurity,} \\ \text{interface roughness} \end{smallmatrix} \right\}, \text{mean}} = \frac{\int dE_{k_i} W_{\left\{ \begin{smallmatrix} \text{impurity,} \\ \text{interface roughness} \end{smallmatrix} \right\}, i} f_{FD,i}(k_i) [1 - f_{FD,f}(k_f)]}{\int dE_{k_i} f_{FD,i}(k_i)} \tag{III.C.13}$$

D. RADIATIVE TRANSITION

The optical transition occurs when an electron releases a photon and transitions from the upper to lower lasing state. As will be shown, spontaneous emission lifetimes are on the order of microseconds, while other rates previously discussed such as phonon rates can have lifetimes on the order of picoseconds. Thus, state lifetimes are not determined from spontaneous emission rates. This section will discuss the optical

transition and the very important parameter the gain. It will conclude by discussing some fundamental parameters found by approximate rate equation analysis.

The potential for the radiative transition can be found by starting with the nonrelativistic electromagnetic Lagrangian,⁸² and then finding the Hamiltonian in the usual way $H = \sum p_i \dot{q}_i - L_{EM}$.

$$H = \frac{1}{2m} (\mathbf{p}^2 - 2q_c \mathbf{A} \cdot \mathbf{p} + q_c^2 \mathbf{A}^2) + q_c \Phi \approx \frac{\mathbf{p}^2}{2m} + q_c \Phi - \frac{q_c}{m} \mathbf{A} \cdot \mathbf{p} \quad (\text{III.D.1})$$

The Hamiltonian is now in the form of $H = H_0 + V$. Substituting for the electron charge, $q_c = -|e|$, the interaction is given by⁷⁹

$$V_{\text{radiative}} = \frac{e}{m} \mathbf{A} \cdot \mathbf{p} \quad (\text{III.D.2})$$

The equations for the \mathbf{E} and \mathbf{B} fields in terms of the scalar and vector potentials (Φ and \mathbf{A}) can be written as a second rank antisymmetric field strength tensor $F^{\mu\nu} = \partial^\mu A^\nu - \partial^\nu A^\mu$.⁸² These equations automatically satisfy Maxwell's homogeneous equations, and the inhomogeneous equations are $\partial_\mu F^{\mu\nu} = J^\nu$. The scalar and vector potentials are not uniquely determined because the following change $A_\mu \rightarrow A_\mu + \partial_\mu \Lambda(\mathbf{x}, t)$ has no effect on the fields \mathbf{E} and \mathbf{B} since $\partial^\mu A^\nu - \partial^\nu A^\mu = \partial^\mu A^\nu - \partial^\nu A^\mu$. Therefore, one such gauge transformation we are free to choose is the Lorentz gauge $\partial_\mu A^\mu = 0$, which Maxwell's equations simplify to one equation $\square A^\mu = J^\mu$. Without sources $J = 0$, and the equation for the vector potential becomes

$$\nabla^2 \mathbf{A} - \frac{\partial^2 \mathbf{A}}{\partial t^2} = 0 \quad (\text{III.D.3})$$

which has a solution of

$$\mathbf{A} = A_0 \cos(\mathbf{q} \cdot \mathbf{x} - \omega t) \hat{\mathbf{e}} = \frac{A_0}{2} [e^{i(\mathbf{q} \cdot \mathbf{x} - \omega t)} + e^{-i(\mathbf{q} \cdot \mathbf{x} - \omega t)}] \hat{\mathbf{e}} \quad (\text{III.D.4})$$

Since Φ is included in H_0 , \mathbf{E} and \mathbf{H} are solved effectively with $\Phi = 0$.

$$\mathbf{E} = -\frac{\partial \mathbf{A}}{\partial t} = -\omega A_0 \sin(\mathbf{q} \cdot \mathbf{x} - \omega t) \hat{\mathbf{e}} \quad (\text{III.D.5})$$

$$\mathbf{H} = \frac{1}{\mu} \nabla \times \mathbf{A} = -\frac{A_0}{\mu} \sin(\mathbf{q} \cdot \mathbf{x} - \omega t) \mathbf{q} \times \hat{\mathbf{e}} \quad (\text{III.D.6})$$

The Poynting vector can now be found from these fields

$$\mathbf{S} = \mathbf{E} \times \mathbf{H} = \frac{\omega A_0^2}{\mu} \sin^2(\mathbf{q} \cdot \mathbf{x} - \omega t) \mathbf{q} \quad (\text{III.D.7})$$

and the average Poynting vector is (noting $\omega = \mathbf{v} \cdot \mathbf{q}$)

$$\langle \mathbf{S} \rangle = \frac{1}{2} \frac{\omega A_0^2}{\mu} \mathbf{q} = \frac{A_0^2 q^2}{2\mu} \mathbf{v} \quad (\text{III.D.8})$$

Inserting \hbar and c back into the equations, the average energy density found from equation (II.D.8) is equal to $N\hbar\omega/V$, where V is the volume

$$\langle E_v \rangle = \frac{\langle \mathbf{S} \rangle}{\mathbf{v}} = \frac{A_0^2 q^2}{2\mu} = \frac{N\hbar\omega}{V} \quad (\text{III.D.9})$$

from which A_0^2 can be solved for

$$A_0^2 = \frac{2\hbar N}{V \epsilon \omega} \quad (\text{III.D.10})$$

Substituting this into equation (III.D.4), the vector potential becomes

$$\mathbf{A} = \frac{1}{2} \sqrt{\frac{2\hbar N}{V \epsilon \omega}} \left[e^{i(\mathbf{q} \cdot \mathbf{x} - \omega t)} + e^{-i(\mathbf{q} \cdot \mathbf{x} - \omega t)} \right] \hat{\mathbf{e}} \quad (\text{III.D.11})$$

This can now be substituted into equation (III.D.2), the expression for the radiative potential. This is valid for absorption, and the following change $N \rightarrow N+1$ must be made for the emission case, to account for spontaneous and stimulated emission. In terms of ladder operators, the interaction potential for the radiative transition becomes (dropping the harmonic part and promoting the momentum term to the quantum mechanical operator)

$$V_{\text{radiative}} = \frac{e}{m} \sqrt{\frac{\hbar}{2V \epsilon \omega}} \left[a_{\mathbf{q}} e^{i\mathbf{q} \cdot \mathbf{x}} + a_{\mathbf{q}}^\dagger e^{-i\mathbf{q} \cdot \mathbf{x}} \right] \hat{\mathbf{e}} \cdot \mathbf{p} = \frac{e}{m} \sqrt{\frac{\hbar}{2V \epsilon \omega}} \left[a_{\mathbf{q}} + a_{-\mathbf{q}}^\dagger \right] e^{i\mathbf{q} \cdot \mathbf{x}} \hat{\mathbf{e}} \cdot \mathbf{p} \quad (\text{III.D.12})$$

1. Emission Rate

To find the 2D spontaneous emission rate, equation (III.D.12) is substituted into Fermi's golden rule keeping the emission term.

$$\begin{aligned} W_{\text{radiative},e} &= \frac{2\pi}{\hbar} \sum_f \left| \langle f | V_{\text{radiative}} | i \rangle \right|^2 \delta(E_f - E_i - \hbar\omega) \\ &= \frac{\pi e^2}{\epsilon V m^2 \omega} \sum_f \left| \langle f | a_{\mathbf{q}}^\dagger e^{-i\mathbf{q} \cdot \mathbf{x}} \hat{\mathbf{e}} \cdot \mathbf{p} | i \rangle \right|^2 \delta(E_f - E_i - \hbar\omega) \end{aligned} \quad (\text{III.D.13})$$

Using the electric dipole approximation, $e^{-i\mathbf{q}\cdot\mathbf{x}} \sim 1$

$$W_{\text{radiative},e} = \frac{\pi e^2}{\epsilon \mathcal{V} m^2 \omega} (N+1) \sum_f |\hat{\mathbf{e}} \cdot \langle f | \mathbf{p} | i \rangle|^2 \delta(E_f - E_i - \hbar\omega) \quad (\text{III.D.14})$$

Setting $N \sim 0$ which is permissible for low intensity light, that is spontaneous emission occurs without any photons in the cavity (to stimulate emission)

$$W_{\text{spont}} = \frac{\pi e^2}{\epsilon \mathcal{V} m^2 \omega} \sum_f |\hat{\mathbf{e}} \cdot \langle f | \mathbf{p} | i \rangle|^2 \delta(E_f - E_i - \hbar\omega) \quad (\text{III.D.15})$$

Summing over the polarizations and final states (including all final photon states for spontaneous emission into all modes), and converting the k-space summation into an integral

$$W_{\text{spont}} = \frac{\pi e^2}{\epsilon \mathcal{V} m^2 \omega} \frac{A}{(2\pi)^2 \hbar^2} \sum_{\text{pol}} \int d^2 p |\hat{\mathbf{e}} \cdot \langle f | \mathbf{p} | i \rangle|^2 \delta(E_f - E_i - \hbar\omega) \quad (\text{III.D.16})$$

Note that $d^2 p = d\phi' p dp = d\phi' \hbar \omega / v^2 d(\hbar\omega)$

$$\begin{aligned} W_{\text{spont}} &= \frac{e^2 A}{4\epsilon \mathcal{V} m^2 \pi v^2 \hbar} \sum_{\text{pol}} \int d\phi' d(\hbar\omega) |\hat{\mathbf{e}} \cdot \langle f | \mathbf{p} | i \rangle|^2 \delta(E_f - E_i - \hbar\omega) \\ &= \frac{e^2}{4\epsilon \mathcal{L}_3 m^2 \pi v^2 \hbar} \sum_{\text{pol}} \int d\phi' |\hat{\mathbf{e}} \cdot \langle f | \mathbf{p} | i \rangle|^2 \end{aligned} \quad (\text{III.D.17})$$

To simplify the bracket, for the moment we switch to the Heisenberg picture, where the operators $\phi(x) = \phi(\mathbf{x}, t) = e^{iHt} \phi(\mathbf{x}) e^{-iHt}$ and $d\mathbf{x}/dt = 1/(i\hbar)[\mathbf{x}, H] = \mathbf{p}/m$.⁷⁸ Substituting this commutator into the bracket

$$\langle f | \mathbf{p} | i \rangle = i \frac{m}{\hbar} \langle f | [H, \mathbf{x}] | i \rangle \quad (\text{III.D.18})$$

Noting that the momentum operator is a constant of motion, i.e., $p(t) = p(0)$, switching back to the Schrödinger picture we find

$$\langle f | \mathbf{p} | i \rangle = i \frac{m}{\hbar} \langle f | H\mathbf{x} - \mathbf{x}H | i \rangle = i \frac{m}{\hbar} (E_f - E_i) \langle f | \mathbf{x} | i \rangle \quad (\text{III.D.19})$$

and defining $\omega = (E_i - E_f)/\hbar$ (which will give a minus sign)

$$\langle f | \mathbf{p} | i \rangle = -im\omega \langle f | \mathbf{x} | i \rangle \quad (\text{III.D.20})$$

Substituting this into equation (III.D.17) and evaluating the summation for the 2D case, noting the polarization sum does not affect anything for the 2D case since the integration is only in terms of $d\phi'$ (i.e., not $d\theta$)

$$\begin{aligned}
 W_{spont} &= \frac{e^2}{4\epsilon L_3 m^2 \pi v^2 \hbar} m^2 \omega^2 \sum_{pol} \int d\phi' |\hat{\mathbf{e}} \cdot \langle f | \mathbf{x} | i \rangle|^2 \\
 &= \frac{e^2 \omega^2}{4\epsilon L_3 \pi v^2 \hbar} 2\pi |\hat{\mathbf{e}} \cdot \langle f | \mathbf{x} | i \rangle|^2
 \end{aligned} \tag{III.D.21}$$

The final expression for the spontaneous emission into all modes becomes (noting envelope wavefunctions are assumed)

$$W_{spont} = \frac{e^2 \omega^2}{2\epsilon L_3 v^2 \hbar} |\langle f | x | i \rangle|^2 \tag{III.D.22}$$

The 3D emission rate can be found in a similar method as for the 2D case, except when performing the polarization sum for the 3D case the square of the bracket term reduces to $|\langle f | x | i \rangle|^2 \sin^2 \theta$

$$W_{3D\,spont} = \frac{e^2 \omega^3}{3\pi \epsilon v^3 \hbar} |\langle f | x | i \rangle|^2 \tag{III.D.23}$$

As can be seen, there is a difference between the 2D and 3D emission cases (noting both are single electron scattering rates). A quick computation reveals spontaneous emission rates are on the order of microseconds, and thus as previously mentioned, do not affect state lifetimes.

2. Gain

The net transitions from the upper to lower lasing state, lead to an induced power $= \hbar \omega (N_2 W_{21} - N_1 W_{12}) = \hbar \omega (\Delta N \times W_{21})$, where $W_{21} = W_{12}$ are the stimulated emission and absorption rates respectively. This amplifies the propagating electromagnetic waves intensity as $dI/dx = gain \times I$. The optical gain of the medium can be found, starting with equation (III.D.14) by keeping the stimulated emission term. Defining the photon flux I_{photon} as the number of photons per unit area and time, substituting for the momentum operator and noting $I_{photon}/v = (\text{Number of photons})/V$ (where v is the speed of light in the medium and V is the volume), the stimulated emission rate (a positive quantity) assuming single mode becomes

$$W_{stim} = \frac{\pi e^2 \hbar^2}{m^2 \varepsilon \omega} \frac{I_{photon}}{v} \left| \langle f | \frac{d}{dx} | i \rangle \right|^2 \delta(E_f - E_i - \hbar \omega) \quad (\text{III.D.24})$$

The gain is defined as (number of transitions per unit volume and time)/(emitted photon flux) = $W/LA/I_{photon} = W/LAI_{photon}$. Noting that the population inversion is $\Delta n_{3D} LA$ number of electrons, the expression for gain becomes

$$\begin{aligned} gain &= \frac{\pi e^2 \hbar^2}{m^2 \varepsilon v \omega} \frac{I_{photon}}{LAI_{photon}} \Delta n_{3D} LA \left| \langle f | \frac{d}{dx} | i \rangle \right|^2 \delta(E_f - E_i - \hbar \omega) \\ &= \frac{\pi e^2 \hbar^2}{m^2 \varepsilon v \omega} \Delta n_{3D} \left| \langle f | \frac{d}{dx} | i \rangle \right|^2 \delta(E_f - E_i - \hbar \omega) \end{aligned} \quad (\text{III.D.25})$$

Taking into account a finite line width, the delta function can be replaced with the Lorentzian⁹³

$$\mathcal{L}(\hbar \omega) = \frac{1}{\pi} \frac{FWHM / 2}{(\Delta E - \hbar \omega)^2 + (FWHM / 2)^2} \quad (\text{III.D.26})$$

where $FWHM$ is the full width half maximum. The maximum gain occurs when $\Delta E = \hbar \omega$, and the Lorentzian is then equal to $2/(\pi FWHM)$. Substituting this in place of the delta function, the expression for peak gain becomes

$$peak\ gain = \frac{2e^2 \hbar^2 \Delta n_{3D}}{m^2 \varepsilon v \omega FWHM} \left| \langle f | \frac{d}{dx} | i \rangle \right|^2 = \frac{2e^2 \hbar \Delta n_{3D}}{m \varepsilon v FWHM} \left| \langle f | x | i \rangle \right|^2 \quad (\text{III.D.27})$$

In Heaviside-Lorentz units $\varepsilon v = n_{index} c$ (while in rationalized mksA units $\varepsilon v = \varepsilon_0 n_{index} c$). This expression can be used for estimating the threshold population inversion, when the threshold gain is found from the waveguide resonator analysis. While having a large oscillator strength = $2\hbar/m\omega |\langle f | d/dx | i \rangle|^2 = 2m\omega/\hbar |\langle f | x | i \rangle|^2$ is favorable, so is having a long upper state lifetime to maintain the 3D population inversion Δn_{3D} , as can be seen from the equation for peak gain. These are often competing characteristics.

3. Rate Equations

As we have seen, scattering rates are density and temperature dependent. Even to compute the mean rates, requires knowing the densities and electron temperatures of the states, which can only be determined by analyzing the full structure. Thus, rate equations are not well suited for analyzing full structures. Nevertheless, some important fundamentals can be found from an approximate rate equation analysis. The rate

equations for a three level system, in terms of 3D volumetric densities, for the optical mode and state populations are

$$\frac{dn_{photon}}{dt} = \frac{(n_2 - n_1)\Gamma V n_{photon}}{\tau_{spon\ single\ mode}} + \frac{n_2\Gamma}{\tau_{spon\ all\ modes}} - \frac{n_{photon}}{\tau_{photon}} \quad (\text{III.D.28})$$

$$\frac{dn_2}{dt} = \eta \frac{J}{|e|L} - \frac{(n_2 - n_1)V n_{photon}}{\tau_{spon\ single\ mode}} - \frac{n_2}{\tau_{spon\ all\ modes}} - \frac{n_2}{\tau_2} \quad (\text{III.D.29})$$

$$\frac{dn_1}{dt} = (1 - \eta) \frac{J}{|e|L} + \frac{(n_2 - n_1)V n_{photon}}{\tau_{spon\ single\ mode}} + \frac{n_2}{\tau_{spon\ all\ modes}} + \frac{n_2}{\tau_2} - \frac{n_1}{\tau_1} \quad (\text{III.D.30})$$

where the upper and lower lasing states are indexed by 2 and 1 respectively. The notation used is n_{photon} is the 3D photon population mode density, $\tau_{spon\ single\ mode}$ is the spontaneous emission into the single lasing mode, $\tau_{spon\ all\ modes}$ is the spontaneous emission into all modes (noting $1/\tau_{spon\ all\ modes} = N_{modes} 1/\tau_{spon\ single\ mode}$ and the total stimulated emission rate $1/\tau_{stim} = V n_{photon} 1/\tau_{spon\ single\ mode}$), $\tau_{photon} = v(\alpha_m + \alpha_\omega)$ is the photon cavity lifetime, $\tau_m = v\alpha_m$ is the mirror escape time, N is the number of sections, $V = LA$ is the volume of one section, V_c is the effective volume of the cavity, $\Gamma = NV/V_c$ is the confinement factor, η is the injection efficiency, and $J = I/A$ is the 2D current density. At steady state with $\tau_2 \ll \tau_{spon\ all\ modes}$ (since $\tau_{21} \ll \tau_{spon\ all\ modes}$) these equations become

$$0 = \frac{(n_2 - n_1)\Gamma V n_{photon}}{\tau_{spon\ single\ mode}} + \frac{n_2\Gamma}{\tau_{spon\ all\ modes}} - \frac{n_{photon}}{\tau_{photon}} \quad (\text{III.D.31})$$

$$0 = \eta \frac{J}{|e|L} - \frac{(n_2 - n_1)V n_{photon}}{\tau_{spon\ single\ mode}} - \frac{n_2}{\tau_2} \quad (\text{III.D.32})$$

$$0 = (1 - \eta) \frac{J}{|e|L} + \frac{(n_2 - n_1)V n_{photon}}{\tau_{spon\ single\ mode}} + \frac{n_2}{\tau_2} - \frac{n_1}{\tau_1} \quad (\text{III.D.33})$$

Above threshold, lots of photons are present in the cavity and $V n_{photon}$ is large, and the second term on the right hand side of equation (III.D.31) can be ignored.

$$\frac{(n_2 - n_1)\Gamma V}{\tau_{spon\ single\ mode}} = \frac{1}{\tau_{photon}} \quad (\text{III.D.34})$$

From equations (III.D.32) and (III.D.33), the 3D population inversion $\Delta n_{3D} = (n_2 - n_1)$ can be found. Substituting this back into equation (III.D.34), the photon density is determined to be

$$n_{photon} = \frac{\tau_{photon} \Gamma \eta_i}{A|e|L} (I - I_{th}) \quad (III.D.35)$$

where the internal quantum efficiency is⁹⁴

$$\eta_i = \frac{\eta \tau_2 \left(1 - \frac{\tau_1}{\tau_{21}}\right) - (1 - \eta) \tau_1}{\tau_1 + \tau_2 \left(1 - \frac{\tau_1}{\tau_{21}}\right)} \quad (III.D.36)$$

and the threshold current satisfying equation (III.D.34) is

$$I_{th} = \frac{A|e|L \tau_{spon\ single\ mode}}{\tau_{photon} \Gamma V} \frac{1}{\eta \tau_2 \left(1 - \frac{\tau_1}{\tau_{21}}\right) - (1 - \eta) \tau_1} \quad (III.D.37)$$

The power emitted by the laser can be found from $P = \hbar \omega V_c n_{photon} / \tau_m$, substituting for n_{photon} , τ_m , and Γ

$$P = \eta_i \frac{\alpha_m}{\alpha_m + \alpha_w} N \frac{\hbar \omega}{|e|} (I - I_{th}) \quad (III.D.38)$$

The first three terms in equation (III.D.38) grouped together, is the differential quantum efficiency, which is the number of photons emitted per electron. The internal quantum efficiency (defined above at some biases) shows the output power is reduced by an imperfect (less than unity) injection efficiency η and a finite lower lasing state lifetime τ_1 .

Below threshold, stimulated emission can be ignored because there are few photons within the cavity, $V n_{photon} \approx 0$. Solving for n_2 from the equation (III.D.32) and for n_1 from the equation (III.D.33), a relation for the population inversion is found, noting that $n_2 = \eta (J/|e|L) \tau_2$. Writing this in terms of the 2D population inversion

$$\Delta n_{2D} = \eta \frac{J}{|e|} \tau_2 \left(1 - \frac{\tau_1}{\tau_{21}}\right) - (1 - \eta) \frac{J}{|e|} \tau_1 \quad (III.D.39)$$

This equation allows for estimation of the threshold current. This simply shows it is necessary to have $\tau_1 < \tau_{21}$ for a population inversion, that it is desirable to have a perfect injection efficiency $\eta = 1$ and a long upper state lifetime. Improving any of these parameters would serve to improve the population inversion. Because rate equations are not well suited for analyzing the electron transport in QC structures, in the next section, it will be discussed how Monte Carlo simulations can be used to model these structures.

IV. MONTE CARLO SIMULATION

Since the lifetimes of the electronic states within QC structures are not constant, rate equations are not well suited for analyzing complete structures because they would be nonlinear. Thus, one approach that is more suited for this type of transport analysis is that based on Monte Carlo simulations. This approach does not rely on any assumptions about the electron distributions and can handle density and temperature dependent scattering mechanisms. By analyzing the complete structure, subband populations and electron distributions for all energy states can be determined. Quantities such as current density (which is measurable) and other quantities such as gain can be found. This is important because while having a large oscillator strength is favorable, so is having a long upper state lifetime to maintain the 3D population inversion Δn_{3D} , as can be seen from the equation for peak gain = $2e^2\hbar^2\Delta n_{3D}/m^2\varepsilon v\omega FWHM|\langle f|d/dx|i\rangle|^2$ (equation (III.D.27)). These are often competing characteristics.

A. ELECTRON TRANSPORT IN QC STRUCTURES

As has been discussed, the electron transport in entire QC structures is not suited for rate equation analysis, and the large number of scattering rates that must be computed would further complicate attempting to use such an approach. From the transport analysis of QC structures, we ultimately seek to find the populations and electron distributions of all states in the structure. The time evolution of the electron distribution functions is described by

$$\frac{df_{\mathbf{k}\beta}}{dt} = \sum_{\mathbf{k}'\beta'} [S_{\mathbf{k}'\beta' \rightarrow \mathbf{k}\beta} f_{\mathbf{k}'\beta'} (1 - f_{\mathbf{k}\beta}) - S_{\mathbf{k}\beta \rightarrow \mathbf{k}'\beta'} f_{\mathbf{k}\beta} (1 - f_{\mathbf{k}'\beta'})] \quad (\text{IV.A.1})$$

where S is the total scattering rate (sum of all mechanisms). The Monte Carlo method, applied to analyzing the electron transport in QC structures, consists of tracing a sufficient number of electrons throughout the structure over time, such that the results will be a good representation of the electron ensemble within the device. It relies on the use of random number generation, to appropriately choose from the probability distributions encountered in this type of a simulation. There are several equivalent ways

to formulate this technique.⁹⁵⁻⁹⁹ In what follows, it will be discussed how we chose to implement this technique.

B. MONTE CARLO METHOD

In general, the motion of a charged particle is due to the presence of fields, electric and magnetic, and scattering events. The time durations between scattering events, the scattering times, historically has been called the free flight times. During its time evolution, the electrons subband and momentum change, and so does the total scattering rate for all mechanisms. Consequently, the free flight times will change too. In order to be able to trace electrons throughout a structure, we must develop a method for stochastically generating these flight times. For example, consider the simple case of an electron moving under the influence of an applied electric field in the \mathbf{x}_1 direction, the k_1 component changes as $k_1 = k_{1,t=0} - |e|/\hbar |\mathbf{E}_1| t$, while the other momentum vector components remain unchanged. At the end of a free flight, the electrons momentum and energy are updated, and the electron is then scattering into its next state.

In QC structures, an electron is characterized by its subband and components of the in-plane momentum vector \mathbf{k} . Because the wavefunctions already contain the effects of the applied electric field, there is no need to include the momentum component that is in the growth direction. Next it will be discussed how to stochastically generate these free flight times for the special case when the scattering rate is constant. As will be shown, this formulation is still applicable to the more practical case where the scattering rate changes over the simulation time, as will be necessary for modeling the electrons within a QC structure.

1. Flight Times

Considering the scattering rate out of a subband to be constant $\Gamma_o = 1/t$, an electrons probability to undergo a scattering event in a duration dt is $\Gamma_o dt$, and $dn = -\Gamma_o n dt$. This simple equation can be solved to find how the population changes with time.

$$n(t) = n(0)e^{-\Gamma_o t} \quad (\text{IV.B.1})$$

The probability that the electron will scatter between t and $t+dt$, depends on the number of electrons in the subband and the scattering rate. This relation may be written as

$$dtP(t) = dt\Gamma_0 e^{-\Gamma_0 t} \quad (\text{IV.B.2})$$

where P is a random number from 0 to 1. Using the direct continuous technique⁹⁷ to stochastically generate the flight times, from equation (IV.B.2)

$$r = \int_0^{t_f} dtP(t) \quad (\text{IV.B.3})$$

where r is a random number between 0 and 1. The solution for this equation is

$$r = -e^{-\Gamma_0 t_f} + 1 \quad (\text{IV.B.4})$$

from which the flight time $t_f = -1/\Gamma_0 \ln(1-r)$ is solve for. Since r is a number between 0 and 1, so is $(1-r)$, and it is equivalent to write

$$t_f = -\frac{1}{\Gamma_0} \ln(r) \quad (\text{IV.B.5})$$

This expression allows us to stochastically generate the flight times for a constant total scattering rate.

As discussed earlier, the scattering rates will not be constant. Nevertheless, this formulation is still applicable to the case where the total scattering rate changes over the simulation time. To deal with this, we will use a clever technique formulated in the given references,^{95,96} called self scattering. Self scattering is the difference between the constant scattering rate and the actual rate. The actual scattering rate is not constant and will depend on, for instance, the scattering mechanism, in-plane momentum vector \mathbf{k} , subband of the initial electronic state, electron densities, and temperatures.

$$\Gamma_0 = \Gamma_{self} + \Gamma(\mathbf{k}) \quad (\text{IV.B.6})$$

The reason for the inclusion of this self term, is that it simplifies the calculations that follow by allowing us to treat the scattering rate as being constant. The self term will eventually be removed, so that it will have no affect on the final results of the simulation. For this technique to work, Γ_0 must always be chosen greater than the maximum actual scattering rate $\Gamma(\mathbf{k})$. The penalty paid, is that at the end of every free flight time, it must be checked to see if an actual scattering event or a fictitious self scattering event occurred. If a fictitious self scattering event occurred, no real scattering event occurred and the electrons momentum is updated and a new flight time is generated. If on the other

hand it is determined that a real scattering event occurred, the electrons energy and momentum are updated and it is then scattered into its new state, where its energy and momentum are updated for this new state. This process of checking to see if a real scattering or self scattering event occurred, can generate a considerable amount of oversampling (self scattering events). Despite the oversampling that occurs due to the inclusion of the self term, it is much better than the alternative which would require changing equation (IV.B.2) to following integral equation (which is in the exponent).⁹⁸

$$dtP(t) = dt\Gamma(\mathbf{k}, t)e^{-\int_0^t dt' \Gamma(\mathbf{k}, t')} \quad (\text{IV.B.7})$$

This equation is not suited for efficient repeated numerical calculations, and for this reason the self scattering technique is used instead.

To use equation (IV.B.5) to generate the flight times, along with the self scattering technique, Γ_o must be found for the simulation. There are different ways to implement this, we choose to use the maximum rates defined below, summing over all mechanisms (denoted by m) the maximum scattering rates $\Gamma_{\max, m}$

$$\Gamma_o = \sum_m \Gamma_{\max, m} \quad (\text{IV.B.8})$$

where

$$\Gamma_{\max, m} = \max_i \sum_f \max_{\mathbf{k}} [\Gamma_{i \rightarrow f}(\mathbf{k})] \quad (\text{IV.B.9})$$

for our initial mapping scheme in the selection process that will follow. This will thereby introduce an additional self term in the selection process,¹⁰⁰ that will also have to be removed using a straight forward rejection technique. This provides a convenient way of implementing simulations with a large number of scattering rates, with the alternative method being to choose the maximum rate as a function of \mathbf{k} value. This method of finding Γ_o is illustrated graphically in Figure IV.B.1.

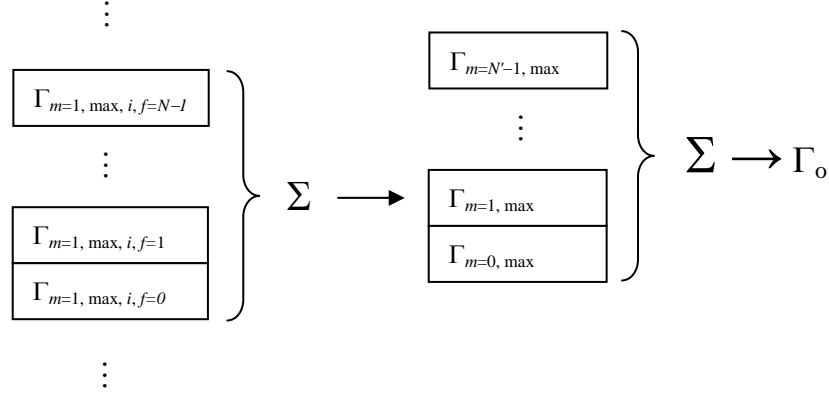


Figure IV.B.1. Graphical illustration for finding Γ_o , for the Monte Carlo method.

2. Selection Process

Now that Γ_o can be found and the flight times can be generated, we must proceed with the selection process that determines the scattering mechanism (or if a self scattering event occurred), the final state, and final energy and momentum of the followed electron. Single electron scattering mechanisms are all handled very similarly, and electron-electron scattering is a special case requiring more parameters to be determined. It will first be describe how the selection process works for the single electron scattering cases, and then for the electron-electron scattering case. Beginning with a new free flight, a random number r_0 is generated between 0 and Γ_o and mapped onto the different maximum scattering mechanisms rates, using the following bin walling procedure,^{97,101} where the mechanism $m = x$ is selected if

$$\sum_{m=0}^{x-1} \Gamma_{\max, m, i} \leq r_0 < \sum_{m=0}^x \Gamma_{\max, m, i} \quad (\text{IV.B.10})$$

If no self scattering occurs and mechanism $m = x$ is selected, the final subband state $f = y$ is chosen by generating another random number r_1 between 0 and $\Gamma_{\max, m=x, i}$ and mapping as follows

$$\sum_{f=0}^{y-1} \Gamma_{\max, m, i \rightarrow f} \leq r_1 < \sum_{f=0}^y \Gamma_{\max, m, i \rightarrow f} \quad (\text{IV.B.11})$$

Once the mechanism and final state subband have been determined, the final momentum vector $\mathbf{k}_f = k_f(\cos\theta\mathbf{x}_1 + \sin\theta\mathbf{x}_2)$ must be found. As an example, the magnitude k_f is easily found from the conservation of energy $E_{T,i} = E_{T,f}$ or for LO-phonon scattering $E_{T,i} = E_{T,f} \pm E_{LO}$, where $E_T = E_n + \hbar^2 k^2 / 2m$. The angle θ can be found by using another Monte Carlo technique. First the angle is randomly chosen from a uniform distribution between 0 and 2π . The self term is removed using a rejection technique, which is an iterative scheme keeping the choice if

$$r \leq \frac{P(\theta)}{P_{\max}} \quad (\text{IV.B.12})$$

and otherwise rejecting it. $P(\theta)$ is found from the corresponding scattering mechanism equations by

$$P(\theta) = \frac{K}{\int d\theta K} \quad (\text{IV.B.13})$$

where K is the kernel inside the scattering rate integral. This selection process and how it unfolds is graphically illustrated in Figure IV.B.2.

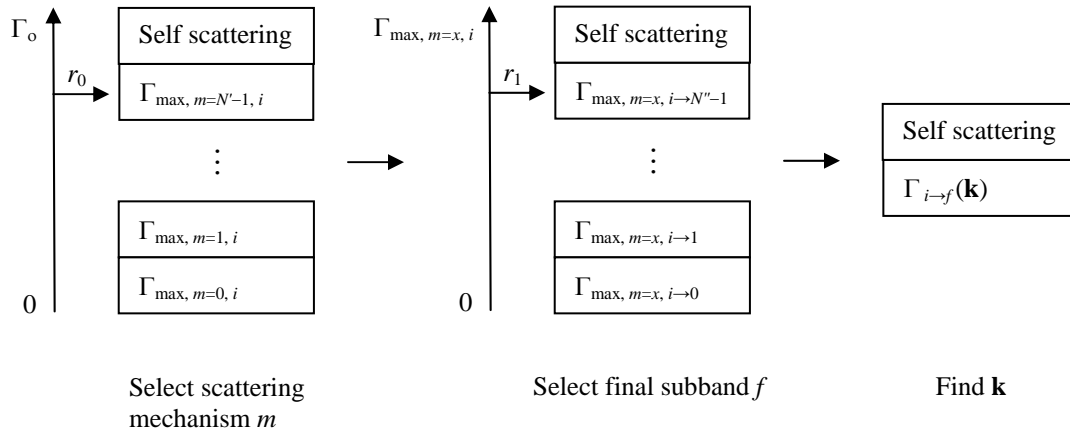


Figure IV.B.2. Graphical illustration of the Monte Carlo selection process.

For electron-electron scattering, many more additional terms must be found. The subband i , k_i and θ_i of the initial followed electron (three parameters) are known, and these three parameters for the second or parent electron to scatter with must be found, as

well as for the two final state electrons. In our implementation, this is done by bin walling in a similar fashion as discussed earlier, to find the *ijfg* process (a mapping look up scheme is used). A parent electron is then randomly chosen from the other electrons within subband j of the ensemble, which determines j , k_j , and θ_j . Since f and g are known, only four parameters remain to be found (k_f , θ_f , k_g , and θ_g). Only one of these really needs to be found though, as the others are dependant by the conservation of energy and momentum. We chose θ_f randomly from a uniform distribution between 0 and 2π , then using equations from section III.B (equations (III.B.69) *et cetera*), the other three parameters can be found. The self term can be removed by solving for $q_{||}$ from equations (III.B.52) or (III.B.71), and using the rejection technique of equation (IV.B.13).

C. IMPLEMENTATION

A flow chart describing the Monte Carlo simulation is shown in Figure IV.C.1. The algorithm consists of calculating the scattering rates and the main Monte Carlo selection process previously described. Because a QC structure is periodic and charge is conserved, when an electron with in-plane wavevector \mathbf{k} is scattered into another section, an electron is introduced with the same \mathbf{k} vector into an equivalent state in the section being modeled. Typically, the center section of a three section structure is modeled. Initially the electrons are distributed thermally at the lattice temperature according to Fermi-Dirac statistics, in one or more energy levels. In theory, the scattering rates need to be recalculated every time an electron scatters to a new state. However, in practical implementation of this algorithm, the scattering rates need only be calculated after an evolved time step duration Δt , and this duration of time is chosen such that the scattering rates do not change too much. For example, a $\Delta t \sim 0.1$ psec might be needed for quickly changed transient times. So in practice, each electron in the ensemble is traced for a time step duration Δt , then the scattering rates are recalculated based on the new subband populations and electron distributions. In this way, the scattering rates are consistently solved for using the correct subband distributions, as the time evolution of the ensemble unfolds. This allows for state blocking to be taken into account, and ensures that density and temperature dependant scattering rates are correctly modeled. The number of

particles must be chosen enough for accurate calculation, and typically $\sim 10^4$ is adequate for most simulations. Note that it is not that important how many electrons or the sheet density each particle represents, only that there are enough for accurately statistically modeling the ensemble within the structure.

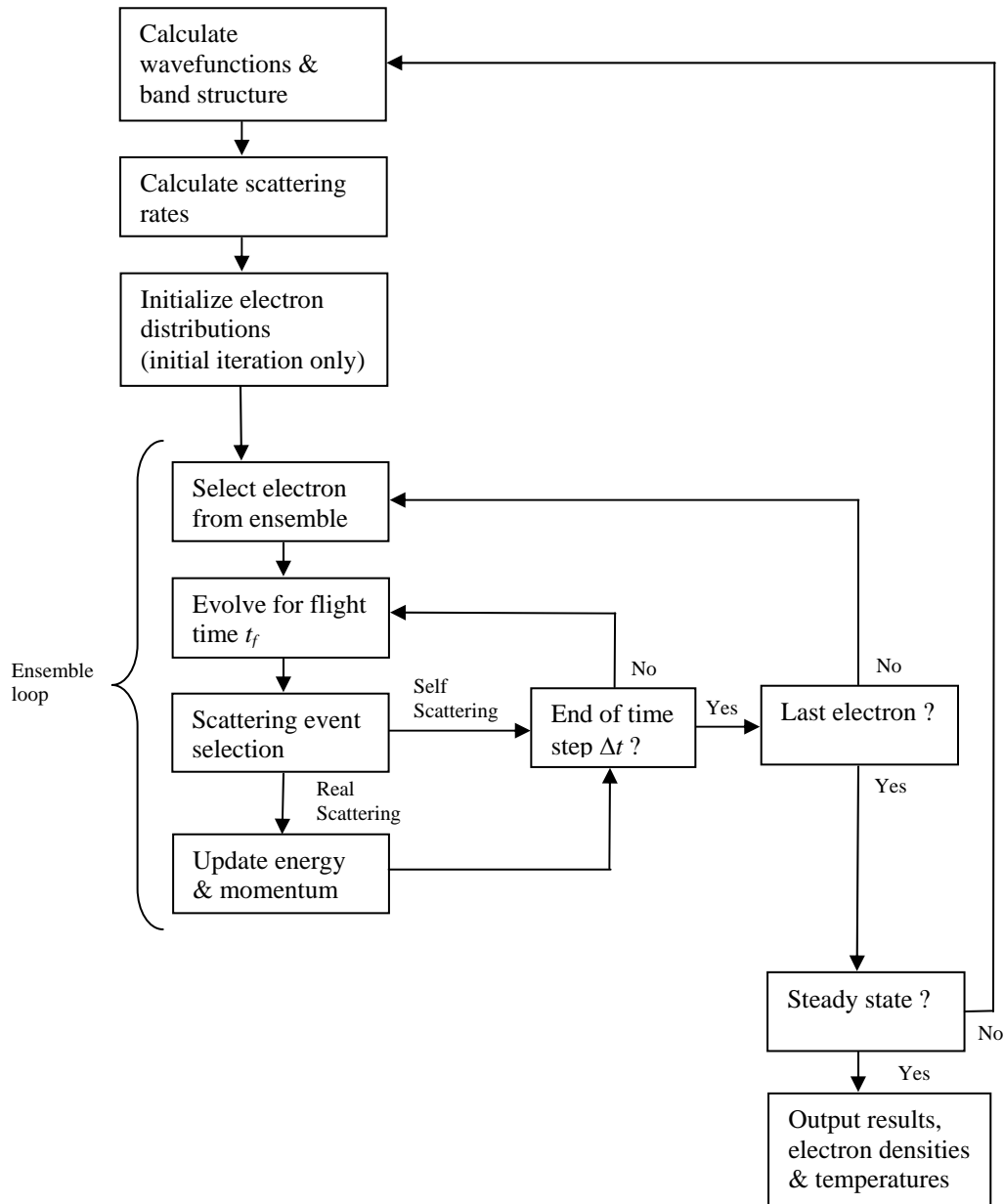


Figure IV.C.1. A flow chart for the Monte Carlo simulation of QC structures.

Because the scattering rate calculations are the time consuming part of the simulation, we choose to calculate and store the rates before each time duration. That way, the rates are only calculated once for each time step duration. The Monte Carlo algorithm is continued until it is determined that state populations have reached steady state and are not changing. This is done by making sure the variance of the populations is below some minimum acceptable value. Once steady state is reached, the electron densities and temperatures are output, and other parameters such as various scattering rate lifetimes, current density, and gain are easily found (all scattering events are stored). As an example of a typical simulation, shown in Figure IV.C.2 is a Monte Carlo simulation of QC structure D619F10E which has six energy levels within one section (the details of this structure will be discussed later), where all electrons were initially distributed in state 2 at the lattice temperature of $T = 25$ K.

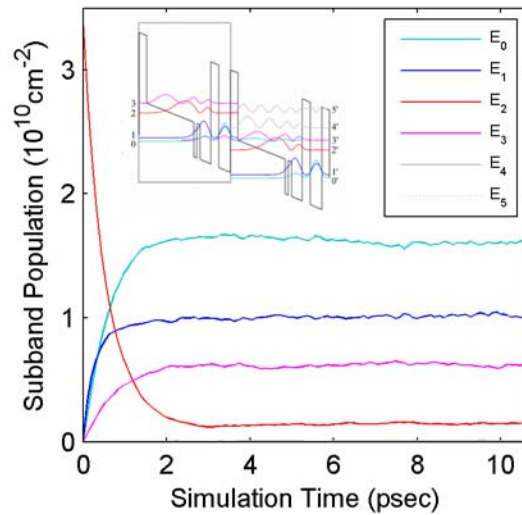


Figure IV.C.2. Monte Carlo simulation of structure D619F10E at a bias of 53.6 mV/section, with all electrons initially distributed in state 2. Inset: Two sections of the structure are shown, with one section outlined.

Under the transport picture described by this type of Monte Carlo simulation, where the scattering between electronic states is determined by the spatial wavefunctions solved via Schrödinger's equation, coherence effects are not taken into account. For example the peak current through a thickened barrier is not affected, only its transmission

sharpness decreases, and this is not accurate. This implies that the scattering is not a fully coherent process and scattering between weakly coupled states with a small anticrossing is mostly a noncoherent process, due to dephasing scattering that effectively interrupts or scrambles the phase coherence. No phenomenological dephasing parameter is introduced in our simulations. This can sometimes lead to optimistic results as well as an overestimation of the scattering between states with a small anticrossing, and hence an overestimation of the current density when aligned with weakly coupled parasitic current channels. The scattering between more than one section is taken into account in step well structures because of the nature of the step well QC structure (which potentially can further lead to an overestimation of the scattering between weakly coupled states). The scattering mechanisms that are included are LO-phonon, electron-electron, impurity, and interface roughness scattering. These scattering rates are calculated via Fermi's golden rule. All rates from these simulations are net rates and include backscattering. State blocking and screening are also included in the simulations. Next we discuss waveguide structures commonly used in QCLs for the confinement of emitted photons.

V. WAVEGUIDE AND RESONATOR

QCL devices are fabricated by growing N repeated sections for the active region, and then processing the wafer sample into a waveguide to form the laser resonator. In these sections, waveguide parameters of interest and the two common types of waveguide structures, surface plasmon and metal-metal waveguides, are discussed. A third structure, a metal-patterned substrate waveguide was also investigated.

A. QCL RESONATORS

The waveguide and resonator are important, because the losses essentially set the threshold condition. At threshold, the gain equals the losses. The threshold gain can be found by considering a one round trip inside the resonator as follows

$$I_o e^{-2\alpha_w L} R_0 R_1 e^{2\Gamma \times \text{gain} \times L} = I_o$$

$$\text{gain}_{th} = \frac{1}{\Gamma} \left(-\frac{1}{2L} \ln(R_0 R_1) + \alpha_w \right) = \frac{(\alpha_m + \alpha_w)}{\Gamma} \quad (\text{V.1})$$

where I_o is the initial intensity, $\alpha_m = -1/2L \ln(R_0 R_1)$ is the mirror loss, α_w is the waveguide loss, L is the length of the resonator, and R is the intensity reflectivity at a facet. The approximation that the mode gain = $\Gamma \times \text{gain}$ has been used. The confinement factor Γ , is defined as the ratio of the guided energy inside the active region to the total energy of the wave

$$\Gamma = \frac{\text{Re} \left\{ \int_{\text{active region}} d^2 x \mathbf{S} \cdot \hat{\mathbf{n}} \right\}}{\text{Re} \left\{ \int_{\text{all space}} d^2 x \mathbf{S} \cdot \hat{\mathbf{n}} \right\}} \quad (\text{V.2})$$

where $\mathbf{S} = \frac{1}{2} \mathbf{E} \times \mathbf{H}^*$.

Since the waveguide mode is attenuated, the propagation constant is complex $\beta = \beta' + i\beta''$, noting that $\alpha_w = 2\beta''$. In terms of the electric field and considering the case where the field facet reflectivity $r = r_m e^{i\phi}$ is the same for both facets, the following can be written

$$e^{-i2\beta L} r_m^2 e^{i2\phi} e^{\Gamma \times gain \times L} = 1 \quad (V.3)$$

In general, it is seen from the phase terms that the Fabry-Pérot resonance condition is found $\beta'L = n\pi - \phi$. By ignoring ϕ , which is often done for optical systems, at resonance the usual condition is found $L = n\lambda_g/2$. Next, the types of waveguides used for QCLs will be discussed.

B. SURFACE PLASMON AND METAL-METAL WAVEGUIDES

Two types of optical confinement structures for THz QCLs have been used, the semi-insulating (SI) surface plasmon and the metal-metal waveguides.^{1,32,102-104} A third type of waveguide similar to the metal-metal waveguide, the metal-patterned substrate waveguide, was also analyzed (Figure V.B.1).

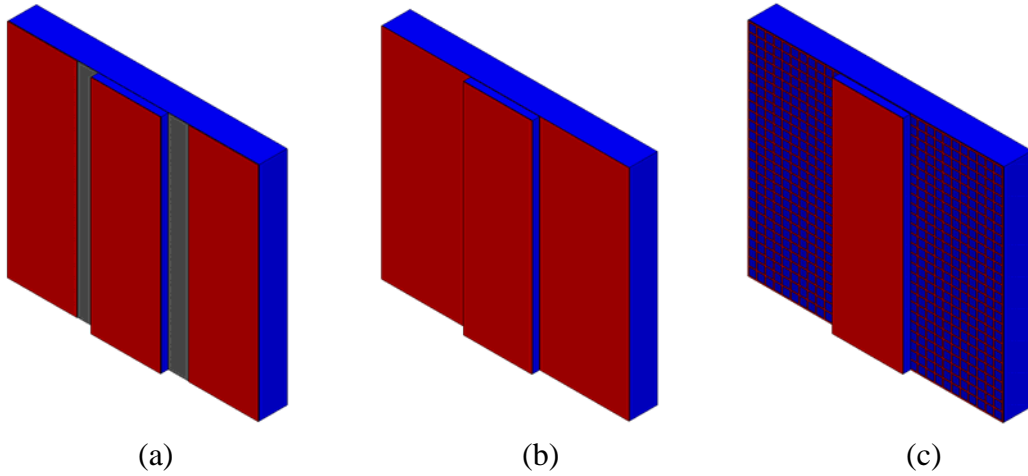


Figure V.B.1. QCL waveguides, the (a) surface plasmon, (b) metal-metal, and (c) metal-patterned substrate waveguides.

The surface plasmon waveguide (Figure V.B.1(a)) consists of a metallic top and two side contacts, and a thin n+ doped semiconductor layer or plasma layer (where the real part of the permittivity is negative) sandwiched between the active region and the SI GaAs substrate. Gaps are present between the sides of the active region and the metallic lateral contacts. This type of structure is easier to fabricate than the metal-metal waveguide since it does not require substrate removal and wafer bonding. Since the fields extend substantially below and outside the active region, the confinement factor is less

than that of the metal-metal waveguides. However, the advantage can be improved output coupling for higher power applications.¹³

The metal-metal waveguide consists of two metallic layers above and below the active region (Figure V.B.1(b)) which is above a n+ GaAs substrate. The fields of the mode are usually well confined with often a near unity confinement factor, which can lead to lower threshold gains. The waveguide width may often be made smaller, than the surface plasmon waveguide counterpart, with acceptable performance. This can allow for reduction in the device area. The metal-metal waveguide is also better suited for higher operating temperatures.¹³ The disadvantage is that the output coupling is worse due to the high reflectivity of the subwavelength rectangular aperture, and the radiated beam pattern is much more fan shaped. At THz frequencies, we are in a waveguide region in which the Fresnel reflection coefficient is not valid to use for the reflectivity for the metal-metal waveguide. The high reflectivity is an advantage in the sense that a high reflectivity (HR) coating on one facet end is rarely needed with this type of waveguide. Although perhaps difficult to fabricate, others have shown improved output power in metal-metal waveguides by micromachining a matching horn antenna on the facet end.¹⁰⁵ Both the surface plasmon and metal-metal configurations use surface plasmons attached to the contact layers.

The waveguide losses and reflectivities for the waveguides, are found using finite element method (FEM) solvers.^{106,107} The Drude model⁸² is used to determine the material parameters, in which the complex permittivity can be found from

$$\varepsilon(\omega) = \varepsilon_b + i \frac{n_{3D} e^2}{m \omega \left(\frac{1}{\tau} - i \omega \right)} \quad (\text{V.4})$$

where $|e|$ is the charge of the electron, m is the effective mass of the electron, and ω is the frequency. In our simulation model, the active region was nominally taken as GaAs and ε_b was set to 12.4 corresponding to the $T = 0$ K value. The relaxation times τ , were set to 0.1 ps for the n+ layers, 0.5 ps for the active region, and 0.06 ps for the metallic gold layers.¹⁰⁸⁻¹¹⁰ For the active region a background carrier concentration of $2 \times 10^{15} \text{ cm}^{-3}$ was assumed, and a concentration of $5 \times 10^{22} \text{ cm}^{-3}$ was used for the metallic gold layers. The

plasma and contact layers concentrations vary by design, and are listed in those particular sections. From Ampère's law $\nabla \times \mathbf{H} = \mathbf{J} + d\mathbf{D}/dt = \sigma \mathbf{E} - i\omega \mathbf{D}$ and equation (V.4), it is seen the complex permittivity can alternatively be entered as a real valued permittivity ϵ_b and a complex conductivity $\sigma = n_{3D}e^2 \tau / m(1 - i\omega\tau)$. Additionally, it can also be entered as a real valued effective permittivity ϵ' and a real valued effective conductivity $\omega\epsilon''$ since $\nabla \times \mathbf{H} = \omega\epsilon'' \mathbf{E} - i\omega\epsilon' \mathbf{E}$, noting that ϵ' can be a positive or negative value. By considering ω in the high frequency limit, the plasma frequency may be defined as $\omega_p = (n_{3D}e^2 / \epsilon_b m)^{1/2}$. Since $ck = (\omega^2 - \omega_p^2)^{1/2}$ it is seen that when $\omega < \omega_p$, k is purely imaginary and waves incident on the plasma are reflected and waves inside fall off exponentially with distance, thus the medium behaves more like a "metal." For $\omega > \omega_p$ transmission occurs and the medium has more of a lossy "dielectric" characteristic.

A waveguide similar to the metal-metal waveguide, the metal-patterned substrate waveguide, was also briefly investigated (Figure V.B.1(c)). The idea was if MBE growth of the active region could be accomplished on top of a patterned substrate, this could avoid having to wafer bond while at the same time keep a structure capable of maintaining a high confinement factor. It was ultimately determined that the defects introduced by the growth process over the patterned substrate, would likely be unacceptable for high quality MBE growth. Nevertheless, the results of the analysis will be briefly mentioned, as similar type of 3D analysis could be useful for mode suppression waveguides. In such a waveguide, a metallic layer would be deposited on the top surface of the active region, and the pattern would also have to be dense enough to keep the modes confined while also not substantially increasing the waveguide loss. Our analysis showed for the guides we modeled, compared to metal-metal waveguides, that the confinement factor was affected little by square patterns from 1 by 5 μm (1 μm thick strips with 5 μm spacing between the strips) to 2 by 2 μm , but the waveguide loss was increased for the less dense patterns. It was also shown for a 2 by 2 μm pattern waveguide, that the waveguide loss could be made lower using a n+ substrate (as opposed to a SI substrate with a thin n+ layer) for frequencies beyond about 2.5 to 5 THz.

VI. THz LO-PHONON QC STRUCTURES

Two different LO-phonon approaches were investigated, the new step well QC structures we proposed,^{40,111-113} and a conventional square well design. Approximate rate equation analysis was initially performed on the step well structures, and the structures were analyzed using Monte Carlo simulations. The analysis indicated the injector of one of the step well structures could further be improved, and simulations on a modified structure showed a more uniform gain over a range of biases. Simulations were also performed on a high power square well LO-phonon design. Our analysis was compared to experimental measurements, and found to be in reasonable agreement.

A. STEP WELL QC STRUCTURES

Even though it is possible to arrange the energy levels in a step well such that the radiative transition and LO-phonon transition are within the same step well, this does not mean it will necessarily be useful for a laser application. For the device to lase, a population inversion must be kept for sufficient gain to overcome the losses. While intrawell radiative transitions can have large overlap of the electron wavefunctions that yield large oscillator strengths, there can be a trade-off between the oscillator strength and upper state lifetime, as the scattering from the upper radiative state to the lower state is usually increased with increasing oscillator strength in three-level LO-phonon structures. This increase in oscillator strength is one of the reasons for studying these step well structures, as increasing the oscillator strength can increase the gain and hence the output power of a device. As will be shown, the section length will remain about the same as other LO-phonon designs.

Initially, an approximate rate equation analysis was performed on the step well structure shown previously in Figure II.B.1(b).^{40,111} The scattering rates (W_{21} and W_{10}) must be calculated for the step quantum well structures in order to estimate whether a population inversion is likely between states 2 and 1. The simplest rate equation analysis allows us to write the population of the middle state 1 (n_1) as

$$\frac{dn_1}{dt} = n_2 W_{21} - n_1 W_{10} \quad (\text{VI.A.1})$$

where n_2 is the population of state 2. The necessary and intuitive condition at steady state for a population inversion to exist ($n_2 > n_1$) is $W_{10} > W_{21}$ (in terms of corresponding lifetimes $\tau_{10} < \tau_{21}$). In general, the scattering rates are a combination of all possible scattering mechanisms, i.e., electron-phonon, electron-electron, impurity, and interface roughness scattering. In this approximate rate equation analysis, we estimate the scattering rates by taking into account the LO-phonon and electron-electron scattering rates. As will be seen later from our Monte Carlo analysis, the electron temperatures can be ~ 50 to 100 K or higher than the lattice temperature. For the rate calculations that follow, the lattice temperature will be taken to be 25 K and the electron temperature to be 100 K.

Figure VI.A.1 shows the mean LO-phonon scattering rates for the 4.3 THz step quantum well previously shown in Figure II.B.1(b) (and shown again inset), calculated for initial state populations from 1×10^9 to $1 \times 10^{10} \text{ cm}^{-2}$ for $T_{\text{lattice}} = 25$ K and $T_{\text{electron}} = 100$ K. All of the scattering rates are essentially constant and independent across the populations computed. As expected, the 2 to 1 transition has the smallest mean scattering rate and hence the longest lifetime, because the energy spacing of 17.9 meV between states 2 and 1 is below the LO-phonon energy spacing of about 36 meV. Only the electrons with sufficiently high in-plane kinetic energy ($\sim 36 - 17.9 = 18.1$ meV or higher) can participate in the scattering process, while others are forbidden. The maximum scattering rate, which occurs when the electron has just enough in-plane energy such that the energy difference is exactly at the resonant LO-phonon energy $\hbar\omega_{LO}$, is also shown in Figure VI.A.1. It can be seen that the mean scattering rates for the 1 to 0 transition are faster than the 2 to 1 transition, and are even faster than the 2 to 1 maximum rate. Also included is the parasitic mean scattering rate for the 2 to 0 transition. This parasitic lifetime is 1.8 picoseconds (psec), which is relatively short. These scattering rates show that the mean lifetimes are such that $\tau_{21} = 5.6 \text{ psec} > \tau_{10} = 0.37 \text{ psec}$. This indicates that the LO-phonon rates are favorable for keeping a population inversion. Of course, the population inversion is affected by all scattering mechanisms,

not just by the electron-phonon scattering rates. Next we will calculate the electron-electron scattering rates and see how incorporating these rates may affect the population inversion analysis.

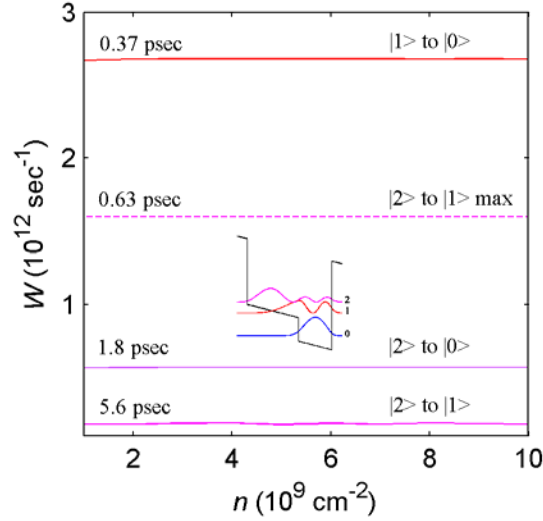


Figure VI.A.1. Mean LO-phonon scattering rates for the 4.3 THz step quantum well (shown inset) as a function of initial state populations for $T_{lattice} = 25$ K and $T_{electron} = 100$ K (solid lines). For the 2 to 1 transition the maximum scattering rate (which is not an averaged rate) is also shown (dashed line). The lifetimes are listed (reciprocals of the essentially constant scattering rates).

The electron-electron scattering rates were calculated for the same 4.3 THz structure as for the LO-phonon analysis using $T_{electron} = 100$ K for initial state populations of 1×10^9 to 1×10^{10} cm^{-2} . Figure VI.A.2 shows the electron-electron scattering rates for the 2 to 1 and 1 to 0 transitions that pertain to the simplified rate equation analysis already discussed. It is seen that the dominant scattering rate is the 2010 process. Unlike the earlier LO-phonon analysis, the electron-electron scattering rates are not constant but rather as expected, increases with carrier concentration. The next highest scattering rates are for the 2221 process, and the lowest scattering rates are for the 1110 process. The total electron-electron scattering rates are the sum of the above processes, taking into account the number of electrons that change energy levels. Figure VI.A.3(a) shows the total electron-electron scattering rates for the 2 to 1 and the 1 to 0 transitions, based on the processes for the simplified rate equation analysis. It is clear that the 2 to 1 scattering

rates are higher than the 1 to 0 scattering rates for all the initial carrier populations. Thus the lifetimes are such that the electron-electron scattering process by itself is not favorable for the purpose of keeping a population inversion.

Although our analysis so far has been in the framework of the simplified rate equation analysis and has considered only processes within that framework, it is worth mentioning that in general a system with N number of energy levels will have 4^N electro-electron scattering processes. Some of these processes do not directly by themselves affect subband populations, i.e., intrasubband *iiii* scattering rates where no net change occurs in the number of electrons in the subband. To see what the scattering rates are for some of the additional processes, computed in Figure VI.A.3(b) are the mean electron-electron scattering rates for the additional 2110, 2210, and 2220 scattering processes. It is seen that of these three, the 2110 process is dominant and involves a net change of losing one electron from state 2 and gaining one electron in state 0, a process by which $2 \rightarrow 1$ and $1 \rightarrow 0$. The scattering rate due to this process is around an order of magnitude less than those considered earlier.

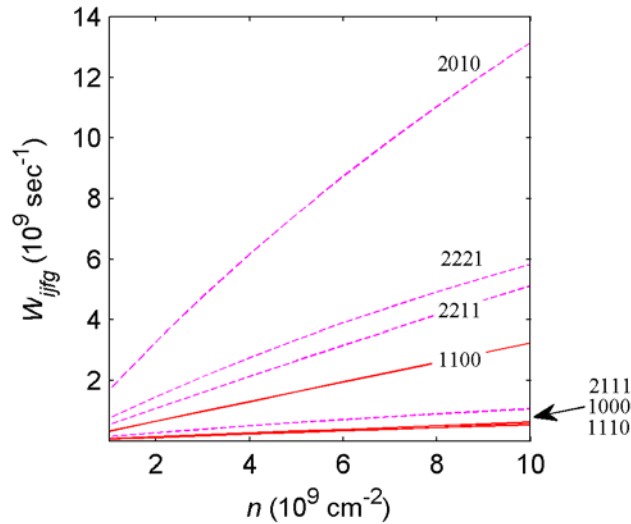


Figure VI.A.2. Mean electron-electron scattering rates for the 4.3 THz step quantum well as a function of initial state populations for $T_{electron} = 100$ K. The various scattering processes for the 2 to 1 and the 1 to 0 transitions for the simplified rate equation analysis are shown.

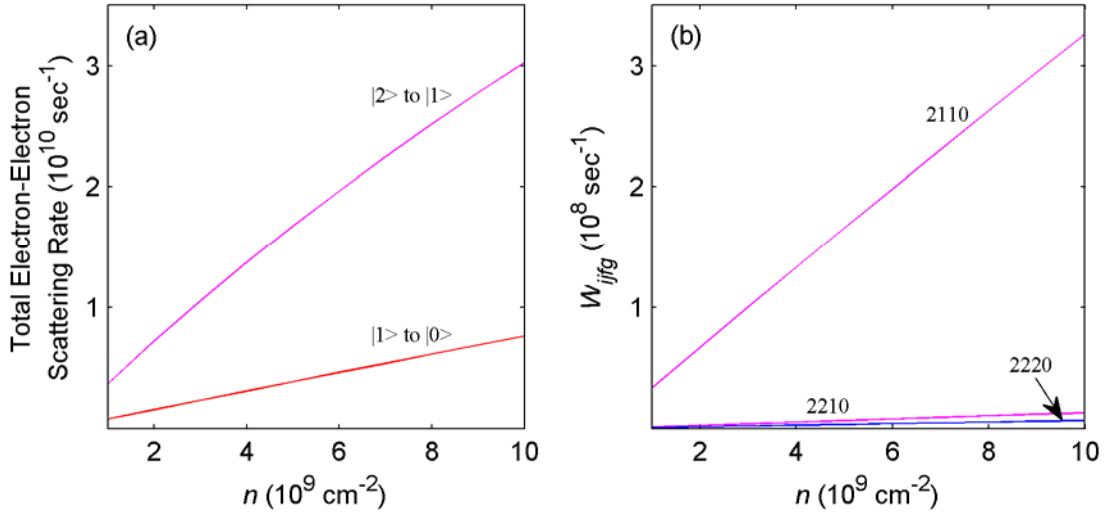


Figure VI.A.3. Scattering rates for the 4.3 THz step quantum well for $T_{electron} = 100 \text{ K}$. (a) The total electron-electron scattering rates for the 2 to 1 and the 1 to 0 transitions, based on the processes for the simplified rate equation analysis, as a function of initial state populations. (b) The mean electron-electron scattering rates as a function of initial state populations for $T_{electron} = 100 \text{ K}$, for some additional scattering processes for the 2 to 1 transition that are not within the framework of the simplified rate equation analysis.

The analysis indicates that the electron-phonon scattering rates are around an order of magnitude larger than the electron-electron scattering rates. The scattering rate analysis of the biased step quantum well indicates that this type of structure is likely capable of keeping a population inversion for the temperatures and range of carrier concentrations considered.

In order to be used in a QC structure, the step quantum well must have an injector section to feed the next section of the cascade. One potential implementation is illustrated in Figure VI.A.4 where one section is outlined.⁴⁰ The double barrier injector section was designed to maintain the upper state lifetime, while allowing the electrons in the lower states to resonantly tunnel to the upper state of the next adjacent section. The conduction band profile was solved by using a self consistent solution to Schrödinger's and Poisson's equations. The step well has been shaped to spatially separate the upper state and lower states as much as possible, in an effort to reduce scattering between those states. The radiative transition takes place between states 4 and 3, where $E_{43} = 16.6 \text{ meV}$ (4 THz or $\lambda \sim 75 \mu\text{m}$). The LO-phonon assisted transition takes place from state 3 to the lower triplet

states (2, 1, 0), since $E_{31} = 36.6$ meV which is near $\hbar\omega_{LO}$. Scattering between the triplet states (2, 1, 0) and injection into the next adjacent sections upper state is to take place. The step well has been arranged so that state 4 is above the step and state 3 below the highest point, in an effort to spatially separate the wavefunctions for efficient injection to the upper state 4 and for reducing the parasitic injection to state 3. Thus, the step barrier helps to reduce unwanted injection into the middle state, which is a problem with other square well LO-phonon structures.

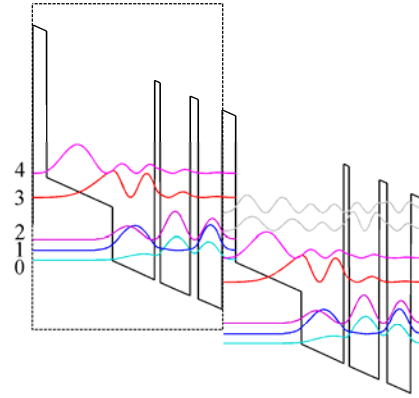


Figure VI.A.4. Conduction band profile of a proposed step well QC structure found using a self consistent solution to Schrödinger's and Poisson's equations. The step well and resonant tunneling double barriers of one section are outlined. Beginning with the left injector, the $\text{Al}_x\text{Ga}_{1-x}\text{As}$ layers compositions are 0.143/0.035/0/0.143/0/0.143/0 and thicknesses in nm are 4.3/20.9/13.5/1.7/9.6/2.5/7.6, with $E_{43} = 16.6$ meV (4 THz) and $E_{31} = 36.6$ meV. The applied field is 9.5 kV/cm. The 9.6 nm well is doped $2.9 \times 10^{16} \text{ cm}^{-3}$, which corresponds to a sheet density of $2.8 \times 10^{10} \text{ cm}^{-2}$.

The mean electron-phonon scattering lifetimes for this structure are $\tau_{3 \rightarrow (2,1,0)} = 0.4$ psec, for the upper to lower states scattering $\tau_{4 \rightarrow (2,1,0)} = 1.4$ psec, and $\tau_{43} = 7.9$ psec. Again, because these are intrawell transitions, the scattering rates computed are relatively fast. The radiative transition is also an intrawell transition, and the overlap of the wavefunctions is reasonably good, which gives an oscillator strength of about 1.34. This oscillator strength is higher than the highest reported LO-phonon designs³⁷ (~ 40% increase), and the section length is about the same, i.e., about half that of typical bound to continuum designs.

To get an approximate estimate of what might be expected for this type of structure, we can estimate from the gain equation (equation (III.D.27)) the population inversion. If we assume a total loss of $\sim 40 \text{ cm}^{-1}$ (which is reasonable for surface plasmon waveguides) and assume a $FWHM \sim 4 \text{ meV}$, the estimated 2D population at threshold is $\sim 2.5 \times 10^9 \text{ cm}^{-2}$. This is within the carrier densities used in our analysis. The current density can be estimated from $\Delta n_{2D} \sim (J/e)\tau_4(1-\tau_3/\tau_{43})$ and is calculated to be $J \sim 760 \text{ A/cm}^{-2}$.

It was concerned that the triplet of lower states spacing was too close to the radiative energy spacing and could provide a means for unwanted absorption. Further, more energy separation was wanted between the lower states and an unused state in the next adjacent section. For this reason, it was decided to focus on single well injector designs. There were a number of different step well structures that were considered, some of which are shown in Figure VI.A.5.¹¹² Other structures (not shown), that resonantly tunneled the middle and lower states, step well designs without all three energy levels in the same well, and some structures that would also have required growth with more than two Al compositions in an $\text{Al}_x\text{Ga}_{1-x}\text{As}$ heterostructure, were considered as well. Due to the difficulty in growing a sample of repeated sections with more than two Al compositions in most MBE chambers, structures requiring only two Al compositions were favored.

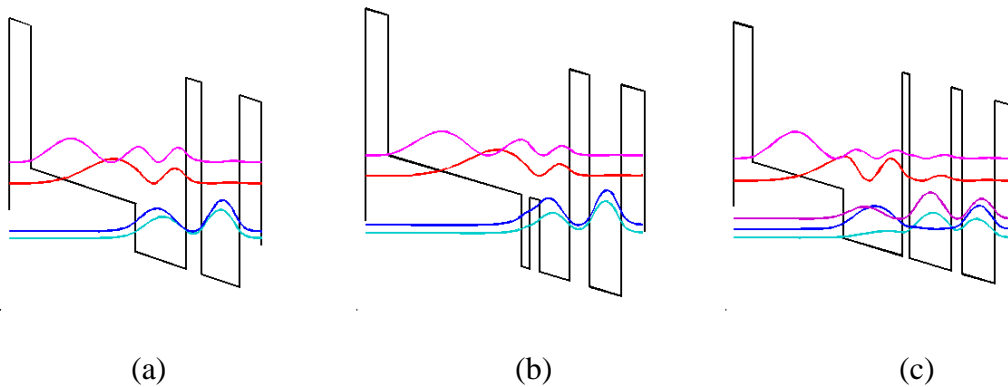


Figure VI.A.5. Some of the step well QC structures considered, (a) one step, one well injector, (b) two step, one well injector, and (c) one step, two well injector.

By using a single well injector, the anticrossing between the lower ground states can be kept much smaller than the optical transition energy spacing (as there will only be a doublet of states), thereby reducing the possibility of absorption. Initially a single step well and one well injector (Figure VI.A.5(a)) structure was analyzed. To avoid a potential parasitic current channel (from alignment with an unwanted energy state in the next adjacent section), the injector well was narrowed so that the only energy state from the well was that of the lowest ground state. This increased the sub-picosecond LO-phonon lifetime of the middle state to ~ 1 psec which was too slow. Rather use a wider injector well to keep the sub-picosecond LO-phonon scattering lifetime and also introduce a second state from the well which could potentially produce a parasitic current channel, it was chosen to utilize a two step well and one well injector as shown in Figure VI.A.5(b) (where the two steps are of equal Al composition). This structure, QC structure D619F10D, will be discussed in the next subsection. The disadvantage, however, is that it introduces two additional growth layers (7 growth layers as compared to only 5 growth layers for a single step well one well injector design). Nevertheless, even with a two equal Al composition step well, this structure is quite simple having only two wells. Albeit the first being a step well. It also has only one additional layer compared to the simplest square well LO-phonon QC structure.³⁹ Note that in principle, a step well QC structure does not need an injector well (in which it would be a one well design).

1. Structure D619F10D

The conduction band profile for QC structure D619F10D is shown in Figure VI.A.6. Electrons are injected into the upper state 3 and the radiative transition occurs between state 3 and middle state 2, where $E_{32} = 15.1$ meV (~ 3.6 THz or $\lambda \sim 82$ μm). The LO-phonon assisted transition takes place from the middle state 2 to the lower doublet states (1, 0), since $E_{21} = 37.2$ meV which is near $\hbar\omega_{LO}$. This ensures fast depopulation of state 2 via LO-phonon scattering, with a mean scattering rate $\tau_{2 \rightarrow (1,0)} = 0.68$ psec (0.44 psec band edge). The anticrossing between states 2 and 5' is relatively small due to the thick collector and injector barriers, and therefore should not be a primary path of scattering out of state 2. Though any electrons that transition from state 2 to 5' would serve to help the population inversion, and state 5' is near the resonant LO-phonon energy

spacing to upper state 3'. Injection from the lower doublet states (1, 0) is to take place into the next adjacent sections upper state 3', and the injector anticrossing $E_{03'} \sim 1$ meV. The step well has been arranged so that state 3 is above the step and the state 2 below the highest point so as to provide spatial separation at the injector barrier for improved injection.

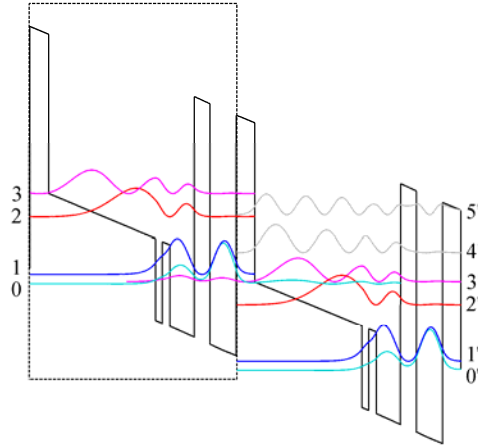


Figure VI.A.6. Conduction band profile of structure D619F10D found using a self consistent solution to Schrödinger's and Poisson's equations. The step well and resonant tunneling well of one section are outlined. Beginning with the left injector, the $\text{Al}_x\text{Ga}_{1-x}\text{As}$ layers compositions are 0.16/0.05/0/0.05/0/0.16/0 and thicknesses in nm are 4.8/27.9/1.8/2/6.3/4.1/6.8, with $E_{32} = 15.1$ meV (3.6 THz) and $E_{21} = 37.2$ meV. The applied field is 10.5 kV/cm. The center 2 nm of the 6.8 nm well is doped to a sheet density of $3.4 \times 10^{10} \text{ cm}^{-2}$.

Since the transitions are intrawell in nature, the LO-phonon scattering is relatively fast. The radiative transition is also intrawell, and the overlap of the wavefunctions is reasonably good, giving an oscillator strength of ~ 1.03 at 9.9 kV/cm (53.2 mV/section).

In order to determine the threshold gain required for lasing, two different commonly used waveguide structures, the surface plasmon and metal-metal waveguides were considered. The threshold gain was determined for both surface plasmon and metal-metal waveguide resonator configurations at the operating frequency.¹¹³ The analysis was performed assuming an active region thickness of $\sim 10 \mu\text{m}$ (which corresponds to $N \sim 185$ sections) and a guide width of $200 \mu\text{m}$. This is because the threshold gain is worse (higher) for smaller width ridges. The threshold gain $= (\alpha_m + \alpha_w) / \Gamma$, where α_m is the

mirror loss and α_w is the waveguide loss. The waveguide losses and reflectivities for the metal-metal waveguide were found using finite element method (FEM) solvers.^{108,109} The Drude model was used to determine the material parameters, and a background carrier concentration of $2 \times 10^{15} \text{ cm}^{-3}$ was assumed. Due to the difficulty in accurately modeling the waveguide with N thinly doped active region section layers, the doping in these thin layers was neglected. Thus, the actual waveguide losses may be higher.

Considering the surface plasmon waveguide first, the side contacts spacing was set at 50 nm to keep the mode from coupling to avoid higher waveguide loss. The top contact plasma layer was 60 nm thick and doped at $5 \times 10^{18} \text{ cm}^{-3}$. To determine a suitable lower plasma layer thickness, the threshold gain was computed as a function of lower plasma layer thickness for doping concentrations of 1×10^{18} to $3 \times 10^{18} \text{ cm}^{-3}$. The mirror losses have been computed for resonator lengths of 1 and 2.5 mm with one facet of the waveguide assumed to have a HR coating. Figure VI.A.7 shows that for the lowest threshold gain over the range of mirror losses considered (resonator lengths of 1 and 2.5 mm), the optimal lower plasma layer is one doped $\sim 2 \times 10^{18}$ to $3 \times 10^{18} \text{ cm}^{-3}$ at a thickness of 400 to 500 nm.

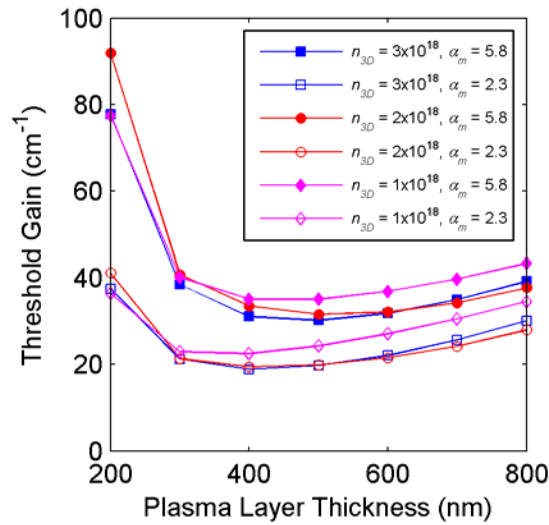


Figure VI.A.7. Threshold gain for a 200 μm ridge, 10 μm thick surface plasmon waveguide, as a function of lower plasma layer thickness for different doping concentrations (cm^{-3}) and mirror losses (cm^{-1}).

The cross-section 2D mode intensity and 1D profile mode intensity are shown in Figure VI.A.8 for a lower plasma thicknesses of $t_{\text{plasma}} = 500$ nm, doped at $3 \times 10^{18} \text{ cm}^{-3}$. The confinement factor is $\Gamma = 0.28$ and the waveguide loss is $\alpha_w = 3.3 \text{ cm}^{-1}$ for this waveguide.

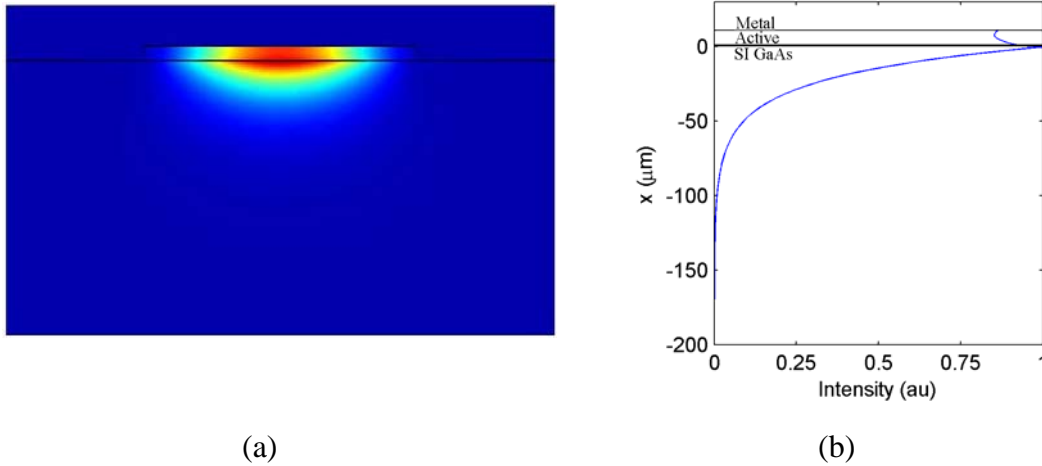


Figure VI.A.8. $200 \mu\text{m}$ ridge, $10 \mu\text{m}$ thick surface plasmon waveguide with $t_{\text{plasma}} = 500$ nm doped at $3 \times 10^{18} \text{ cm}^{-3}$, (a) cross-section 2D mode intensity, (b) 1D profile mode intensity.

Next, the threshold gain was computed for a metal-metal waveguide, where the top and lower contact plasma layers were 60 nm thick (10 and 50 nm layers doped at 5×10^{19} and $5 \times 10^{18} \text{ cm}^{-3}$, with the lower contact also having a 3.5 nm LTG GaAs layer). For the metal-metal waveguides, we assume both facets are uncoated. We find the threshold gain to be 7.7 and 5.7 cm^{-1} for mirror losses corresponding to resonator lengths of 1 and 2.5 mm respectively. The attenuation was calculated to be $\alpha_w = 4.3 \text{ cm}^{-1}$ with a confinement factor $\Gamma \sim 1$. This near unity confinement factor is seen as evident from the cross-section 2D mode intensity graphed in Figure VI.A.9. Optimal guide parameters for a surface plasmon waveguide depend on having a relatively thick lower contact layer compared to the upper contact layer, while for a metal-metal guide both contact layers should be relatively thin to minimize waveguide loss. Because an etch-stop layer can be used for processing both surface plasmon and metal-metal waveguides from the same sample, a sample that has an optimal lower plasma layer thickness for a surface plasmon

waveguide will not be optimal for a metal-metal waveguide. As an example, the threshold gain was computed for a metal-metal waveguide with a top contact layer 60 nm thick doped at $5 \times 10^{18} \text{ cm}^{-3}$, and for lower plasma thicknesses of $t_{\text{plasma}} = 150$ and 500 nm doped at $3 \times 10^{18} \text{ cm}^{-3}$ (and found to change very little for guide widths from 100 to 200 μm). The threshold gain was calculated to be only 8.5 cm^{-1} for $t_{\text{plasma}} = 150 \text{ nm}$ and increased to 18.2 cm^{-1} for $t_{\text{plasma}} = 500 \text{ nm}$ (both with a resonator length of 1 mm). The thinner plasma layer thickness of 150 nm can be seen to result in an improvement for the metal-metal waveguide. Although the threshold gain is higher for a surface plasmon waveguide, the output coupling factor $\alpha_m/(\alpha_m + \alpha_w)$ can be smaller for some surface plasmon waveguides which is better for high power applications, i.e., since the output power $= \frac{1}{2} \eta_i \alpha_m / (\alpha_m + \alpha_w) N \hbar \omega / |e| (I - I_{th})$ from a single facet of an uncoated device.

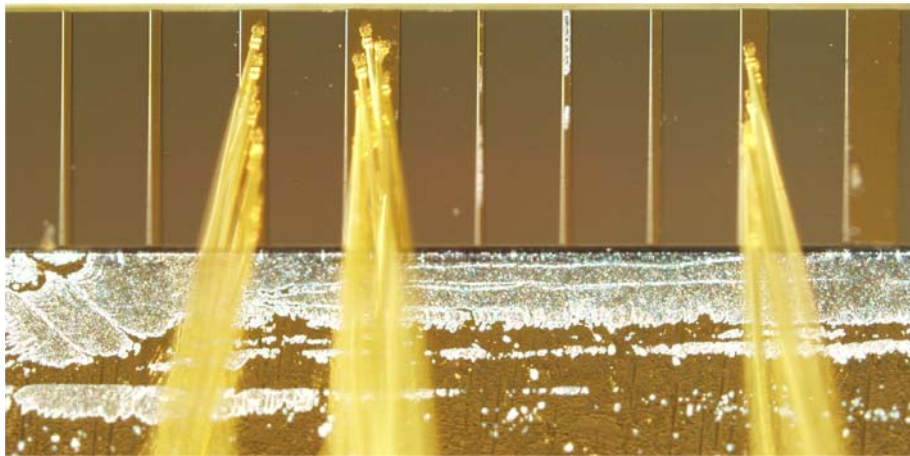


Figure VI.A.9. 200 μm ridge, 10 μm thick metal-metal waveguide, cross-section 2D mode intensity.

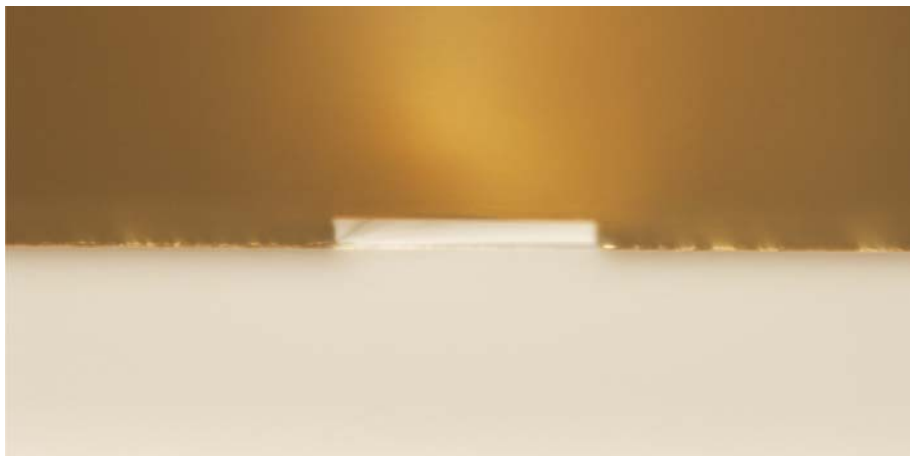
a. MBE Growth and Fabrication

The sample was grown by MBE using IQE foundry service, with $N = 185$ sections, where the top and lower contact plasma layers were 60 nm thick (10 and 50 nm layers doped at 5×10^{19} and $5 \times 10^{18} \text{ cm}^{-3}$, with the to be lower contact also having a 3.5 nm LTG GaAs layer). The sample was processed by the National Research Council (NRC) (Canada) into metal-metal waveguides of 100 and 200 μm wide, and 1 mm resonator lengths, with both facets uncoated (Figure VI.A.10). The fabricated devices showed an unusually high impedance ($> 1 \text{ k}\Omega$) at room temperature, compared to typical QCLs of about 10Ω . This likely indicates that there was either a growth problem, such as a high p-type background concentration during MBE growth (which depleted the electron concentration in the active region), or non-ohmic contacts generated during the processing. Initial electroluminescence measurements were made at $T = 10 \text{ K}$ (using a CTI Cryogenics Model 22 closed cycle He cryostat and a Nexus 870 FT-IR ESP Nicolet

spectrometer), and no light out was detected. Measurements on the sample showed little current through the device near the injector anticrossing (at ~ 10.6 V, ~ 300 mA, which corresponds to 150 A/cm²), as illustrated in Figure VI.A.11 for a 200 μm wide device. The I-V characteristics were measured on both the 100 and 200 μm wide samples out to about ~ 5 A, without the device going into NDR. Because the contact resistance was so high and no light was detected, there was either a growth or contact processing error with this sample.



(a)



(b)

Figure VI.A.10. Sample D619F10D. (a) Top view of the metal-metal waveguides, showing bond wires to the 100 and 200 μm wide by 1 mm long waveguides. (b) Cross-section of one of the 100 μm wide waveguides.

We are currently investigating the cause of the high impedance to determine the origin which will help us refine the growth and fabrication processes. Tests are being performed, using secondary ion mass spectrometry (SIMS) at NRC, to determine if correct doping concentrations were maintained in the sample growth. No conclusion on the feasibility of this device can be drawn from these measurements, as clearly there was a fabrication problem.

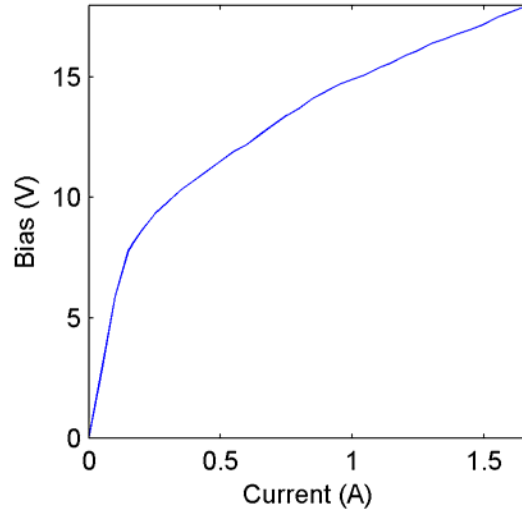


Figure VI.A.11. The measured I-V curve of sample D619F10D, for a 200 μm wide by 1 mm long metal-metal waveguide device.

b. Monte Carlo Simulation

A Monte Carlo simulation of QC structure D619F10D was performed, to model the electron ensemble. As previously discussed, the scattering between more than one section is taken into account because of the nature of the step well QC structure (which potentially can further lead to an overestimation of the scattering between weakly coupled states). The scattering mechanisms that were included are LO-phonon, electron-electron, impurity, and interface roughness scattering. The scattering rates were calculated via Fermi's golden rule. All rates from these simulations are net rates and include backscattering. State blocking and screening are also included in the simulations. The Monte Carlo simulations of the step well QC structure were performed with $T_{\text{lattice}} = 25$ K. Shown in Figure VI.A.12 is the calculated current density and gain (assuming a 4.1

meV *FWHM*) over the high gain bias region. The calculated gain is higher over much of this region than the threshold gains computed earlier for the waveguide resonator configurations analyzed. However, just beyond 50 mV/section a dip in the gain curve is observed. It was felt that a more uniform gain could be realized, by modifying the structure slightly to improve the injection efficiency.

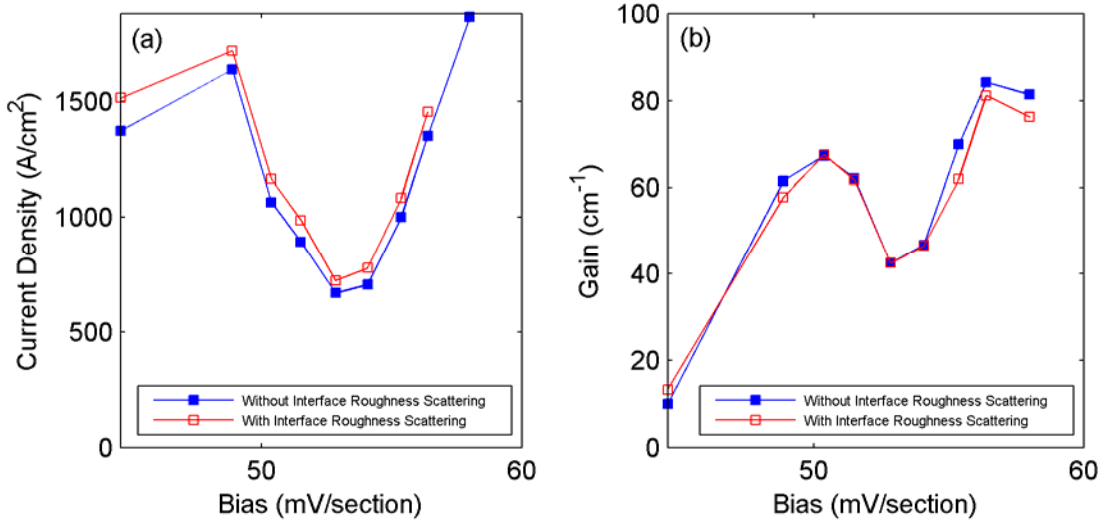


Figure VI.A.12. Results of the Monte Carlo simulation of structure D619F10D, with and without including interface roughness scattering. (a) Current density as a function of applied electric field bias. (b) Gain as a function of bias.

2. Structure D619F10E

The dip in the gain curve seen from the Monte Carlo simulation of QC structure D619F10D, was likely a result of inefficient scattering into the upper state at those biases. In order to correct for this, a second structure was designed and analyzed, structure D619F10E where the injector well was thinned slightly and the collector well thickness increased slightly. With these changes, it was anticipated a more uniform gain over these biases could be achieved. The conduction band profile for the step well QC structure is shown in Figure VI.A.13.¹¹³ Electrons are injected into the upper state 3 and the radiative transition occurs between state 3 and middle state 2, where $E_{32} = 15.2$ meV (~ 3.7 THz or $\lambda \sim 82 \mu\text{m}$). The LO-phonon assisted transition takes place from the middle state 2 to the lower doublet states (1, 0), since $E_{21} = 37.9$ meV which is near $\hbar\omega_{LO}$ (~ 36 meV in

GaAs). This ensures fast depopulation of state 2 via LO-phonon scattering, with a scattering rate lifetime $\tau_{2 \rightarrow (1,0)} \sim 0.5$ psec (band edge) for this structure. Again, the anticrossing between states 2 and 5' is relatively small (less than ~ 0.5 meV) due to the thick collector and injector barriers, and therefore should not be a primary path of scattering out of state 2. Though any electrons that transition from state 2 to 5' would serve to help the population inversion, and state 5' is near the resonant LO-phonon energy spacing to upper state 3'. Injection from the lower doublet states (1, 0) is to take place into the next adjacent sections upper state 3', and the injector anticrossing has been slightly increased to $E_{03'} \sim 1.2$ meV. The step well has been arranged so that state 3 is above the step and the state 2 below the highest point so as to provide spatial separation at the injector barrier for improved injection.

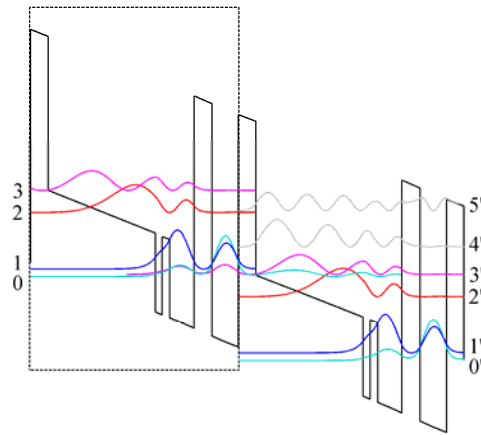


Figure VI.A.13. Conduction band profile of structure D619F10E found using a self consistent solution to Schrödinger's and Poisson's equations, shown at an applied electric field of 10.4 kV/cm (56.3 mV/section). The step well and resonant tunneling well of one section are outlined. Beginning with the left injector, the $\text{Al}_x\text{Ga}_{1-x}\text{As}$ layers compositions are 0.16/0.05/0/0.05/0.16/0 and thicknesses in nm are 4.6/27.9/1.8/2/6.3/4.7/6.8, with $E_{32} = 15.2$ meV (~ 3.7 THz) and $E_{21} = 37.9$ meV. The center 2 nm of the 6.8 nm well is doped to a sheet density of $3.4 \times 10^{10} \text{ cm}^{-2}$.

Since the transitions are intrawell in nature, the LO-phonon scattering is relatively fast. The radiative transition is also intrawell, and the overlap of the wavefunctions is reasonably good, giving an oscillator strength of ~ 0.94 at 9.9 kV/cm (53.6 mV/section).

The Monte Carlo method was used to model the electron ensemble of QC structure D619F10E, in the same manner as for the previous structure analyzed.¹¹³ The

Monte Carlo simulations of the step well QC structure in Figure VI.A.13 were performed with $T_{lattice} = 25$ K. Table VI.A.I lists the subband populations and electron temperatures found at an applied electric field of 53.6 mV/section.

n	n_{2D} ($\times 10^9$ cm $^{-2}$)	$T_{electron}$ (K)
0	16.1	131
1	10.1	132
2	1.53	155
3	6.22	127

Table VI.A.I. Populations of the subbands (E_n) and electron temperatures found from the Monte Carlo simulation of structure D619F10E, at an applied electric field of 53.6 mV/section, with $T_{lattice} = 25$ K.

The current density, gain, and population densities and the electron temperatures for the upper (E_3) and middle (E_2) states are shown in Figure VI.A.14 over a range of applied electric field biases. The results are shown with and without including interface roughness scattering. Others have shown reasonable agreement with experimental findings by not including interface roughness scattering in their simulations,¹¹⁴ and that agrees with our simulations of other square well structures. In these simulations interface roughness scattering was found to increase somewhat the current density and electron temperatures, and also slightly decreases the medium gain. The current density as a function of applied bias follows about what is expected, with the exception of the points between ~ 45 to 50 mV/section. This is where some scattering to parasitic current channels takes place. These high values are likely due to an overestimation of the scattering to the weakly coupled states. A small bump in the curve at ~ 38.4 mV/section is observed, where this is near the anticrossing between states 0 and 2'. The step serves to also minimize scattering between states 0 and 2' at this intermediate bias.

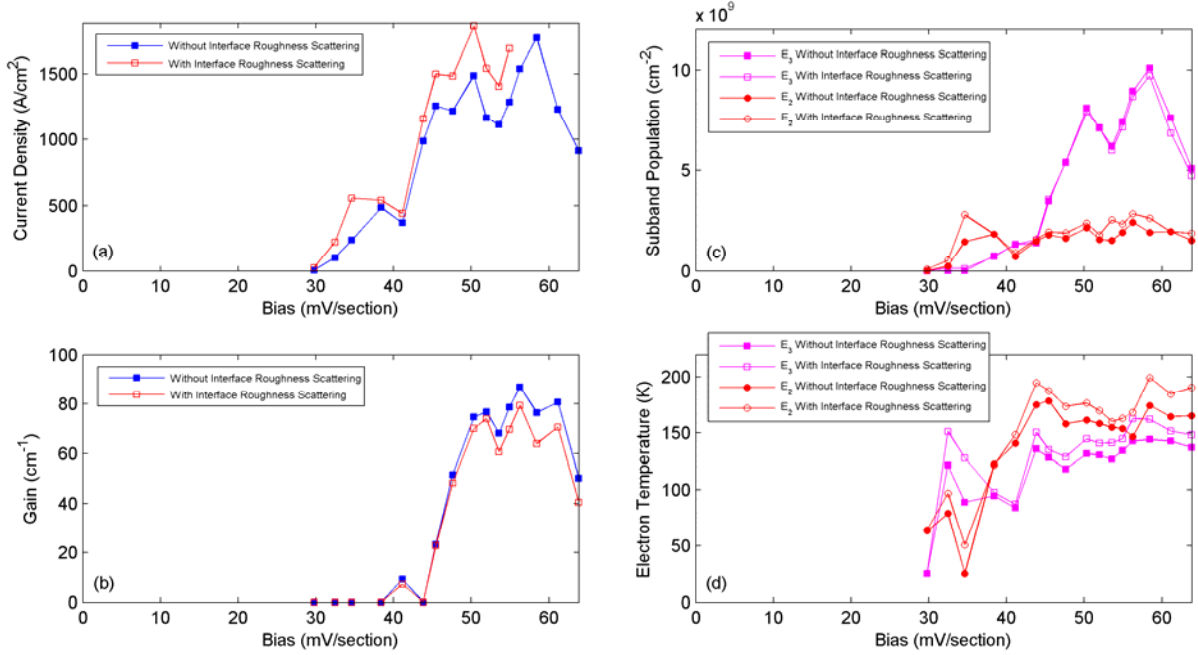


Figure VI.A.14. Results of the Monte Carlo simulation of structure D619F10E, with and without including interface roughness scattering. (a) Current density as a function of applied electric field bias. (b) Gain as a function of bias. (c) The population densities and (d) electron temperatures for the upper (E_3) and middle (E_2) subbands as a function of bias.

A peak gain of 86.9 cm^{-1} is found (assuming a $FWHM = 4.1 \text{ meV}$) and the gain is $\sim 70 \text{ cm}^{-1}$ or higher across much of the high gain bias region. This is due to the vertical transitions of the optical and LO-phonon transitions, as well as the high injection efficiency from the step. The vertical optical transition allows for a relatively high oscillator strength and fast LO-phonon scattering helps keep the middle state 2 depleted. Due to the step, injection loss to the middle state 2' is relatively small. The injection efficiency is found to be $\sim 89\%$, defined here to be from the lower doublet states (0, 1) to the upper state 3'. The lifetime of the middle state due to LO-phonon scattering is found to be $\tau_{2 \rightarrow (1,0)} = 0.88 \text{ psec}$, with the ratio of $\tau_{3 \rightarrow (1,0)}/\tau_{2 \rightarrow (1,0)}$ from LO-phonon scattering varying from about 2.1 to greater than 3 across biases in the high gain region. The calculated gain is seen to be higher than the calculated threshold gains for both the surface plasmon and metal-metal waveguides analyzed earlier.

B. SQUARE WELL LO-PHONON QC STRUCTURE

As previously discussed, only square quantum well structures have been used in QCL designs. The highest power QCL, reported in the given reference,¹⁰ utilized a four square well LO-phonon structure and operated at ~ 4.4 THz. This device represents a relatively optimized design in terms of the structure, wavelength of operation, and waveguide, to achieve a peak power of ~ 250 mW in a ~ 200 μm wide by ~ 1.2 mm long surface plasmon waveguide configuration. There were $N = 183$ sections grown, and the lower plasma layer was 400 nm doped at $3 \times 10^{18} \text{cm}^{-3}$. As with all conventional square well LO-phonon designs, it contained the usual first three square wells, and a fourth injector well similar to the first LO-phonon THz QCL. The third well is used to resonantly tunnel the lower lasing state and also arrange for a lower ground state. Because of this, as with other LO-phonon square well designs, there is a doublet of states at the lower lasing state. This structure will next be described in detail, and we will model it using our Monte Carlo code to compare the simulation results to the experimentally measured results.

1. 4.4 THz Structure

The conduction band profile for the 4.4 THz QC structure is shown in Figure VI.B.1. Electrons are injected into the upper state 4 and the radiative transition occurs between state 4 and state 3. The design was intended to emit near 4.7 THz, but was experimentally found closer to ~ 4.4 THz ($\lambda \sim 68$ μm). The LO-phonon assisted transition primarily takes place from state 2 (as well as from state 3) to the lower doublet states (1, 0), since E_{21} is near $\hbar\omega_{LO}$ (~ 36 meV in GaAs). States 3 and 2 are intended to be coupled for fast scattering between those states. This ensures fast depopulation of the lower lasing state via LO-phonon scattering. Injection from the lower doublet states (1, 0) is to take place into the next adjacent sections upper state 4'. This shorter wavelength of operation and hence larger radiative energy separation of the upper and lower lasing states, along with good coupling at the injector, aids in improved injection.

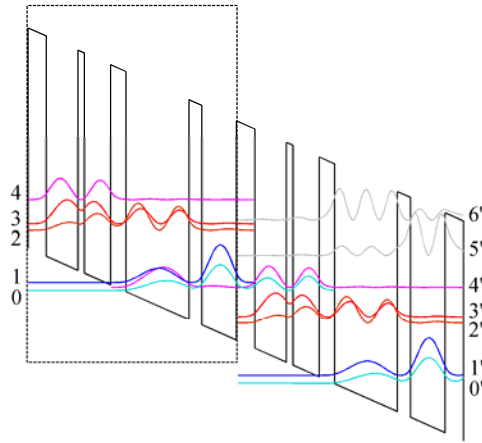


Figure VI.B.1. Conduction band profile of the 4.4 THz structure, shown at an applied electric field of 11.5 kV/cm (62.4 mV/section), with one section outlined. Beginning with the left injector, the $\text{Al}_x\text{Ga}_{1-x}\text{As}$ layers compositions are 0.15/0/0.15/0/0.15/0/0.15/0 and thicknesses in nm are 4.8/8.2/1.7/6.8/4.0/16.4/3.4/9.0. The 16.4 nm well is doped to a sheet density of $3.1 \times 10^{10} \text{ cm}^{-2}$.

The Monte Carlo simulations of the 4.4 THz QC structure were performed with $T_{\text{lattice}} = 25 \text{ K}$. The current density and gain are shown in Figure VI.B.2 over the high gain bias region of the device. The results are shown with and without including interface roughness scattering, for roughness of $a/2$ (same as previously used for the step well structures analysis) and $a/4$. In these simulations, reasonable agreement is shown with the interpolated measured values¹⁰ for the current density at most biases, with the largest difference being an overestimation occurring $\sim 68 \text{ mV/section}$ which is just beyond the injector anticrossing and near the $E_{26'}$ anticrossing. This overestimation is likely due to not including coherent effects of dephasing. As with the previous step well structure analyzed, the effects of interface roughness scattering were found to increase somewhat the current density, and also slightly decrease the medium gain. It is seen that assuming a roughness of $a/2$ overestimates the current density, and that using a roughness of $a/4$ is almost negligible compared to simulations without including interface roughness scattering. Although one monolayer (ML) is sometimes listed as $a/2$, this really depends on how it is defined. A GaAs unit cell consists of two Ga layers and two Al layers. During growth, it is possible to monitor the Ga and As layers separately. If each of these

layers is defined as one monolayer, then there are four monolayers and $1 \text{ ML} = a/4$ by definition. On the other hand, if one defines one Ga layer plus one As layer as one monolayer, then there are two monolayers and $1 \text{ ML} = a/2$ by definition. The gain is also calculated, and the device yields high gain.

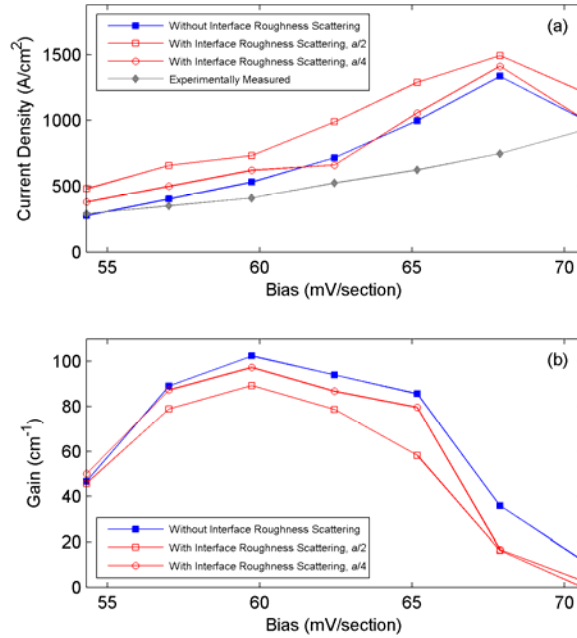


Figure VI.B.2. Results of the Monte Carlo simulation of the 4.4 THz structure, with and without including interface roughness scattering. (a) Current density as a function of applied electric field bias. (b) Gain as a function of bias.

This analysis indicates that interface roughness scattering effects are only appreciable for roughness greater than $\sim 1 \text{ ML}$, and that overestimation in the current density may occur assuming a roughness of $a/2$. The results presented earlier for the step well structure, which included interface roughness scattering assuming a roughness of $a/2$, are likely to be overestimating the current density of the structure. While interface roughness can vary from sample to sample, this analysis shows the importance of maintaining correct tolerances during growth. Because our analysis shows reasonable agreement with the experimentally measured current densities, it indicates that our Monte Carlo analysis of the step well structures should have similar accuracy.

THIS PAGE INTENTIONALLY LEFT BLANK

VII. CONCLUSIONS AND DISCUSSION

This research focused on modeling electron transport properties of THz LO-phonon QC structures, including the design and analysis of new step well QC structures. From the Monte Carlo simulations, it was found that step well structures are capable of high gains and oscillator strengths, high injection efficiencies, with comparable characteristics to other square well designs, but do have increased scattering from the upper state to the lower states. The peak gain of $\sim 87 \text{ cm}^{-1}$ found in these simulations of a step well QC structure, is higher than the peak gain of $\sim 73 \text{ cm}^{-1}$ reported for a simulated LO-phonon square well design, which also showed similar overestimation of the current density from their Monte Carlo simulations.¹¹⁴ The current density near the injector anticrossing was higher in these step well QC structure results and some of the electron temperatures were slightly higher as well. This overestimation of the current density was likely due to not taking into account coherence effects.

Perhaps one of the most important results from these simulations on the step well QC structures, showed high injection efficiencies are possible using a step well injector. Though the injection efficiency was much higher than typical for square well LO-phonon designs with similar oscillator strengths (~ 1.6 times higher), the current density was still high due to scattering from the upper to lower states. It may be possible to utilize a step well injector to improve injection efficiency, even if the step is not used to arrange all three energy states within the same well. Utilizing a step well injector with resonant tunneling, could yield the benefits of both good injection efficiency and improved upper to lower state lifetime. Our analysis is the first to suggest using more than one potential height, using two or more Al compositions, in a QCL active region structure.

The step well structure that was grown and processed, failed experimentally. Because of the large contact resistance and the low current through the device at the injector anticrossing, it was determined this was due to a growth or contact fabrication problem. Therefore, it was not possible to conclude the practical feasibility of such structures. Testing is being conducted to determine the source of the fabrication problem. The step well design remains a promising approach that differs from the two successful

approaches that have previously been used (miniband and square well LO-phonon). Because the middle state (upper phonon or lower lasing state) is a single energy state, contrasting to previous LO-phonon based QCL designs that have doublet states, for long wavelength lasers this could be important because it eliminates the possibility for unwanted THz absorption that could otherwise occur between those doublet states.

The Monte Carlo simulations performed on a high power conventional square well LO-phonon design, showed reasonable agreement with experimentally measured results. This indicated that our simulations of the step well structures, was likely of similar accuracy. It was also found that interface roughness scattering becomes significant for roughness greater than approximately one monolayer, and including interface roughness scattering in simulations can lead to an overestimation of the current density in the device, depending on the roughness height chosen. This illustrates the importance of maintaining tight growth tolerances for QC structures.

Although a high oscillator strength can lead to high gain, provided the upper state lifetime can be maintained, optimum temperature devices may be realized using lower oscillator strength structures. It should be pointed out that the best temperature performing devices are due to their higher frequency of operation, and none across the THz frequency range perform much better than $T \sim E_{radiative}/k_B = \hbar\omega/k_B$.^{12,13} A longer wavelength device might operate at a lower temperature, but with respect to $E_{radiative}/k_B$ be the same or better than a shorter wavelength device of higher operating temperature. Even in step well structures, it is possible to make the radiative transition more diagonal by utilizing an additional well prior to the step, and also by not arranging all three energy levels within the same well.

The overestimation between weakly coupled states that occurs in the Monte Carlo simulations, can be dealt with either by including dephasing in a density matrix Monte Carlo simulation or by using nonequilibrium Green's functions. The nonequilibrium Green's function technique is more intuitive from a quantum view point, and has several advantages. It can be used to include dephasing, many-body effects, and allow for spectral estimation.^{115,116} This technique is useful in many other areas of condensed matter physics as well. We are continuing to research these techniques and structures

discussed, and are also looking to include the effects of other parameters such as temperature in our analysis.

THIS PAGE INTENTIONALLY LEFT BLANK

LIST OF REFERENCES

1. R. Köhler, A. Tredicucci, F. Beltram, H. E. Beere, E. H. Linfield, A. G. Davies, D. A. Ritchie, R. C. Iotti, and F. Rossi, *Nature* **417**, 156 (2002).
2. J. Faist, F. Capasso, D. L. Sivco, C. Sirtori, A. L. Hutchinson, and A. Y. Cho. *Science* **264**, 553 (1994).
3. R. Colombelli et al., *Appl. Phys. Lett.* **78**, 2620 (2001).
4. J. S. Yu, A. Evans, S. Slivken, S. R. Darvish, and M. Razeghi, *Appl. Phys. Lett.* **88**, 251118 (2006).
5. D. G. Revin, J. W. Cockburn, M. J. Steer, R. J. Airey, M. Hopkinson, A. B. Krysa, L. R. Wilson, and S. Menzel, *Appl. Phys. Lett.* **90**, 021108 (2007).
6. M. P. Semtsiv, M. Wienold, S. Dressler, and W. T. Masselink, *Appl. Phys. Lett.* **90**, 051111 (2007).
7. S. Slivken, A. Evans, W. Zhang, and M. Razeghi, *Appl. Phys. Lett.* **90**, 151115 (2007).
8. G. Scalari, C. Walther, J. Faist, H. Beere, and D. Ritchie, *Appl. Phys. Lett.* **88**, 141102 (2006).
9. A. W. M. Lee et al., *Appl. Phys. Lett.* **89**, 141125 (2006).
10. B. S. Williams, S. Kumar, Q. Hu, and J. L. Reno, *Electron. Lett.* **42**, 89 (2006).
11. J. Faist, G. Scalari, C. Walther, and M. Fischer, *Materials Research Society (MRS) CC7.2* (2007).
12. S. Kumar, Q. Hu, and J. L. Reno, *Appl. Phys. Lett.* **94**, 131105 (2009).
13. B. S. Williams, *Nature Photonics* **1**, 517 (2007).
14. M. Tacke, *Infrared Phys. Technol.* **36**, 447 (1195).
15. P. H. Siegel, *IEEE Trans. Microwave Theory Tech.* **50**, 910 (2002).
16. A. Maestrini et al., *IEEE Microwave Wireless Components Lett.* **14**, 253 (2004).
17. D. L. Woolard, E. R. Brown, M. Pepper, and M. Kemp. *Proc. IEEE* **93**, 1722 (2005).
18. I. Mehdi, G. Chattopadhyay, E. Schlecht, J. Ward, J. Gill, F. Maiwald, and A. Maestrini, *IEEE MTT-S International Microwave Symposium Digest*, 341 (2006).
19. T. G. Phillips and J. Keene, *Proc. IEEE* **80**, 1662 (1992).
20. B. B. Hu and M. C. Nuss, *Opt. Lett.* **20**, 1716 (1995).

21. D. M. Mittleman, M. Gupta, R. Neelamani, R. G. Baraniuk, J. V. Rudd, and M. Koch, *Appl. Phys. B* **68**, 1085 (1999).
22. P. Y. Han, G. C. Cho, and X.-C. Zhang, *Opt. Lett.* **25**, 242 (2000).
23. D. T. Leisawitz, W. C. Danchi, M. J. DiPirro, L. D. Feinberg, D. Y. Gezari, M. Hagopian, W. D. Langer, J. C. Mather, S. H. Moseley, M. Shao, R. F. Silverberg, J. G. Staguhn, M. R. Swain, H. W. Yorke, and X. Zhang, *Proc. SPIE* **4013**, 36 (2000).
24. H.-T. Chen, R. Kersting, and G. C. Cho, *Appl. Phys. Lett.* **83**, 3009 (2003).
25. K. J. Siebert, T. Löffler, H. Quast, M. Thomson, T. Bauer, R. Leonhardt, S. Czasch and H. G. Roskos, *Phys. Med. Biol.* **47**, 3743 (2002).
26. A. J. Fitzgerald, E. Berry, N. N. Zinovev, G. C. Walker, M. A. Smith and J. M. Chamberlain, *Phys. Med. Biol.* **47**, R67 (2002).
27. D. Zimdars and J. S. White, *Proc. SPIE* **5411**, 78 (2004).
28. K. Humphreys, J. P. Loughran, M. Gradziel, W. Lanigan, T. Ward, J. A. Murphy, C. O'Sullivan, *Proc. of the 26th Annu. Int. Conf. of the IEEE*, 1302 (2004).
29. J. E. Bjarnason, T. L. J. Chan, A. W. M. Lee, M. A. Celis, and E. R. Brown, *Appl. Phys. Lett.* **85**, 519 (2004).
30. P. H. Spiegel, *IEEE Trans. Microwave Theory Tech.* **52**, 2438 (2004).
31. J. F. Federici, D. Gary, R. Barat, and D. Zimdars, *Proc. SPIE* **5781**, 75 (2005).
32. M. Rochat, L. Ajili, H. Willenberg, J. Faist, H. Beere, G. Davies, E. Linfield, and D. Ritchie, *Appl. Phys. Lett.* **81**, 1381 (2002).
33. G. Scalari, L. Ajili, J. Faist, H. Beere, E. Linfield, D. Ritchie, and G. Davies, *Appl. Phys. Lett.* **82**, 3165 (2003).
34. R. Köhler, A. Tredicucci, C. Mauro, F. Beltram, H. E. Beere, E. H. Linfield, A. G. Davies, and D. A. Ritchie, *Appl. Phys. Lett.* **84**, 1266 (2004).
35. G. Scalari, N. Hoyler, M. Giovannini, and J. Faist, *Appl. Phys. Lett.* **86**, 181101 (2005).
36. C. Walter, G. Scalari, J. Faist, H. Beere, and D. Ritchie, *Appl. Phys. Lett.* **89**, 231121 (2006).
37. B. S. Williams, H. Callebaut, S. Kumar, Q. Hu, and J. L. Reno, *Appl. Phys. Lett.* **82**, 1015 (2003).
38. S. Kumar, B. S. Williams, and Q. Hu, *Appl. Phys. Lett.* **88**, 121123 (2006).
39. H. Luo, S. R. Laframboise, Z. R. Wasilewski, G. C. Aers, H. C. Liu, and J. C. Cao, *Appl. Phys. Lett.* **90**, 041112 (2007).
40. W. Freeman and G. Karunasiri, *Proc. Ninth Int. Conf. on Intersubband Transitions in Quantum Wells* (2007).
41. P. Harrison, R. W. Kelsall, *J. Appl. Phys.* **81**, 7135 (1997).

42. P. Kinsler, P. Harrison, and R. W. Kelsall, *Phys. Rev. B* **58**, 4771 (1998).
43. A. W. M. Lee and Q. Hu, *Opt. Lett.* **30**, 2563 (2005).
44. G. Karunasiri, Seventh Int. Symposium on Technol. and the Mine Problem (2006).
45. A. W. M. Lee, B. S. Williams, S. Kumar, Q. Hu, and J. L. Reno, *IEEE Photon. Tech. Lett.* **18**, 1415 (2006).
46. B. N. Behnken, M. Lowe, G. Karunasiri, D. R. Chamberlin, P. R. Robrish, and J. Faist, *Proc. SPIE* **6549**, 0C (2007).
47. B. N. Behnken, G. Karunasiri, D. R. Chamberlin, P. R. Robrish, and J. Faist, *Proc. Ninth Int. Conf. on Intersubband Transitions in Quantum Wells* (2007).
48. B. N. Behnken, G. Karunasiri, D. R. Chamberlin, P. R. Robrish, and J. Faist, *Proc. SPIE* **6893**, 22 (2008).
49. B. N. Behnken, G. Karunasiri, D. R. Chamberlin, P. R. Robrish, and J. Faist, *Opt. Lett.* **33**, 440 (2008).
50. B. N. Behnken, Dissertation, Naval Postgraduate School (2008).
51. D. C. Hutchings, *Appl. Phys. Lett.* **55**, 1082 (1989).
52. K. R. Lantz, Thesis, Naval Postgraduate School (2002).
53. P. Harrison, *Quantum Wells, Wires and Dots*, 2nd ed. (John Wiley & Sons Ltd, Chichester, 2006).
54. Communication with M. Troccoli.
55. H. C. Liu, M. Wächter, D. Ban, Z. R. Wasilewski, M. Buchanan, G. C. Aers, J. C. Cao, S. L. Feng, B. S. Williams, and Q. Hu, *Appl. Phys. Lett.* **87**, 141102 (2005).
56. A. Benz, G. Fasching, A. M. Andrews, M. Marti, K. Unterrainer, T. Roch, W. Schrenk, S. Golka, and G. Strasser, *Appl. Phys. Lett.* **90**, 101107 (2007).
57. B. Monemar, *Phys. Rev. B.* **8**, 5711 (1973).
58. D. Arnold, A. Ketterson, T. Henderson, J. Klem, and H. Morkoc, *Appl. Phys. Lett.* **45**, 1237 (1984).
59. B. El Jani, P. Gibart, J. C. Portal, and R. L. Aulombard, *J. Appl. Phys.* **58**, 3481 (1985).
60. M. Zachau, F. Koch, G. Weimann, and W. Schlapp, *Phys. Rev. B.* **33**, 8564 (1986).
61. J. Batey and S. L. Wright, *J. Appl. Phys.* **59**, 200 (1989).
62. L. Pavesi and M. Guzzi, *J. Appl. Phys.* **75**, 4779 (1994).
63. O. Madelung, *Data Science and Technology, Semiconductors: Group IV Elements and III-V Compounds* (Springer-Verlag, Berlin, 1991).

64. I. Vurgaftman, J. R. Meyer, and L. R. Ram-Mohan, *J. Appl. Phys.* **89**, 5815 (2001).
65. S. Adachi, *GaAs and Related Materials, Bulk Semiconducting and Superlattice Properties* (World Scientific, New Jersey, 1994).
66. E. Rosencher and B. Vinter, *Optoelectronics* (Cambridge University Press, Cambridge, 2002).
67. M. Brodsky and G. Lucovsky, *Phys. Rev. Lett.* **21**, 990 (1968).
68. S. Yamazaki, A. Ushirokawa, and T. Katoda, *J. Appl. Phys.* **51**, 3722 (1980).
69. K. Nash, M. Skolnick, and S. Bass, *Semicond. Sci. Technol.* **2**, 329 (1987).
70. H. Fröhlich, *Proc. Roy. Soc. A* **160**, 230 (1937).
71. Communication with B. Vinter.
72. R. P. Feynman, *Statistical Mechanics* (Westview Press, Boulder, 1998).
73. M. E. Peskin and D. V. Schroeder, *An Introduction to Quantum Field Theory* (Westview Press, Boulder, 1995).
74. D. D. Coon and R. P. G. Karunasiri, *Appl. Phys Lett.* **45**, 649 (1984).
75. J. P. Leburton. *J. Appl. Phys.* **56**, 2850 (1984).
76. S. Goodnick and P. Lugli, *Phys. Rev. B* **37**, 2578 (1988).
77. H. B. Teng, J. P. Sun, and G. I. Haddad, *J. Appl. Phys.* **84**, 2155 (1998).
78. J. J. Sakurai, *Modern Quantum Mechanics*, revised ed. (Addison Wesley Longman, Reading, 1994).
79. B. K. Ridley, *Quantum Processes in Semiconductors*, 4th ed. (Oxford University Press, New York, 1999).
80. M. R. Spiegel, *Shaum's Mathematical Handbook of Formulas and Tables*, 2nd ed. (McGraw-Hill, New York, 1998).
81. Communication with S. Feng.
82. J. D. Jackson, *Classical Electrodynamics*, 3rd ed. (John Wiley & Sons, Inc., New York, 1999).
83. M. Mösko, A. Mösková, and V. Cambel, *Phys. Rev. B* **51**, 16860 (1995).
84. A. Tomita, J. Shah, J. E. Cunningham, S. M. Goodnick, P. Lugli, and S. Chuang. Erratum: *Phys. Rev. B* **52**, 5445 (1995).
85. T. Ando, A. Fowler, and F. Stern, *Rev. Mod. Phys.* **54**, 437 (1982).
86. J. Smet, C. Fonstad, and Q. Hu, *J. Appl. Phys.* **79**, 9305 (1996).
87. P. Maldague, *Surf. Sci.* **73**, 296 (1978).
88. P. Kinsler, P. Harrison, and R. W. Kelsall, *Phys. Rev. B* **58**, 4771 (1998).

89. S. M. Goodnick, D. K. Ferry, C. W. Wilmen, Z. Liliental, D. Fathy, O. L. Krivanek, *Phys. Rev. B* **32**, 8171 (1985).
90. T. Unuma, M. Yoshita, T. Noda, H. Sakaki, and H. Akiyama, *J. Appl. Phys.* **93**, 1586 (2003).
91. B. K. Ridley, in *Theory of Transport Properties of Semiconductor Nanostructures*, edited by E. Scholl (Chapman & Hall, London, 1998).
92. D. K. Ferry and S. M. Goodnick, *Transport in Nanostructures*, (Cambridge University Press, Cambridge, 2008).
93. A. Yariv, *Optical Electronics in Modern Communications* (Oxford University Press, New York, 1997).
94. R. Köhler, A. Tredicucci, F. Beltram, H. E. Beere, E. H. Linfield, A. G. Davies, D. A. Ritchie, S. S. Dhillon, and C. Sirtori, *App. Phys. Lett.* **82**, 1581 (2003).
95. H. D. Rees, *Phys. Lett. A*, 416 (1968).
96. H. D. Rees, *J. Phys. Solids* **30**, 643 (1969).
97. C. Jacoboni and L. Reggiani, *Reviews of Modern Physics* **55**, 645 (1983).
98. C. Jacoboni and P. Lugli, *The Monte Carlo Method for Semiconductor Device Simulation*, (Springer-Verlag Wien, New York, 1989).
99. R. C. Iotti and F. Rossi, *Phys. Rev. Lett.* **87**, 146603 (2001).
100. Communication with H. Callebaut.
101. Communication with B. Sherfey.
102. J. Ulrich et al. *Physica B* **272**, 216 (1999).
103. Unterrainer, K. et al., *Appl. Phys. Lett.* **80**, 3060 (2002).
104. B. S. Williams, S. Kumar, H. Callebaut, Q. Hu, and J. L. Reno, *Appl. Phys. Lett.* **83**, 2124 (2003).
105. M. I. Amanti, M. Fischer, C. Walther, G. Scalari, and J. Faist. *Electron. Lett.* **43**, 573 (2007).
106. COMSOL Multiphysics, FEM solver.
107. Ansoft HFSS, FEM solver.
108. V. W. L. Chin, T. Osotchan, M. R. Vaughan, T. L. Tansley, G. J. Griffiths, and Z. Kachwala. *J. Elec. Mat.* **22**, 1317 (1993).
109. P. G. Huggard, J. A. Cluff, G. P. Moore, C. J. Shaw, S. R. Andrews, S. R. Keiding, E. H. Linfield, and D. A. Ritchie. *J. Appl. Phys.* **87**, 2382 (2000).
110. S. Kohen, B. S. Williams, and Q. Hu, *J. Appl. Phys.* **92**, 053106 (2005).
111. W. Freeman and G. Karunasiri, NAWCWD TM 8577 (2008).

112. W. Freeman and G. Karunasiri, U.S. Patent Application Filed, Patent Pending (2008).
113. W. Freeman and G. Karunasiri, Proc. SPIE **7311**, 73110V (2009).
114. H. Callebaut, S. Kumar, B. S. Williams, and Q. Hu, Appl. Phys. Lett. **84**, 645 (2004).
115. S.-C. Lee and A. Wacker, Phys. Rev. B **66**, 245314 (2002).
116. S.-C. Lee, F. Banit, M. Woerner, and A. Wacker, Phys. Rev. B **73**, 245320 (2006).

INITIAL DISTRIBUTION LIST

1. Defense Technical Information Center
Fort Belvoir, VA
2. Dudley Knox Library
Naval Postgraduate School
Monterey, CA